Communauté
UNIVERSITÉ Grenoble Alpes

THÈSE

Pour obtenir le grade de

DOCTEUR DE LA COMMUNAUTÉ UNIVERSITÉ GRENOBLE ALPES

Spécialité : **Physique**

Arrêté ministériel : 7 août 2006

Présentée par

Airidas KOROLKOVAS

Thèse dirigée par **Jean-Louis BARRAT** et
codirigée par **Philipp GUTFREUND**

préparée au sein de **l'Institut Laue-Langevin**
dans **l'École Doctorale de Physique**

Écoulement de polymères enchevêtrés aux interfaces

Thèse soutenue publiquement le **16 Décembre 2016**,
devant le jury composé de :

Prof. Jean-Louis Barrat
Université Grenoble Alpes (Directeur de thèse)
Dr. Philipp GUTFREUND
Institut Laue-Langevin (Co-encadrant de thèse)
Prof. Ralf EVERAERS
ENS Lyon (Rapporteur)
Dr. Fabrice COUSIN
CEA Saclay (Rapporteur)
Prof. Maximilian WOLFF
Uppsala University, Suède (Examinateur)
Prof. Giovanna FRAGNETO
Institut Laue-Langevin (Président du jury)

Acknowledgements

I express my sincere respect and gratitude to César Emmenegger-Rodriguez and Andres de los Santos who had faith in the project and have offered their chemistry expertise during our darkest hour when no part of the project seemed to work. A special thanks goes to Franz Adlmann and Anton Devishvili for their unwavering support and keeping my spirits high against adversity. I am also heavily indebted to my daily supervisor Philipp Gutfreund who guided me through the various facets of the PhD. I thank Elizabeth Charlaix for introducing me to this project and my thesis director Jean-Louis Barrat for his experienced advice and research freedom he trusted me with. The quality of this work was significantly improved thanks to the contributions of Maximilian Wolff, Alexis Chennevière, Frédéric Restagno, Andrew J.C. Dennison, and Liliane Léger.

This thesis was fully funded by the Institut Laue-Langevin, Grenoble, France. I also acknowledge the use of Partnership for Soft Condensed Matter (PSCM) laboratories, as well as travel funding from the European Soft Matter Infrastructure (ESMI) and Institut Henri Poincaré (IHP).

Grenoble, 11 January 2017 A. K.

Abstract

Shear responsive friction at solid-liquid interfaces could become an important component in various technologies such as microfluidics, lubrication and polymer processing. Our model system is a polymer brush grafted on a solid substrate, subject to shear flow by an entangled polymer solution. The structure of the brush was probed both experimentally by Rheo - Neutron Reflectometry, and by computer simulations based on soft blobs. In the simulations we demonstrate for the first time that it is possible to suppress polymer chain crossings and observe entanglement dynamics using only the soft blob repulsive potential. To confine the blobs between two hard plates we introduce a new boundary condition, mirror-and-shift, which enables a monotonic, rather than oscillatory, density profile climb at the interface. The simulation techniques are then combined and compared against experimental measurement of polymer brush thickness as a function of shear rate. A good quantitative agreement is obtained, concluding that the brush thickness collapses perpendicularly to the applied shear flow, and is thus a non-linear second order effect. We attribute this effect to the normal stress difference, commonly occurring in entangled polymer liquids in their shear thinning flow regime.

Key words: friction, entanglement, polymer brush, interface, computer simulation, rheology, neutron reflectometry

Résumé

La friction d'une surface en réaction au cisaillement pourrait devenir un élément important dans des diverses technologies telles que la microfluidique, la lubrification ou encore la production et le traitement des polymères. Notre système modèle est constitué d'une brosse polymère sous un écoulement d'une solution de polymère enchevêtrée. La structure de la brosse a été sondée expérimentalement par Rhéo - Réflectométrie Neutronique, ainsi que par la simulation numérique basée sur des globules très "mous" (*blobs* en anglais). Dans les simulations on montre pour la première fois qu'il est bien possible de supprimer le croisement de chaînes de polymères pour ensuite pouvoir observer la dynamique d'enchevêtrement grâce uniquement au potentiel répulsif des globules. Pour confiner ces globules entre deux plaques dures, on propose une nouvelle condition limite, appelée mirror-and-shift, qui produit un comportement de profil de densité monotone et non oscillatoire à l'interface. Ces innovations de simulation sont ensuite combinées et leur résultat est comparé avec nos mesures expérimentales de l'épaisseur de la brosse polymère, en fonction de taux de cisaillement. Un bon accord quantitatif est obtenu, dont la conclusion est que l'épaisseur de la brosse s'effondre perpendiculairement au cisaillement appliqué, ce qui est un effet non-linéaire de second ordre. On attribue cet effet à la différence des contraintes normales, qui se produit communèment dans des liquides de polymères enchevêtrés lorsqu'il sont poussés vers leur régime de rhéofluidification par un flot suffisant.

Mots clefs : friction, enchevêtrement, brosse polymère, interface, simulation numérique, rhéologie, réflectométrie neutronique

Contents

Acknowledgements **i**

Abstract (English/Français) **iii**

List of publications **ix**

List of abbreviations **xi**

Introduction **1**

1 From soft blobs to entangled polymers **7**
1.1 Basic polymer physics 7
1.2 Rouse dynamics 9
1.3 Entanglement dynamics 10
1.4 Simulation techniques 12
1.4.1 Molecular Dynamics 13
1.4.2 Dissipative Particle Dynamics 14
1.4.3 Brownian Dynamics 15
1.5 The key novelty: suppressing chain crossings using only soft blobs 16
1.6 Outlook 19

2 Soft blobs confined by hard walls **21**
2.1 The main innovation: mirror-and-shift boundary condition 21
2.2 Dry brushes 23

3 Polymer brushes under shear flow **27**
3.1 Polymer brush fabrication 28
3.2 Neutron reflectometry 29
3.3 Outlook 35

A Simulation of entangled polymer solutions **37**

B Simulating confined particles with a flat density profile **65**

C Polymer brush collapse under shear flow **77**

Bibliography **125**

Curriculum Vitae **127**

List of publications

This thesis is based on the following publications:

1. Simulation of entangled polymer solutions. Airidas Korolkovas, Philipp Gutfreund, and Jean-Louis Barrat. *The Journal of Chemical Physics* **145**, 124113 (2016)

2. Simulating confined particles with a flat density profile. Airidas Korolkovas. *Physical Review E* **94**, 021302(R) (2016)

3. Polymer brush collapse under shear flow. Airidas Korolkovas, César Rodriguez-Emmenegger, Andres de los Santos Pereira, Alexis Chennevière, Frédéric Restagno, Maximilian Wolff, Franz Adlmann, Andrew J.C. Dennison, and Philipp Gutfreund. Submitted to *Macromolecules* (November 2016)

List of abbreviations

BD	Brownian Dynamics
DEP	DiEthyl Phthalate
DFT	Density Functional Theory
DPD	Dissipative Particle Dynamics
dPS	deuterated PolyStyrene
FIGARO	Fluid Interfaces Grazing Angles ReflectOmeter
GPU	Graphics Processing Unit
hPS	hydrogenated PolyStyrene
ILL	Institut Laue-Langevin
LD	Langevin Dynamics
MD	Molecular Dynamics
NR	Neutron Reflectometry
PDMS	PolyDiMethylSiloxane
PS	PolyStyrene
SCFT	Self-Consistent Field Theory
SLD	Scattering Length Density
TOF	Time-of-flight
Wi	Weissenberg number

Introduction

Entangled polymer solutions show both liquid and solid behaviours [1, 2]. At low frequencies, the material flows just like a simple Newtonian liquid [3] such as glycerol. At higher frequencies, it stores the deformation energy and becomes a piece of an elastic rubber [4]. The cross-over between these two regimes is rather broad [5] and is centered around a characteristic relaxation time, required for one chain to diffuse a distance equal to its own size [6].

The bigger the molecule, the slower it moves due to overall friction, and moreover it has to travel further away to cover its own size, leading to (Rouse) relaxation time $\tau_R \propto M_w^2$, proportional to the square of the molecular weight [7]. However, very long chains become trapped in their own network and are unable to diffuse in a random direction. Instead, their motion is restricted to a one dimensional randomly curved tube, created by the topological constraints of other nearby chains. This entanglement effect slows down the relaxation to $\tau_d \propto M_w^3$ (disentanglement). Because of such a steep dependence, it is quite common to find polymer systems with a relaxation time of up to one second or more [8], while still being perfectly liquid. This time scale is very relevant for many practical, every day applications involving polymer flows: lubrication in mammalian joints [9], synthetic fibre production [10], or even advanced oil recovery from porous shale rock [11]. To understand these and many other phenomena, we will have to deal with the following conditions: i) polymer liquids under shear flow, rather than at equilibrium; ii) behaviour at an interface, rather than bulk; and iii) preferably polymers in solution, rather than polymer melts.

In this thesis, one particular system has been chosen and studied in great depth: entangled polymer brushes under shear flow of a polymer solution, shown in Fig. 1. A polymer brush is made by chemically attaching one end of a polymer chain onto a substrate [12]. If the brush chains are very long, they can interpenetrate with the free chains (Fig. 1a), resulting in entangled dynamics. A second-order effect, called normal stress difference [13], kicks in under an applied shear flow (Fig. 1b), and pushes the brush to below its equilibrium height, acting perpendicular to the shear flow. Such a phenomenon could serve as a basis for the design of stress-responsive surfaces, enabling the engineering of dynamically controlled friction and adhesion properties.

The time scale of the phenomenon is governed by the reptation time of the free chains, $\tau_d \approx 1\,\mathrm{s}$ for a typical system. The applied shear rate $\dot{\gamma} = dv_x/dz$ is usually quoted in dimensionless

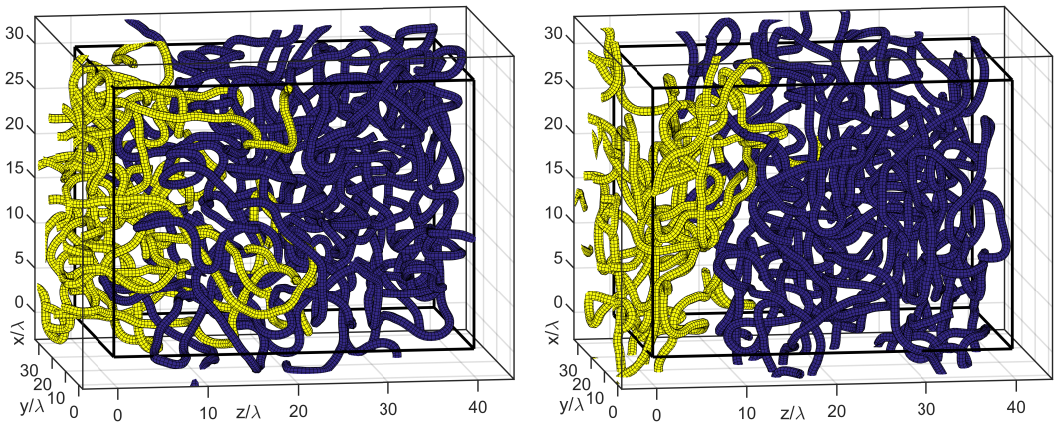

(a) Static

(b) Shear $\dot{\gamma} = dv_x/dz$

Figure 1 – An entangled polymer brush under shear flow. Yellow shows the grafted brush chains, dark blue shows the free bulk chains. As the shear rate exceeds $\mathrm{Wi} \gtrsim 1$, the brush shrinks and decouples from the bulk chains. Configuration snapshot from a Blob Dynamics simulation.

Weissenberg number $\mathrm{Wi} = \dot{\gamma}\tau_d$. The brush collapse is a non-linear phenomenon, meaning that its effect grows quadratically with the applied shear rate: $\Delta z \propto -\mathrm{Wi}^2$. Therefore, we have a rather sharp onset threshold: at small shear rates $\mathrm{Wi} < 1$ the effect is very weak, and at $\mathrm{Wi} > 1$ the brush starts shrinking much more rapidly, hence the term "brush collapse".

The entangled brush system was investigated experimentally via Neutron Reflectometry [14] as well as computationally via Blob Dynamics simulations [15]. This powerful combination is becoming increasingly demanded in the study of complex systems with lots of interacting parts. An experimental measurement typically provides information only on a few aspects of a much bigger issue. Computer simulations, on the other hand, can deliver much more data since all the modeled degrees of freedom are explicitly tracked. However, without backing from experiment, one cannot be sure if the calculated behaviour is realistic and actually occurs in nature. Therefore, joint experiment and simulation efforts are particularly welcome and their combined results are more trustworthy than the sum of each approach taken separately.

In the experiment, both the brush and the free chains in solution have to be chemically very similar if not identical, since for very large molecular weights, any disparity may cause an unwanted phase separation [16]. Therefore, the only viable method to clearly distinguish the brush from the free chains is isotopic labeling of their atomic nuclei, where hydrogen is replaced with deuterium, thus keeping identical chemistry but introducing a sharp contrast for neutron radiation [17]. The brush was grafted on a large $7 \times 7 \times 1$ cm silicon crystal, placed in contact with the polymer solution, and sheared [18] with a rotating titanium plate. Silicon is transparent for neutrons, and hence a neutron beam could shine through and reflect off the brush [19]. The reflection is stronger when the brush-bulk interface is sharper. We could

then effectively measure the brush roughness as a function of the applied shear rate, and have found that indeed the mean brush thickness collapses quadratically: $z/z_0 \approx 1 - \mathrm{Wi}^2$.

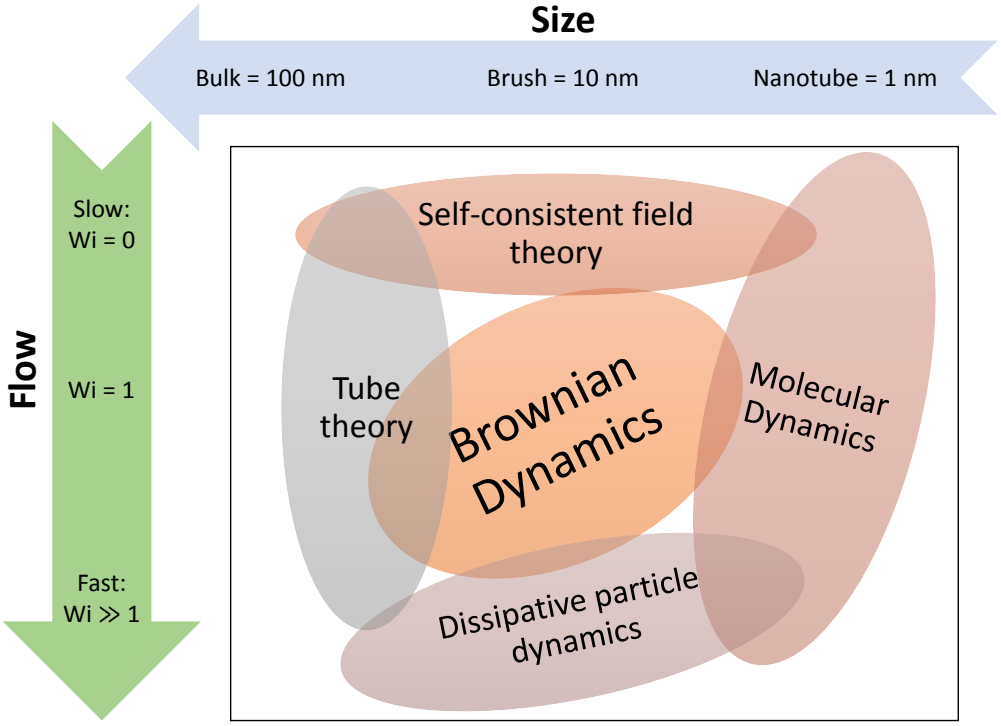

Figure 2 – Various computational techniques. The sketch (very roughly) shows the region of applicability, as a function of the system size and the applied shear rate.

On the theoretical and simulation side, there is a wide variety of approaches that have been used to study brushes. The more pertinent ones are summarized in Fig. 2. The main theoretical tool for brushes is the self-consistent field theory (SCFT) [20]. Here it usually takes the form of a one-dimensional differential equation, whose solution is the brush density profile which can be related directly to the experimentally measured neutron reflectivity spectrum. SCFT is rooted in the statistical mechanics and its basic idea is to find the shape of the brush which minimizes the total energy of the system [21]. However, under an applied shear flow the brush is far from equilibrium [22] and is constantly exchanging energy between the shearing apparatus and the heatbath, in which case the core SCFT assumptions are broken and do not seem to have easy fixes. Particularly problematic is the shear in the non-linear regime involving entanglement dynamics. Informally, we could say that under shear, the polymer chains try to be deformed as little as possible from their respective equilibrium shapes [23], but at present it is not clear how to translate this concept into an equation which could deliver the requisite monomer density profiles.

As far as entanglement is concerned [24], there is a very successful tube theory [25], which explains most of the known polymer dynamics, and only starts to break down at very large

shear rates Wi $\gg 1$ which are outside of our scope anyway. The main idea is to solve the equation of motion for just a single chain, subject to the mean field of topological constraints created by all the other chains. The mean field forces are then derived from the one chain dynamics itself, and this is repeated until a self-consistent result is reached. Unfortunately, the tube theory is strongly limited whenever its mean field assumption is violated, which happens at interfaces, narrow channels, and inhomogeneities such as brushes. It is not easy to extend the tube theory to heterogeneous settings, since the equation quickly gets very cumbersome, thus losing its appeal and compromising its predictive power relative to the amount of assumptions that must be build in.

We are currently not aware of any theories capable of reasonably calculating the entangled brush shape under shear. Our main tool is therefore a multi-chain simulation, where we solve the coupled equations of motion for about 100 interacting chains. The multi-chain model is representative of a tiny piece of the actual material, and could be mapped to about $(50\,\mathrm{nm})^3$ in our case. The main advantage of such simulations is that we do not need to make any high level assumptions about entanglement or other large scale features of the chain motion. Our main job is only to make sure that the chains are very long, immersed in a randomly fluctuating thermal bath, and are unable to cross each other. The entanglements and various non-linear shear effects such as the brush collapse emerge naturally by themselves and do not require any further models or assumptions.

Multi-chain simulations are considered to be brute force methods and require very efficient algorithms to produce useful results within an acceptable computational time. Therefore, many techniques have been developed [26], each pertaining to a specific length scale of interest. The most famous is the Molecular Dynamics (MD) [27] which runs on the scale of an atom. As indicated in Fig. 2, this technique is suitable for small molecules, and can be used under extremely strong shear flows. However, for the purposes of understanding entanglement, atomic resolution is not required, and therefore coarse-grained techniques are used much more often. Examples would be the Dissipative Particle Dynamics (DPD) [28] and its earlier version, the Langevin Dynamics (LD) [29]. These techniques are famously used to simulate entangled polymer melts, and due to their longer timescale, one can access more moderate shear rates. However, to simulate entangled polymer solutions, we will have to use an even coarser scale, called Brownian Dynamics (BD) [30]. The main advantage of this method is the possibility to reach quite low shear rates, which are directly relevant for our experimental situation and also many other practical applications.

In Chapter 1 we delve into the details of the BD technique but limit ourselves to only bulk entangled polymer solutions at equilibrium. The main novelty is that we are able to suppress chain crossings even at this very coarse scale. We clearly observe the emergence of entangled dynamics for the first time using only the soft blob repulsion.

Chapter 2 addresses a more technical issue on how to confine coarse, soft particles by a hard, sharp interface, such as a silicon crystal. This combination is necessary to properly model

our experimental system. We have therefore developed a new boundary condition, called mirror-and-shift. The idea is that the coarse particles confine themselves, creating an almost homogeneous system, but with walls. Our calculated density profiles at the interface agree well with experimental facts, which is something that is surprisingly difficult if not impossible to achieve with other existing confinement methods.

Lastly, in Chapter 3 we combine all our simulation techniques and present a model for an entangled polymer brush under shear flow. Simulation results are compared with our neutron reflectometry measurements of real polystyrene brushes, and a good agreement is found among the two approaches. The conclusion is that an entangled brush height shrinks quadratically with the applied shear rate, $\Delta z/z_0 \approx -\mathrm{Wi}^2$. The time scale is determined largely by the dynamics of the free chains in solution, and is not affected by the internal dynamics of the brush such as arm retraction. The brush returns to equilibrium when the shear is turned off. The effect can by cycled many times over. The brush collapse is expected to occur whenever there is a sufficiently deep interpenetration region between the brush and the free chains. The effect could not be observed for short chains (no entanglement), or very dense brushes (no interpenetration).

1 From soft blobs to entangled polymers

In this Chapter we describe a computer simulation of an entangled, semi-dilute polymer solution. For now, the discussion will be limited to a bulk system (using periodic boundary conditions), and at equilibrium. Care has been taken to setup the absolutely simplest possible model, adequate to describe real experiments at the appropriate scale. Our model barely requires any assumptions, which enables relatively straightforward extensions into more complicated settings, including confinement (Chapter 2), and an applied shear flow in contact with a brush (Chapter 3).

1.1 Basic polymer physics

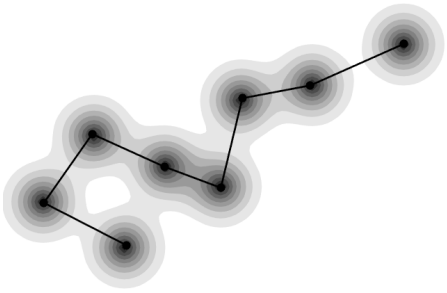

Figure 1.1 – The starting point: bead-and-spring model of a polymer chain. Our final, upgraded model is shown later in Table 1.1, third panel.

The most basic mechanical model of a polymer molecule is shown in Fig. 1.1. It is simply balls connected by springs. We will be primarily concerned with liquid polymers far above their glass transition temperature, and they can be either molten or dissolved in a good solvent. The main theme in polymer physics is that the chains try to maximize their entropy at all times, and hence they are constantly seeking to be as disordered and random as possible. If we neglect all interactions and just consider N balls located at $\mathbf{R}_n$, connected by springs of length λ, and immersed in a thermal bath, the chain will fluctuate and explore various possible shapes, or conformations, but in the long run its radius of gyration will remain fixed

to the average of

$$R_g = \sqrt{\langle (\mathbf{R}_n - \langle \mathbf{R}_n \rangle)^2 \rangle} = \sqrt{\frac{\lambda^2 N}{6}}, \tag{1.1}$$

which is precisely the result for a random walk of N steps and step length λ. There are two random walks involved here: each ball does a random walk of its own, and the conformation of the chain as a whole also develops the characteristics of a random walk. In a more realistic description we must take into account that each ball prefers to be surrounded by the solvent molecules, and stay way from other balls. This can be modeled mathematically by introducing a repulsive potential between each pair of balls a distance $\mathbf{r} = \mathbf{R}_n - \mathbf{R}_{n'}$ apart:

$$\Phi(\mathbf{r}) = k_B T \exp\left(-\frac{\mathbf{r}^2}{2\lambda^2}\right) \tag{1.2}$$

where $k_B T \approx 25\,\text{meV}$ is the thermal unit. The precise shape of the potential is not important when we have very long chains and are only interested in their large scale, or universal, properties. This interaction is commonly called the excluded volume force, where the "excluded volume" refers to $v \approx \lambda^3$ and is literally the volume of the ball. It can be shown [31] that with this repulsion, the radius of gyration swells to roughly

$$R_g \approx \lambda N^{0.6}. \tag{1.3}$$

However, our main system of interest is when a lot of such chains are packed close together,

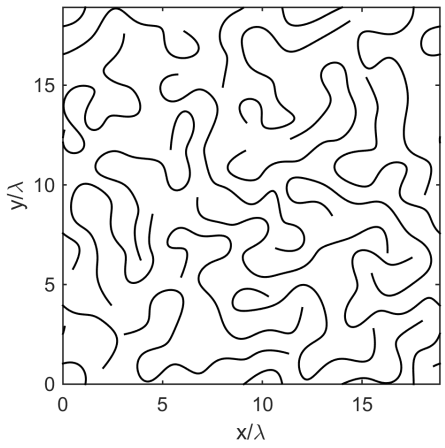

Figure 1.2 – Semi-dilute polymer solution in two dimensions. Chain length $N = 16$.

as illustrated in Fig. 1.2. In this case, the excluded volume interactions are screened and the radius of gyration once again scales as in Eq. (1.1): $R_g \approx \lambda\sqrt{N/6}$, but the pre-factor may be slightly different depending on the precise interaction parameters and pressure. The static, or thermodynamic, or $t \to \infty$, properties of polymers (such as the radius of gyration), have been extensively studied in the past and constitute a mature branch of science. A much more thorough introduction can be found in standard textbook presentations [32]. We will therefore

now switch to the less explored ground of polymer dynamics which are more difficult to tackle and where some open questions still remain for us to answer.

1.2 Rouse dynamics

If we turn off the excluded volume interaction, Eq. (1.2), and disregard hydrodynamic effects, the chains follow very simple equations of motion, first investigated in detail by Rouse [33]. Various dynamical properties of the Rouse model can be obtained analytically and are available in textbooks [7, 34]. Here we will mention just a few very basic and crude results. We will focus on the motion of the central $n = N/2$ monomer, because it is the furthest away from the chain ends and its motion shows the largest deviation from a simple random walk. The main quantity of interest is the mean squared displacement:

$$g_1(t) = \langle (\mathbf{R}_{N/2}(t) - \mathbf{R}_{N/2}(0))^2 \rangle . \tag{1.4}$$

At short time scales, the monomer does not realize that it is embedded in a much larger chain, and therefore its motion follows the random walk statistics:

$$g_1 \approx Dt, \quad t < \tau \tag{1.5}$$

Here

$$D = \frac{k_B T}{6\pi\eta_s \lambda} \tag{1.6}$$

is the diffusion coefficient for a particle of size λ inside a solvent of viscosity η_s, as derived from the fluctuation-dissipation theorem [35], while the equation itself is known by the name Einstein-Stokes [36]. The smallest relevant time unit is the time it takes the ball to diffuse a distance equal to its own size:

$$\tau \approx \frac{\lambda^2}{D} = \frac{6\pi\eta_s\lambda^3}{k_B T}. \tag{1.7}$$

At very long time scales, the central monomer must diffuse at the same rate as the entire molecule. It can be found by looking at the center of mass

$$\mathbf{R}_0 = \frac{\mathbf{R}_1 + \mathbf{R}_2 + \cdots + \mathbf{R}_N}{N} \tag{1.8}$$

If every ball is assumed to be an independent random walker, then their motion is uncorrelated $\langle \Delta\mathbf{R}_n \Delta\mathbf{R}_{n'} \rangle = 0$ and the mean square displacement of the center will be

$$\langle \Delta\mathbf{R}_0^2 \rangle = \frac{(\Delta\mathbf{R}_1 + \Delta\mathbf{R}_2 + \cdots + \Delta\mathbf{R}_N)^2}{N^2} \approx \frac{NDt}{N^2} \tag{1.9}$$

and therefore the diffusion is a factor N slower:

$$g_1 \approx \frac{Dt}{N}, \quad t \gg \tau_R \tag{1.10}$$

The Rouse relaxation time τ_R is the time it takes the chain to diffuse a distance equal to its own size:

$$\frac{D\tau_R}{N} \approx \lambda^2 N \quad \Rightarrow \quad \tau_R \approx \frac{\lambda^2 N^2}{D} = \tau N^2 \tag{1.11}$$

and is therefore proportional to the square of the chain length. One power comes from the fact that diffusion is slower, and the second power comes because the chain is bigger. At intermediate time scales, $\tau < t < \tau_R$, the central monomer should slow down to smoothly bridge the short and long time scales. If we assume a power-law behaviour, $g_1 = At^\alpha$, the unknowns A and α can be found by joining the two boundaries:

$$A\tau^\alpha = D\tau \tag{1.12}$$

$$A\tau_R^\alpha = \frac{D\tau_R}{N} \tag{1.13}$$

which can be solved to find $\alpha = 0.5$ and $A = D\tau^{0.5}$. The complete Rouse behaviour can be thus summarised:

$$g_1 = \begin{cases} Dt, & t < \tau \\ D\sqrt{t\tau}, & \tau < t < \tau N^2 \\ Dt/N, & t > \tau N^2 \end{cases} \tag{1.14}$$

The exact analytical solution [34] also confirms the power-law behaviour $g_1 \propto t^{0.5}$ at intermediate times. Our computer simulation is based on the Rouse model (random walkers connected by springs), plus an excluded volume repulsion between all chains. This repulsion, if suitably modeled, will suppress chain crossings, and that will give rise to entanglement dynamics, one aspect of which is a striking deviation from Eq. (1.14).

1.3 Entanglement dynamics

Entanglement dynamics [34] can be observed in both polymer melts and semi-dilute polymer solutions. Our simulation data showing the central monomer diffusion is plotted in Fig. 1.3. The mean squared displacement is normalized by $\sqrt{t}$, which is the Rouse prediction, Eq. (1.14). Quite clearly, the data deviates strongly from the Rouse model, and the mean squared displacement grows qualitatively slower than $t^{0.5}$, at the intermediate time scale. No combination of Rouse parameters could ever explain this data, and therefore a new theory must be introduced.

The earliest and simplest explanation of entangled polymer dynamics has been the tube

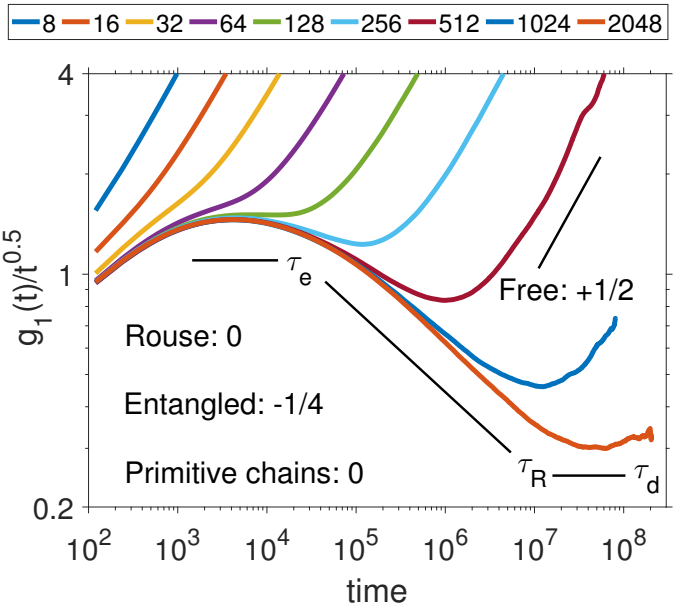

Figure 1.3 – Internal dynamics of an entangled polymer system. Plotted is the mean squared displacement of the central monomer, normalized by $\sqrt{t}$, which is the theoretical Rouse behaviour. Various chain lengths are shown from $N = 8$ to $N = 2048$. Data collected from a Blob Dynamics simulation.

theory. Here one says that the central monomer cannot diffuse in any random direction, but can only travel along the existing contour of its chain. Such an anisotropic diffusion is called "reptation". Any transverse motion would require a large deformation of the whole entangled network and is statistically unlikely. To quantify the tube idea, we can estimate that the square of the linear distance traveled by the central monomer during a time t is

$$L^2 \approx g_1^{(\text{Rouse})}(t) \approx D\sqrt{\tau t} \approx (\Delta n \lambda)^2, \tag{1.15}$$

where Δn is the number of monomers traversed in time t. Notice that this distance is rolled up inside a randomly curved tube, and therefore the actual mean squared displacement of the central monomer is merely

$$g_1^{(\text{reptation})} \approx \lambda^2 \Delta n \approx \left(D\lambda^2\sqrt{\tau t}\right)^{1/2} \propto t^{1/4} \tag{1.16}$$

The onset of this power law occurs at the entanglement time $\tau_e \approx \tau N_e^2$ when the monomer starts to realize that it is trapped in a tube. The N_e is called the entanglement length and is the minimum number of monomers required to see any deviation from the Rouse model, which in our case is about $N_e \approx 60$. The reptation picture is valid up to the Rouse time $\tau_R \approx \tau N^2$, when the chain fluctuations die out. After that, the chain still remains in its original tube up to the final disentanglement time $\tau_d \approx \tau N^3$, where the motion is again characterised by $g_1 \propto t^{0.5}$ behaviour, known as the primitive chain diffusion [37, 38]. The main point of the

simulation is to demonstrate the emergence of $g_1 \propto t^{0.25}$ diffusion behaviour at intermediate times, which is clearly slower than the Rouse model $g_1 \propto t^{0.5}$ predicts, and is hence a strong indicator that our chains are very long and unable to cross each other. Fig. 1.3 demonstrates how this very specific law emerges dynamically just by increasing the chain length, rather than being inserted statically through some additional forces.

The true entanglement is an emergent phenomenon of many long chains blocking each other's transverse motion. To model this mathematically, one must solve a system of non-linearly coupled, stochastic, differential equations with at least (50 chains) × (200 modes) = 10,000 degrees of freedom, which is the bare minimum required to see a significant and systematically growing deviation from the unentangled Rouse model. From a mechanical or rheological points of view, the entanglement transition is even broader and stronger, boosting the viscosity from $\eta \propto N$ in the Rouse regime, to over $\eta \propto N^3$ in the entangled regime. To fully observe it, one needs an additional factor of 10 more degrees of freedom, and hence a factor of $10^3 \times 10$ longer computing time.

Why do we need such intense computations? Well, one reason is that it takes about $N_e \approx 60$ random steps of two nearby chains, until they are sufficiently intertwined to form one entanglement. A random walk mostly just goes back and forth canceling itself, while its mean squared displacement is only

$$R_e = \sqrt{\frac{\lambda^2 N_e}{6}} \approx 3\lambda, \tag{1.17}$$

which seems like a reasonable distance for two chains of radius λ to be wound around each other. The second reason is that reptation is driven by pure entropy, rather than enthalpic forces, and therefore is vastly different from other large-scale molecular phenomena such as protein folding, binding, self-assembly, etc. There is no special "entanglement force" and no "entanglement energy" to speak of. Without any parameters, it is difficult to significantly alter or speed up the process. All we can do is let the segments fluctuate with their random walk while repelling each other, and wait patiently for 10^8 steps to finally see, in a statistical sense, what fascinating dynamical properties emerge from their very simple rules of interaction.

1.4 Simulation techniques

Historically, entanglement dynamics have been first demonstrated using bead-and-spring simulations [39], but are also possible with lattice-based models [40], and both are considered to be valid descriptions of polymer melts. Our main contribution is to also obtain such entanglement dynamics, but based on a simulation running on soft blobs, more suited for semi-dilute polymer solutions [41] rather than melts. In this section we briefly review the main simulation techniques, summarized in Table 1.1. We start from Molecular Dynamics, and end with Brownian Dynamics which was the starting point for building our own approach.

↑↑ Quantum Mechanics, Schrödinger equation ↑↑	
Molecular Dynamics Second order deterministic equation of motion Particle: atom Time unit: 10^{-13} s Length unit: 0.1 nm	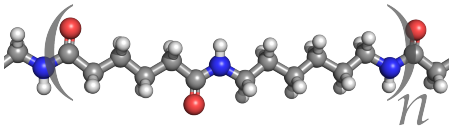
Dissipative Particle Dynamics Second order stochastic equation of motion Particle: bead Time unit: 10^{-11} s Length unit: 1 nm	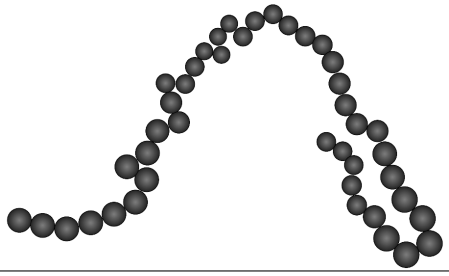
Brownian Dynamics First order stochastic equation of motion Particle: blob Time unit: 10^{-9} s Length unit: 10 nm	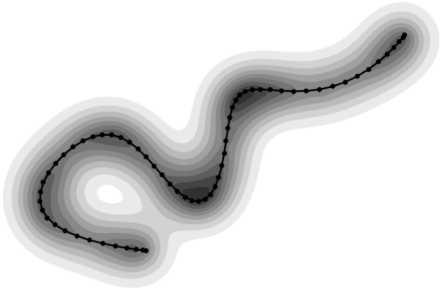
↓↓ Continuum Mechanics, Navier-Stokes equation ↓↓	

Table 1.1 – Main simulation techniques. Image sources: wikipedia.org, Ref. [42], and Ref. [15]

1.4.1 Molecular Dynamics

The earliest and most prolific computer simulation technique in material science is Molecular Dynamics (MD). In it, every atom is represented as a distinct particle, interacting with its neighbours via some model potential field such as Lennard-Jones. The model is typically justified on empirical and experimental grounds, and is often related or even derived from the underlying quantum mechanical structure of the electron cloud [43].

To discover how a model system behaves, one must solve the set of coupled Newton's equations

of motion, one for each atom, indexed n:

$$m_n \frac{d\mathbf{v}_n}{dt} = \sum_{n'=1}^{N} \mathbf{F}_{nn'}(t) \tag{1.18}$$

$$\frac{d\mathbf{r}_n}{dt} = \mathbf{v}_n(t) \tag{1.19}$$

usually supplemented with an explicit temperature constraint:

$$\sum_{n=1}^{N} \frac{m_n \mathbf{v}_n^2}{2} = \frac{3}{2} N k_B T \tag{1.20}$$

The equations are solved using small discrete time steps during which the interatomic force $\mathbf{F}_{nn'}$ changes only slightly and can be considered approximately constant. As a simple estimate, we require the distance traveled per step to be much smaller than the interatomic spacing. This reasoning leads to the time step

$$t_{\mathrm{MD}} = \left(\frac{\rho}{k_B T}\right)^{0.5} \lambda^{2.5} = 10^{-13}\,\mathrm{s} \tag{1.21}$$

where $\rho = 1\,\mathrm{g/cm^3}$ is the typical fluid density and $\lambda = 1\,\text{Å}$ is the typical atom size. The MD technique is widely used to study all kinds of materials at the atomic scale, including the conformation and ordering of macromolecules. Current computers [44] can typically perform 10^8 time steps within an acceptable waiting time which is usually a week, but some studies report counting times of up to one year.

1.4.2 Dissipative Particle Dynamics

There are many situations involving large macromolecules such as proteins and entangled polymers, which are simply out of each of MD's time scales. To help tackle some of these questions, widespread in biological and soft matter systems, various coarse-grained computer simulations have been developed. The idea is that sometimes we can afford to neglect certain atomic degrees of freedom. For instance, a polystyrene chain might be modeled as beads connected by springs, where each bead corresponds to one persistence length equal to a dozen of styrene monomers and totaling about a hundred of atoms. The lost degrees of freedom are taken back into account stochastically, by generating a randomly fluctuating force $\mathbf{W}(t)$, uncorrelated in time or space: $\langle W^\alpha(t) W^\beta(t')\rangle = \delta^{\alpha\beta}\delta(t-t')$. The state of the art equation of motion is called Dissipative Particle Dynamics (DPD) [45]:

$$m_n \frac{d\mathbf{v}_n}{dt} = \sum_{n'=1}^{N} \mathbf{F}_{nn'}(t) - \zeta\omega(r_{nn'})\,(\hat{\mathbf{r}}_{nn'} \cdot \mathbf{v}_{nn'})\,\hat{\mathbf{r}}_{nn'} + \sqrt{2\zeta k_B T \omega(r_{nn'})}\,\mathbf{W}_{nn'}(t) \tag{1.22}$$

Notice that a friction term must be included to maintain the temperature stable around a fixed level. One also has to introduce a friction coefficient $\zeta = 6\pi\eta_s\lambda$ which depends on the effective

medium viscosity $\eta_s \approx 5 \times 10^{-4}$ Pa s, in the case of toluene. To ensure the local conservation of momentum and the validity of Newton's third law, the random force does not come out of nowhere, but instead acts pairwise between neighbouring beads via some weight function $\omega(r) = e^{-r^2/\lambda^2}$, although its exact shape is not so important. Earlier studies, called Langevin Dynamics, did not use the pairwise random force generator, and momentum was indeed not conserved. More recent studies have shifted to DPD since it has a similar computational cost, but more accurate physics, especially the hydrodynamical properties. In either of those techniques, the time step is limited by the time it takes the momentum to decorrelate by a significant amount:

$$t_{\mathrm{DPD}} = \left(\frac{\rho}{\eta_s}\right)\lambda^2 = 10^{-11}\,\mathrm{s} \tag{1.23}$$

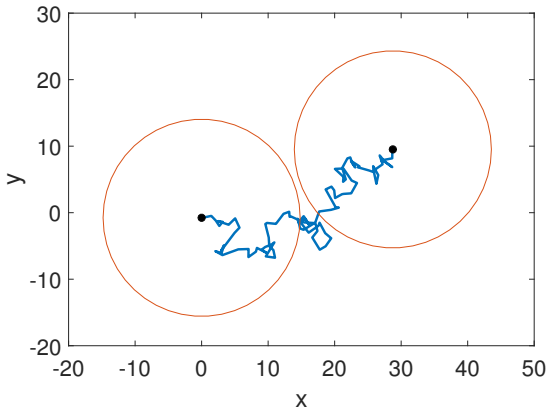

Figure 1.4 – Overdamped as opposed to ballistic motion. The blob's momentum relaxes hundreds of times before the displacement becomes comparable to the blob size itself. The blue line shows the fine-grain trajectory of the blob center of mass.

1.4.3 Brownian Dynamics

For the most massive macromolecules [46], even the DPD scheme cannot reach sufficiently long time scales. An example could be a polymer of very high molecular weight $M_w = 10^6\,\mathrm{g\,mol^{-1}}$ dissolved at a semi-dilute concentration $\phi = 30\%$, which means that there is still considerable chain interpenetration resulting in rich entanglement dynamics on the time scale of a second or more. In this case, the effective coarse particle is called a blob and it corresponds to the mesh size of the polymer network, which is the typical distance between two neighbouring chains. One blob can contain many thousands of atoms, and its effective potential field is smeared out resembling a Gaussian function, in contrast to the much steeper Lennard-Jones field used to model an atom in MD. However, to reap the full time-saving benefits, it is not enough to simply use a bigger particle. We must also understand that the blob's momentum relaxes hundreds or even thousands of times over, before it moves a distance equal to its own size, see Fig. 1.4. Therefore, it will be really beneficial to simply renounce

tracking the momentum altogether, and just be content with knowing the blob positions. Such an overdamped view is called Brownian Dynamics (BD), and is governed by a first order stochastic equation of motion:

$$\zeta \frac{d\mathbf{r}_n}{dt} = \sum_{n'=1}^{N} \mathbf{F}_{nn'}(t) + \sqrt{2\zeta k_B T}\mathbf{W}_n(t) \tag{1.24}$$

This equation runs on a time scale

$$t_{\mathrm{BD}} = \left(\frac{\eta_s}{k_B T}\right)\lambda^3 = 10^{-9}\,\mathrm{s} \tag{1.25}$$

or even less, depending on how big are the blobs. Despite its attractive long time scale, the BD technique has several other issues which have hampered its use in the simulation community. One of the harshest complaints is that the blobs are too soft and can easily overlap or even cross each other, which is unphysical and in the case of polymers prevents any entanglement dynamics from emerging [47].

1.5 The key novelty: suppressing chain crossings using only soft blobs

For our polymer problem, it can be shown [48] that the correct static properties will be obtained if the potential field of a blob is chosen to be about

$$\Phi(\mathbf{r}) = k_B T e^{-\mathbf{r}^2/2\lambda^2} \tag{1.26}$$

that is, one $k_B T$ high, and spread out in a smooth shape, resembling a Gaussian. During the time step t_{BD}, the blobs move by a small fraction of their own size and therefore the scheme is numerically stable. Meanwhile, the random force also shuffles the blobs around by roughly the same amount, but the excluded volume force is simply too weak to reliably counteract this, resulting in occasional blob crossings.

Our solution to this problem is to deliberately limit the time resolution as shown in Fig. 1.5. Simply put, a secondary, much larger time step is used to generate the requisite random force, whereas the original t_{BD} step is used to calculate the excluded volume force as usual. This scheme is still a valid discrete approximation to the original BD equation of motion, with the understanding that meaningful physical results are only accessible at the resolution of the largest time step.

The broader consequence is that the blobs can only be thought to exist at large time scales, exceeding substantially the t_{BD}. Basically, the concept of a blob only makes sense to an observer who blinks slowly. It is impossible to describe a system with soft blobs whilst also demanding a high time resolution: one must either renounce prying on the system too frequently, or suffer from the unphysical blob crossings.

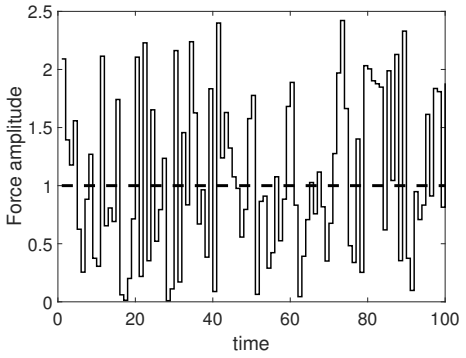

(a) Random force updated at every single time step

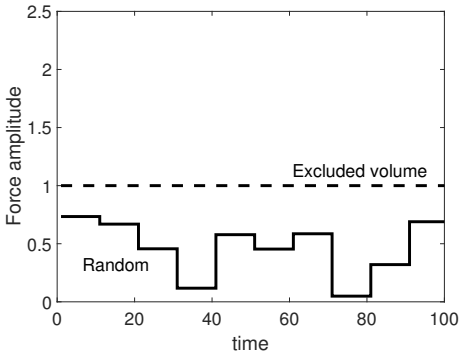

(b) Random force updated only once every 10 time steps

Figure 1.5 – Various discrete approximations of the continuous Wiener process $\langle W(t)W(t')\rangle = \delta(t-t')$

Another item that helps to reduce chain crossings is illustrated in Fig. 1.6. The random force vectors must be drawn from some random distribution. Usually, one employs the Gaussian distribution, Fig. 1.6a, because it is readily available in most programming environments, and it feels the "natural" choice, because of the central limit theorem which says that when a large number of independent random variables is added, the distribution tends to approach a Gaussian. However, the theoretical Gaussian function has an infinitely long tail, and this becomes a problem after (100 chains) × (1000 blobs) × (10^8 steps) = 10^{13} random vectors have been drawn. This number, ten trillion random numbers, is routinely reached in our present-day calculations, but it is actually quite modest and will only grow in the future. Unfortunately, it becomes a statistical certainty that one of those numbers, the biggest outlier, will have a value of about

$$\text{Gaussian}: \quad \texttt{max}(\text{random amplitude}) \approx \sqrt{2\log(\text{number of draws})} \approx 7.7 \tag{1.27}$$

It gets worse if we perform let's say 10 independent runs for better statistics, in which case the maximum outlier is expected at $\sqrt{2\log\left(10^{14}\right)} \approx 8.0$, and this estimate grows bigger for "unlucky" runs. This is bad news, since our claim of suppressing chain crossings is only as good as its weakest point, which is at that one blob out of 10^5, during that one step out of 10^8, when the biggest outlier is generated. The good news is that we are in fact by no means obliged to use the Gaussian shape. The only requirement is that the distribution is isotropic (equally likely in every direction), and that the mean square value of the random vector is fixed, which we have normalized to 2 for our two dimensional example. If these conditions are met, any reasonable distribution shape will result in the same static properties (radius of gyration, osmotic pressure, static structure factor, etc.). The dynamics, however, will be substantially improved if we choose a shape whose maximal outlier has the smallest possible value, while still maintaining a fixed mean square value for the entire distribution. A good

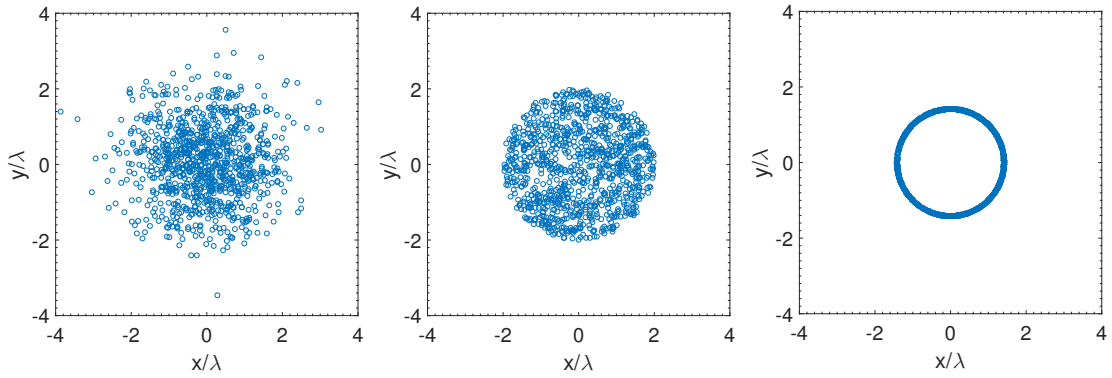

(a) Gaussian (b) Uniform (c) Shell or ring

Figure 1.6 – The random displacement vectors drawn from several isotropic distributions of different shapes, but all having the same mean square value. Each panel contains 1000 randomly generated points.

choice would be the uniform distribution (Fig. 1.6b) which has

$$\text{Uniform}: \quad \texttt{max}(\text{random amplitude}) = 2 \tag{1.28}$$

but the best of all is the shell (or ring, in two dimensions) shape:

$$\text{Shell}: \quad \texttt{max}(\text{random amplitude}) = \sqrt{2} \approx 1.4 \tag{1.29}$$

Clearly, the greatest outlier of the shell distribution is some $7.7/1.4 \approx 5.5$ times smaller than the corresponding outlier of the Gaussian, which translates into a hefty reduction of chain crossing likelihood.

These and some other useful ideas are described in much greater detail in the appended article A. There we show how to generalize the BD equation not just for individual blobs, but for very long polymer chains with the blob potential smeared continuously along the entire backbone.

A graphics processing unit (GPU) was used to simulate a system of 64 chains, with 1024 degrees of freedom each. Various dynamical properties were analyzed, which clearly demonstrate entanglement effects in agreement with earlier theories, experiments, and simulations. The main novelty is that the entangled system was simulated using soft Gaussian blobs connected by a linear spring interaction, which is the appropriate model in the semi-dilute state. No other interactions or constraints were required, which makes our model very well suited for future studies in more complicated settings, such as heterogeneous systems, confinement, and non-equilibrium situations.

1.6 Outlook

We must admit that there remain some unresolved drawbacks of the BD method. The most worrisome is that without information on particle momentum, it is unclear on how to locally obey the Newton's third law. Specifically, if we need to apply a shear flow, it is done by assuming a velocity profile (Couette) in the entire simulation box, and we look at the resulting shear stress. However, in a rheological experiment one usually applies a shear stress at the surface, and the velocity profile develops in the whole bulk as an outcome. Without Newton's third law, the momentum does not propagate and we will not be able to reproduce the exact experimental situation. This deficiency severely limits the possibilities of simulating interesting and important phenomena such as shear bands, surface slip, or elastic instabilities. Additional work will be required to somehow make the BD equation obey the Newton's third law locally, while keeping the long diffusive time scale, and preferably without too many assumptions, and without incurring significant computational costs.

2 Soft blobs confined by hard walls

In the previous Chapter the soft blobs were modeled as a bulk system with periodic boundary conditions. Now we will take these blobs and confine them between two walls. The confined setup is crucial for a proper study of interfacial phenomena and therefore it is useful to spend some effort to develop an appropriate confinement methodology.

2.1 The main innovation: mirror-and-shift boundary condition

The kind of system that interests us is some soft fluid made up of blobs sized $\lambda = 2\,\mathrm{nm}$ or so, in contact with a flat surface such as silicon, which has a roughness of 0.2 nm, and therefore is much sharper than the blobs. Since we wish to run the simulation at the scale of a blob, it will be impossible to resolve the sharp details of the substrate. The sharpest confinement that one can hope for could be about the same size as the blob itself.

If we simply model the wall using a repulsive potential of the same range as the blobs, for instance $U(z) \approx k_B T e^{-z/\lambda}$ or any other reasonable function, the density profile across the wall will develop a handful of oscillations of a large amplitude, up to 50% of the bulk level, and a wavelength corresponding to the size of the blob $\lambda = 2\,\mathrm{nm}$. Clearly, this is a strong contradiction with numerous experiments for a variety of soft systems, characterized with neutron and x-ray reflectometry for example.

As will be detailed in Chapter 3, the neutron reflectometer FIGARO has accurate resolution in the range of 0.1-100 nm and could not detect any sign of density oscillations exceeding more than 1% of the bulk level, especially not on the length scale of a blob $\lambda \approx 2\,\mathrm{nm}$. These spurious density oscillations are in fact commonly reported in almost all other simulations [49], but not in self-consistent field theory (SCFT) calculations [50], with the exception of some density functional theory (DFT) studies [51] working on an atomic scale and assuming an extremely crisp wall and a perfectly spherical shape of the monomers. Our experimental situation, along with numerous other studies [52], does not meet these assumptions: the SiO_2 substrate, no matter how well polished, has a roughness of at least one oxygen atom, whereas the liquid

on top is far from just spherical balls, instead being molecules of a complicated shape with small hydrogens sticking out in many places, which means that the surface roughness is substantially greater than the smallest feature of the molecule, and therefore any density oscillations are smeared out of existence. Unfortunately, this assumption cannot be applied on the coarse scale of the blob, as one would need to assume a surface roughness much greater than λ, clearly at odds with reality.

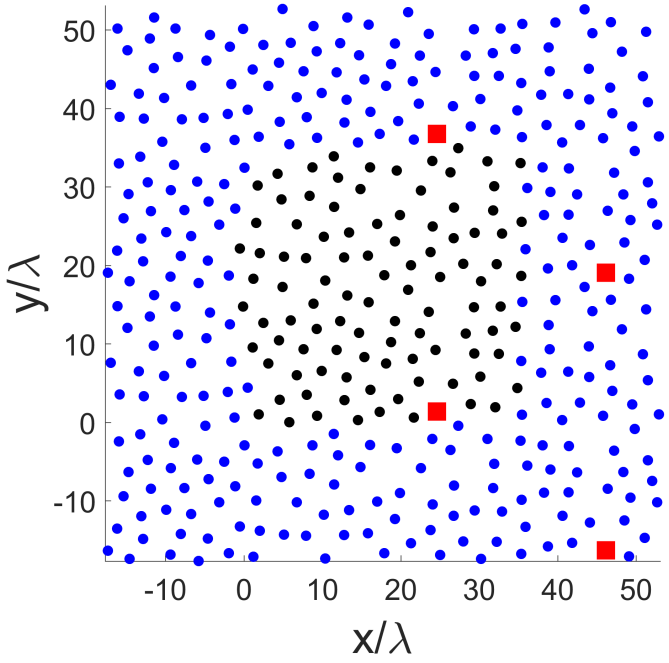

Figure 2.1 – A homogeneous liquid confining itself in the x-direction via mirror-and-shift boundary conditions, while being periodic in the y-direction. The red square marks various images of the same particle.

Our solution to this problem is presented in a Rapid Communication [53] reproduced in Appendix B. The main idea is to make the fluid confine itself via our novel mirror-and-shift boundary conditions, see Fig. 2.1. Although this approach may seem strange, especially from a chemist point of view, it does produce monotonic and close to maximally sharp density profiles, in good agreement with experiment at the appropriate length scale. It works really well for polymers too, even end-tethered polymer brushes. It is also quite straightforward to impose a shear flow. The computational cost is only marginally higher than a bulk simulation of the same size. Overall, we found that it is a very well suited method to model soft liquids in contact with hard walls.

To summarize, the use of mirror-and-shift boundary condition was crucially important to obtain realistic brush density profiles at an appropriate length scale.

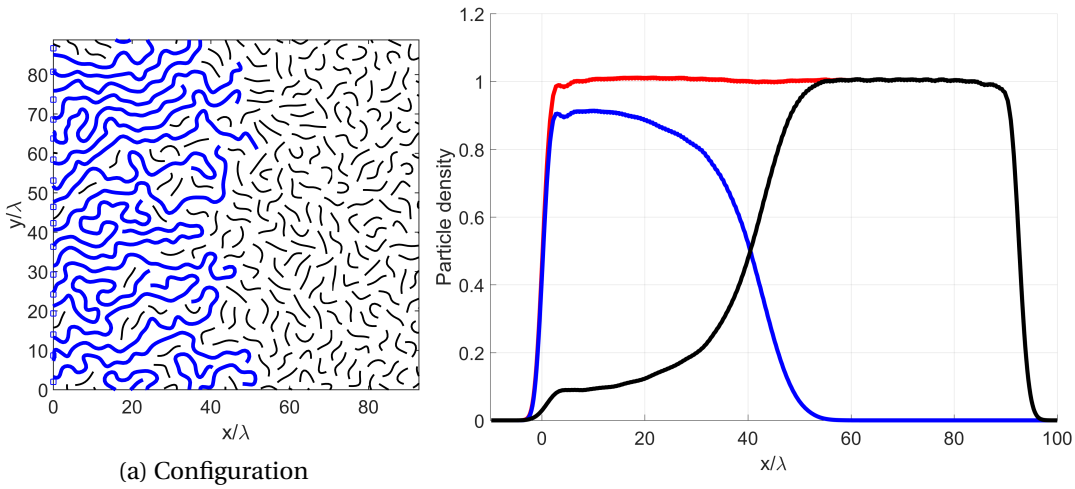

(a) Configuration

(b) Density profile

Figure 2.2 – Brush 1: wet and stretched

2.2 Dry brushes

Before turning on the shear flow in Chapter 3, we will briefly explore the kinds of brushes that are possible to realistically simulate with our setup. The easiest brushes are the ones which have sufficiently low density, examples of which are presented in Appendices B and C. In these cases we can use the exact same interaction parameters (excluded volume and chain stiffness), on both free and grafted chains, the only difference being that the grafted chains are attached to their designated grafting point, while the free chains are not attached anywhere, as their name implies.

The situation becomes more complicated with dense brushes. When the distance between the grafting points approaches the blob size, one must introduce a second, smaller blob potential to model the grafted chains [54]. If the blob size is not decreased, the polymer density on the brush will be considerably greater than the bulk value, which is unphysical. Eventually for a very high grafting density the simulation becomes numerically unstable as it is impossible to resolve chains grafted denser than their blob size. One must also keep in mind that the entire simulation box must run at the smallest scale of its fastest interaction, which would be the small blobs of the brush. This is not the most efficient arrangement, and eventually if the brush is very dense while the bulk fluid is quite dilute, one may need to switch to more complicated heterogeneous multiscale simulation techniques [55].

In the following preliminary calculations we have assumed the grafted chain length fixed at $N = 32$ blobs. We have varied the free chain length P and the grafting density

$$\sigma = \frac{\text{number of grafted chains}}{\text{box } y\text{-length}}, \tag{2.1}$$

as defined for a two-dimensional box. Four different systems were simulated, as specified in

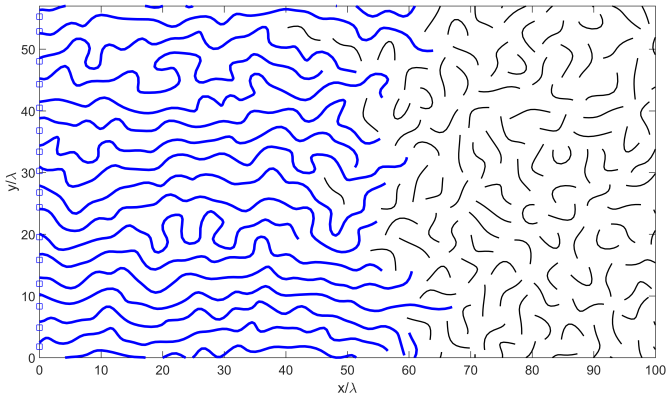

(a) Configuration

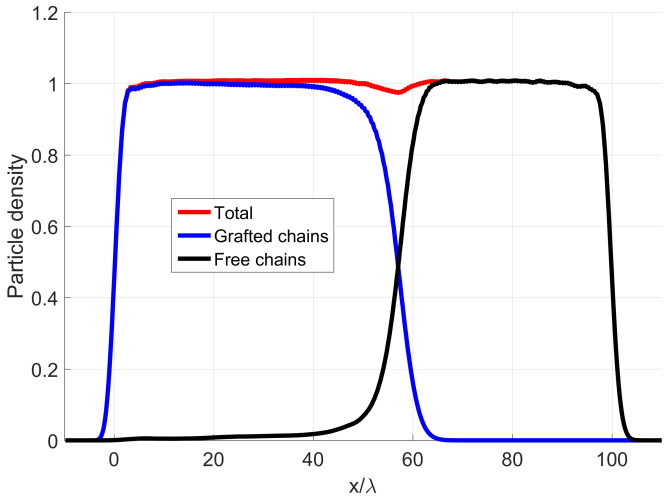

(b) Density profile

Figure 2.3 – Brush 2: border between wet and dry

Table 2.1. The blob size λ was kept constant and we have manually adjusted the brush spring length b, thereby changing the brush stiffness λ/b, in order to have a constant density of blobs across the entire simulation volume.

In Fig. 2.2 we show the conformation and monomer density profiles for a prototypical stretched polymer brush, as presented in most physics studies [56]. The grafting density is increased in Figs. 2.3 and 2.4, thereby gradually pushing the free chains out of the brush, and hence the brush becomes more and more “dry”. Finally, in Fig. 2.5 we increase the free chain length, which renders the brush even drier.

The interesting effect that we have found in this simulation, is that once the brush is sufficiently dry, it does not interdigitate with the bulk chains, resulting in a depleted layer at the brush-bulk interface. Since the brush and the free chains belong to the same chemical species, they should enthalpically adhere to each other. Nevertheless, in the case of very dry brushes, steric hindrance of entropic origin seems to prevent this adhesion, and may cause what is called an

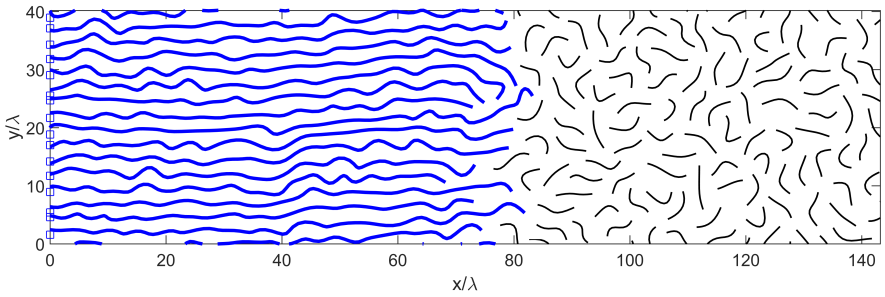

(a) Configuration

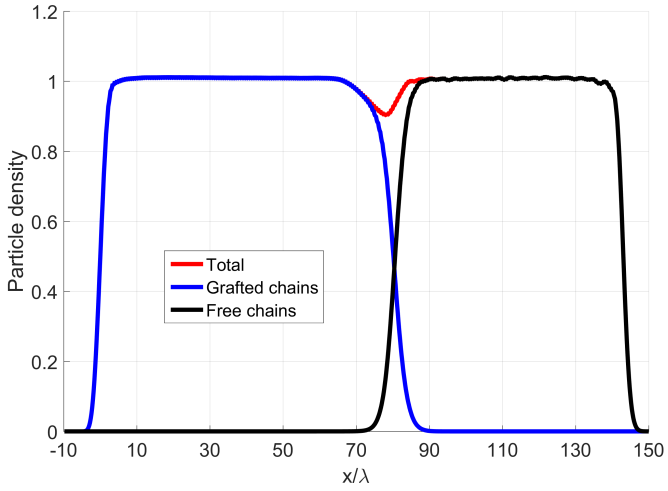

(b) Density profile

Figure 2.4 – Brush 3: dry brush

autophobic dewetting of the liquid layer from the brush. This phenomenon has been reported experimentally for PDMS brushes [57], and also in other computer simulations [58], as well as SCFT calculations [59].

As far as we know, there has not been any direct experimental proof of the depleted layer existence. We have made an attempt to detect this layer in our own neutron reflectometry measurements, using a polystyrene brush immersed in a polystyrene melt. So far the result has been negative and no depletion could be seen. There could be many reasons for this outcome: i) brush was too polydisperse, smearing out the depletion, ii) brush was not uniform enough, also smearing out the depletion, iii) brush not dense enough, iv) high temperature required to fully melt high M_w polystyrene (we reached 180 °C), destroyed the brush in the presence of oxygen. It may also be possible that the simulations are wrong and that some ingredient is still missing to correctly describe such a strongly heterogeneous system.

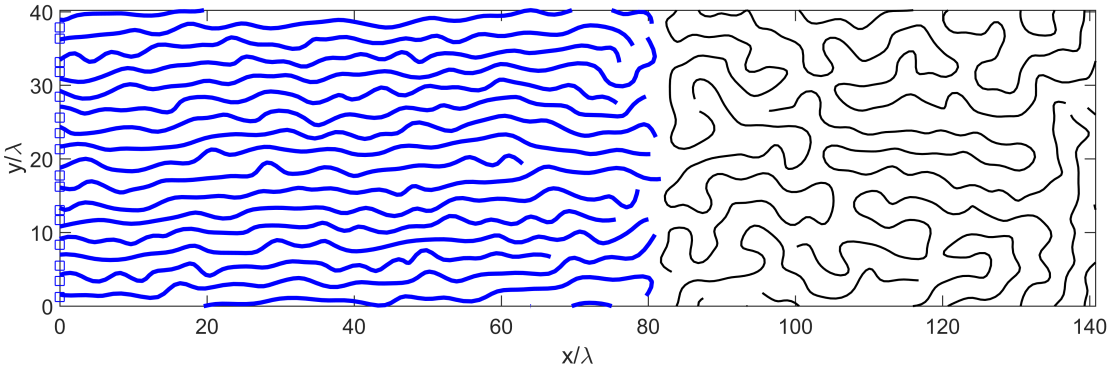

(a) Configuration

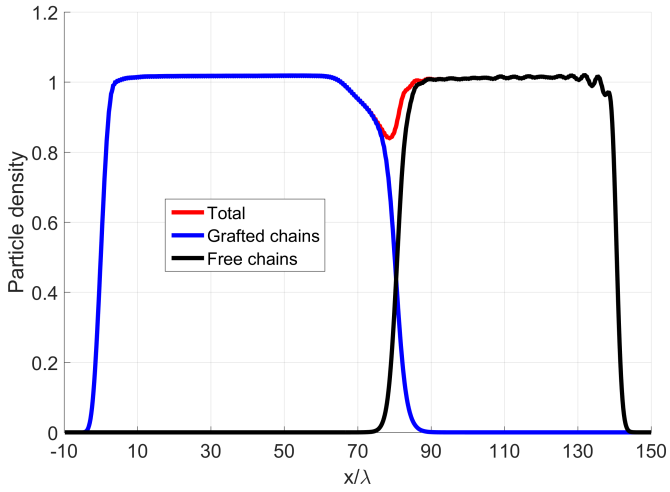

(b) Density profile

Figure 2.5 – Brush 4: very dry brush

Sample	1	2	3	4
State	wet	dry-wet border	dry	very dry
Free chain length P	4	4	4	64
Grafting density σ	0.09	0.14	0.2	0.2
Brush stiffness λ/b	0.67	0.6	0.36	0.44

Table 2.1 – Simulation parameters

3 Polymer brushes under shear flow

The end goal of our study was to understand how does a polymer brush behave under an applied shear flow. During the preparation of this thesis, an experimental study has been published [60] investigating a very similar system. There, the authors have applied a shear flow on a polystyrene brush in contact with a liquid polystyrene melt. The system was then rapidly quenched below its glass transition temperature, freezing the polymer conformation in place. The vitrified samples could later be characterized with neutron reflectometry, thus measuring *ex situ* the brush shape as a function the applied shear rate. The conclusion was that the brush shrinks and decouples from the bulk. The present Chapter could be considered to be a continuation of Ref. [60].

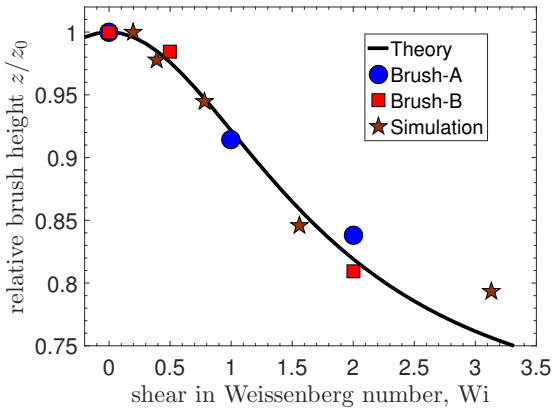

Figure 3.1 – Brush height under an applied shear flow. Two different grafting densities, Brush-A and Brush-B, have been measured experimentally, compared against one simulated system, and fitted with a phenomenological theory prediction.

In our measurements we have used a semi-dilute polymer solution, rather than a melt. A typical composition is 30% polystyrene in 70% diethyl phthalate (DEP). This allows a liquid system at room temperature, which could be more easily characterized *in situ* while shearing, also using neutron reflectometry. Various brushes of different grafting densities and chain

lengths have been examined, allowing us to draw broader conclusions on the brush behavior. We have used both experimental and computer simulation techniques, further guided by some theoretical insight, and the result of our efforts can be summarized in Fig. 3.1. The main conclusion is that the mean brush height shrinks quadratically with the applied shear rate, $\Delta z/z_0 \approx 1 - \mathrm{Wi}^2$. This behaviour is quite universal and has been observed using different brushes with greatly different grafting densities, using both polymer melts (Ref. [60]) and semi-dilute solutions (our data), in experiments as well as computer simulations. The main requirement to observe this effect is that the brush and the bulk chains must interpenetrate deeply enough and thereby be entangled with each other. Our computer simulation was performed using the combined innovations presented in Chapters 1 and 2. Therefore, in this final Chapter we will mostly focus on the experimental considerations.

A well controlled shear experiment is feasible up to shear rates of about $1000\,\mathrm{s}^{-1}$, and hence it is best to have both brush and free chains as high molecular weight as possible to increase their reptation time and enable coupling with the shear flow. The longest polymer we have tried was $600\,\mathrm{kg\,mol}^{-1}$ PS chains of dry thickness 5 nm (limited by the grafting-to technique). Such low density brushes (mushrooms) should in principle collapse under shear, but unfortunately they are too dilute to be visible with neutrons and therefore we could not detect any potential changes in their structure. Due to these practical considerations, the grafting-to brush had to be limited to about $200\,\mathrm{kg\,mol}^{-1}$ to have a successful measurement.

On the other hand, the brush density can be dramatically increased using grafting-from chemistry, and indeed we have tested PS brushes of up to 120 nm dry thickness. Unfortunately, these were too dense to allow a significant brush-bulk interpenetration and no reflectivity change could be observed under applied shear flow. Obviously, the brush collapse cannot go on forever, and will have to saturate once the brush becomes completely dry and all the free chains are fully expelled. For the very high density brushes, the saturation height is basically the same as the height at equilibrium, and therefore, they do not show any structural change upon an applied shear rate. As a result, we had to reduce the grafting density by about one third of the maximum, also keeping in mind that the grafting-from chemistry limits the molecular weight up to no more than $100\,\mathrm{kg\,mol}^{-1}$.

In the next section we briefly review the various chemical techniques for making polymer brushes, followed by an introduction to neutron reflectometry in Section 3.2. More results and the full details of the study are presented in Appendix C.

3.1 Polymer brush fabrication

The fabrication of polymer brushes is typically performed by attaching the polymer onto a surface via the “grafting-to” (our experiment Brush-A), “grafting-from” (our experiment Brush-B), or “grafting-through” methods [61].

The grafting-to [62] consists of tethering pre-formed polymer chains to a substrate, either

covalently or non-covalently. The non-covalent attachment can be fairly easily broken and reformed, and is sometimes called a pseudo-brush. In our experiments we have only used covalent bonding, which is more permanent and resistant to mechanical stress. It is usually achieved by terminating the anionic polymerization reaction with a suitably functionalized end-group or a short block that has a potential to bind to surfaces. A common functionalization available commercially is the carboxyl –COOH end group, although the amino $–NH_3$ group can also be found. Typically, the end-functionalized polymer is deposited (e.g. by spin-coating) on an activated substrate, which in our case is a self-assembled monolayer of an organosilane molecule, one end of which is immobilized on the silicon block, and the other end is on the outside waiting to react with the organic polymers. The system is heated above the polymer glass transition temperature, and allowed to react once in a melt state under oxygen-free conditions. Another possibility to increase the grafting density is to graft from a solvent of poor thermodynamic quality (near cloud point), such that the chains are collapsed, allowing more of them to be crammed on the same surface. The main advantage of the grafting-to approach is that very high molecular weights can be grafted. The limitation is that the grafting density is strongly restricted and the resulting brush is usually no more than a factor $\times 2$ denser than the mushroom regime.

In contrast, the "grafting-from" [63] method is based on growing the polymer chains from the surface itself by means of a "living", or controlled, polymerization protocol in which the initiator (or a chain-transfer agent) is bound to the surface. The grafting density can be very high, or reduced in a controlled fashion, depending on application requirements. However, such a protocol requires a special reactor vessel to accommodate a large substrate, and in this complicated environment the level of chemical purity cannot be guaranteed to be very high. Therefore, the polymerization reaction tends to terminate sooner, resulting in smaller molecular weight, and more polydispersity, with respect to a more traditional bulk polymerization reaction.

The polydispersity issue has been addressed using yet another grafting method, called "grafting-through" [64]. Here, the monomer is supplied from the back side of the semi-permeable substrate, therefore reacting more uniformly with all the growing chains. However, this technique is difficult to implement using our silicon substrates, which are not permeable to any monomers.

In our experiments, we have successfully observed the brush collapse using samples made by both grafted-to and grafted-from techniques. The necessary conditions are that the grafted chains are sufficiently long and not too dense to allow some interpenetration, but not too dilute either, so they can be seen with neutrons.

3.2 Neutron reflectometry

Neutron Reflectometry (NR) has proven to be indispensable [65], and so far the only method able to measure the brush structure directly *in situ* while it is being sheared. The main appeal

for neutrons is that they interact differently with different nuclear isotopes. When a sample is subject to neutron radiation of wavevector **k**, its every nucleus will emit secondary radiation in the form of spherical waves [66]:

$$\psi(\mathbf{r}) = \frac{b}{r} e^{ikr}, \tag{3.1}$$

where b is the so-called scattering length, which is a unique number for every isotope, and depends on the shape of the potential well of the nucleus as felt by the neutron via the strong nuclear interaction. For some nuclei, most notably hydrogen ^{1}H, the wave is scattered with a 180° phase shift and therefore the scattering length is negative: $b_{\mathrm{H}} = -3.74\,\mathrm{fm}$. In the case of deuterium ^{2}H, which is composed of one proton and one neutron, the scattering length is positive and drastically different: $b_{\mathrm{D}} = 6.67\,\mathrm{fm}$. This lucky discrepancy allows us to label the free and the grafted chains with different isotopes, and from the neutron point of view, the system appears much like depicted in Fig. 1, labeled with different "colours".

Another key advantage of neutrons as a probe is their non-invasive and non-destructive nature. One can record a neutron reflectometry spectrum from a polymer brush under shear, and rest assured that the system is almost not perturbed by radiation, unlike for example x-ray probes which can inflict heavy radiation damage to delicate organic samples such as ours. Also very important is that many engineering materials such as silicon or aluminium, are transparent for the neutrons. This enables access to interfaces buried deep within various devices, such as a shear apparatus.

Most materials such as polymers are a mixture of several nuclear species, not just one. Therefore, to quantify the scattered intensity of a particular material we shall use the average scattering length per unit volume, called the scattering length density, or SLD:

$$\mathrm{SLD} = \frac{1}{V} \sum_{j=1}^{J} b_j \tag{3.2}$$

where we add the contribution of every nucleus j inside a volume V. For instance, regular polystyrene C_8H_8 has the $\mathrm{SLD} = 1.4 \times 10^{-6}\,/\text{Å}^2$. Deuterated polystyrene C_8D_8, on the other hand, has a much greater $\mathrm{SLD} = 6.4 \times 10^{-6}\,/\text{Å}^2$. No such contrast is possible for optical or x-ray radiation, which are sensitive to the electronic structure instead. The numbers are calculated using tabulated values of the scattering length b, available from Ref. [67] or other standard references.

We will now briefly outline the theory of neutron reflectivity. Our discussion closely follows standard textbook material presented in Ref. [68], Chapter 3, and summarized in Fig. 3.2. In the reflection geometry, the neutron radiation is described by its wavevector transfer:

$$Q = |\mathbf{k}_{\mathrm{out}} - \mathbf{k}_{\mathrm{in}}| = 2k \sin\alpha \tag{3.3}$$

The phase of the neutron wave propagates slower in a material of a high SLD, with a phase

factor e^{inkr}, where

$$n = 1 - \delta = 1 - \frac{2\pi(\mathrm{SLD})}{k^2} \tag{3.4}$$

is the refractive index as perceived by the neutrons. As a consequence, it can be shown that inside a material m of a given $(\mathrm{SLD})_m$, the wavevector transfer is diminished to

$$Q_m^2 = Q^2 - 16\pi(\mathrm{SLD})_m, \tag{3.5}$$

with respect to the wavevector transfer Q in vacuum (or air since $\mathrm{SLD}_{\mathrm{air}} \approx 0$). The reflectivity between two layers $m = 1$ and $m = 2$ is the ratio of the outgoing and incoming wave amplitudes and is given by the Fresnel formula:

$$r_F(Q) = \frac{a_{\mathrm{out}}}{a_{\mathrm{in}}} = \left(\frac{Q_1 - Q_2}{Q_1 + Q_2}\right). \tag{3.6}$$

The above formula is only valid for a perfectly sharp interface, which is rarely justified in real experiments, and certainly not in ours. Instead, the interface usually has some finite roughness $\sigma_{1,2} > 0$, and it can be shown [69, 70] that this weakens the reflectivity to approximately

$$r(Q) = r_F(Q) \exp\left(-\frac{Q_1 Q_2 \sigma_{1,2}^2}{2}\right). \tag{3.7}$$

The reflectivity is scanned for different wavevector transfers Q, and as can be seen from Eq. (3.5), at some very small value $Q_c = \sqrt{16\pi(\mathrm{SLD})} \approx 0.01\,\text{Å}^{-1}$ for a silicon-air interface, the values of Q_m become imaginary, which leads to the total internal reflection: $R(Q < Q_c) \equiv 1$. Here are some other simple approximations valid in restricted Q-ranges (zero roughness is assumed here):

$$R(Q) = |r(Q)|^2 = \begin{cases} 1, & Q < Q_c \\ (3 - 2Q/Q_c)^2, & Q \gtrsim Q_c \\ \left(\frac{Q_c^2}{2Q^2}\right)^2, & Q \gg Q_c \end{cases} \tag{3.8}$$

The Fresnel formula can only be applied to a single interface, whereas our sample typically has the following composition: silicon – silicon dioxide – initiator – brush – bulk polymer solution. To describe the reflectivity from such a multi-layer, we must take into account all the (infinite) multiple reflections happening internally, as shown in Fig. 3.2. A standard way to do it is the Parratt's recursive formula [71] (an alternative and equivalent approach is the Abeles optical matrix formalism [72]). In our example we have $M = 3$ layers, plus one fronting (silicon), and one backing (polymer solution). There are four interfaces in total. The bottom-most interface has only one reflection,

$$\tilde{r}_{M,\infty} = r_{M,\infty} \tag{3.9}$$

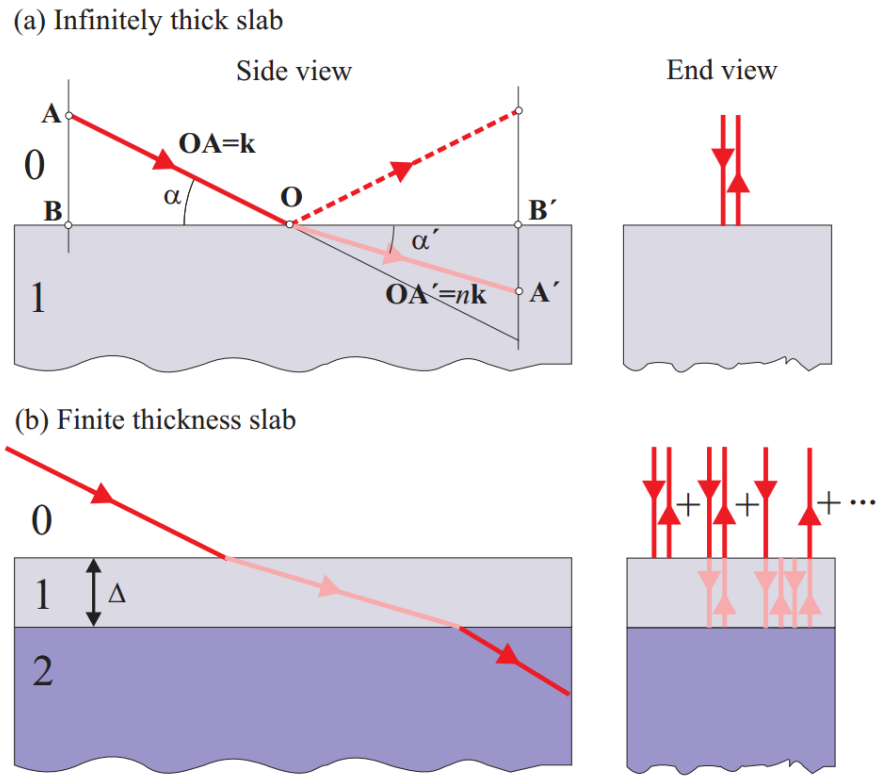

Figure 3.2 – Reproduced from [68] shows reflection and transmission from a slab of infinite (a) and finite (b) thickness. The finite slab is of thickness Δ and the total reflectivity is the sum of the infinite number of reflections, as indicated in the right panel of (b).

which can be calculated almost exactly by Eq. (3.7). Next layer up, the reflectivity is calculated using Parratt's formula:

$$\tilde{r}_{M-1,M} = \frac{r_{M-1,M} + \tilde{r}_{M,\infty} p_M^2}{1 + r_{M-1,M} \tilde{r}_{M,\infty} p_M^2}, \tag{3.10}$$

which takes into account all the infinite reflections shown in Fig. 3.2, panel (b). Here

$$p_m^2 = e^{iQ_m \Delta_m} \tag{3.11}$$

is the phase shift accumulated by the neutron wave upon traversing a layer of thickness Δ_m, while the internal wavevector transfers Q_m are all calculated from Eq. (3.5), and depend on the SLD of each layer. Parratt's Eq. (3.10) is repeated iteratively to calculate $\tilde{r}_{M-2,M-1}$, etc. until we arrive at the very first interface, $\tilde{r}_{0,1}$ which is silicon-silicon dioxide in our case. The absolute square of this reflectivity,

$$R(Q) = |\tilde{r}_{0,1}|^2 \tag{3.12}$$

corresponds to the measured intensity of the neutron beam at a given wavevector transfer

Q (see Eq. (3.3)), which in turn is scanned by changing the neutron wavelength $\lambda = 2\pi/k$, the incidence angle α, or both as is usually done in time-of-flight (TOF) reflectometers like FIGARO.

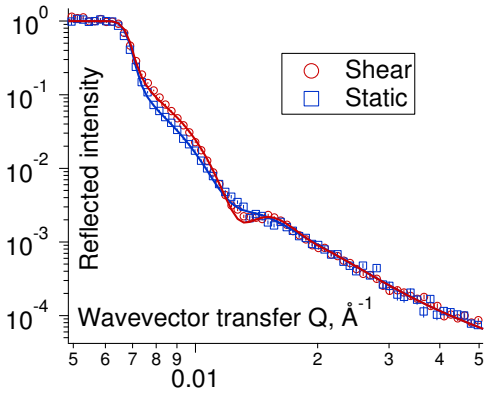

(a) Reflectivity spectrum. Circles and squares show experimentally measured data points, while solid lines are calculated from a model shown in Fig. 3.3b

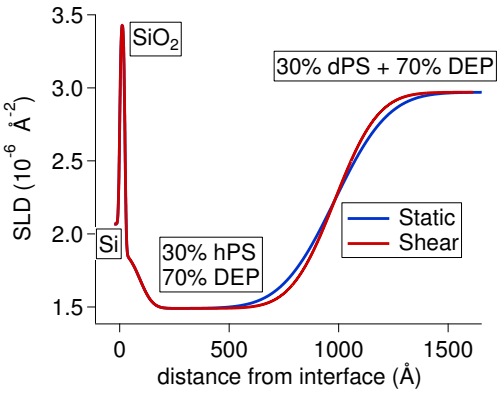

(b) Scattering length density profile obtained assuming a slab model and a Gaussian roughness between each layer. The fitting parameters are: layer thickness, layer SLD, and interface roughness.

Figure 3.3 – Neutron reflectometry data for an entangled polymer brush under shear flow, Wi = 2.0

A typical result of our experiments in displayed in Fig. 3.3a. We measure the reflected intensity of the neutron beam as a function of the wavevector transfer Q, for different shear rates ranging from static Wi = 0 (red circles) to the non-linear shear thinning regime at Wi = 2.0 (blue squares). If the sample structure is known (the final result shown in Fig. 3.3b), it can be used to exactly calculate the reflectivity spectrum. Unfortunately, the opposite is not true since we can only measure the reflected intensity $R = |r|^2$, but not the phase of the neutron wave, and half of the required information is not available. To describe the sample using the slab model, we require quite a few parameters: the SLD of each substance (5), plus the thickness of each layer (3), plus the roughness of each interface (4), therefore 12 numbers in total. The measured spectrum does not contain enough features to justify all this information, and therefore we must determine some of the parameters from other complementary measurements, such as the reflectivity of a dry brush in air, and a fully swollen brush in toluene, not shown here.

Once a plausible SLD profile has been constructed, the remaining details can be obtained by fitting the NR data. We have used standard Motofit software [73], which is based on calculations equivalent to those described above in Eq. (3.10). A genetic fitting algorithm is employed, which starts by first generating a random set of SLD profiles within a specified parameter range. Each guess is then converted into a corresponding reflectivity curve $R(Q)$,

which is compared against the experimental data points $R_0(Q)$ by calculating a fitness score:

$$\chi^2 = \sum_Q \frac{[\log R(Q) - \log R_0(Q)]^2}{\Delta R_0(Q)} \tag{3.13}$$

obtained by summing all the square differences between the predicted and the measured points, usually using the logarithmic scale in order to weigh the points more equally at both small and high Q, and also including the experimental error bars $\Delta R_0(Q)$. Other reasonable fitness functions with different weighing factors could be used as well, depending on the nature of the data.

The guess SLD profiles which have the best fitness scores (the smallest χ^2 values) are then combined to create a second generation of profiles, plus some random mutations to avoid getting stuck in a local minimum and explore the parameter space more thoroughly. This process is repeated for about 100 generations, and the best fitting result is plotted as a solid line in Fig. 3.3a, while its corresponding SLD profile is shown in Fig. 3.3b.

If the brush is not too dense, one can assume that the overall polymer concentration is fixed throughout the brush-bulk interface, and is equal to the concentration of the bulk solution:

$$\phi_{\text{grafted}}(z) + \phi_{\text{free}}(z) = \phi_{\text{bulk}} = 0.3 \tag{3.14}$$

This assumption can be verified by using a different contrast (e.g. a deutrated brush in a hydrogenated polymer solution, or various mixtures thereof). The SLD as obtained from the fit, Fig. 3.3b, is equal to the weighted sum of all species:

$$\text{SLD}(z) = \text{SLD}_{\text{hPS}}\phi_{\text{grafted}} + \text{SLD}_{\text{dPS}}\phi_{\text{free}} + \text{SLD}_{\text{DEP}}(1 - \phi_{\text{bulk}}) \tag{3.15}$$

These equations can be rearranged to find the brush density profile $\phi_{\text{grafted}}(z)$ in terms of the fitted $\text{SLD}(z)$ profile:

$$\phi_{\text{grafted}}(z) = \frac{(\text{SLD}(z) - \text{SLD}_{\text{DEP}}) - (\text{SLD}_{\text{dPS}} - \text{SLD}_{\text{DEP}})\phi_{\text{bulk}}}{\text{SLD}_{\text{hPS}} - \text{SLD}_{\text{dPS}}} \tag{3.16}$$

The roughness between the layers was modelled using a Gaussian function (see Eq. (3.6)), and therefore the fitted SLD has the shape of the error function $\text{erf}(z)$. This is the default and the simplest function to fit, and it seems to apply fairly well for our system. Other more complicated shapes have been proposed theoretically [74], but no such comparable theories are yet available for the entangled brushes under shear flow. Also, the brush-bulk interface is very rough and many different shapes could possibly fit the NR data, making it difficult to confirm or dismiss candidate theories. At the current stage of our research, it was sufficient to describe the brush by its thickness and roughness, using the simplest possible formulas. Our data strongly suggests that only the brush roughness is changing (decreasing) under shear, which means that the free chains are expelled, but the overall brush mass stays constant as it should be, if the sample is not degraded.

Most of our NR experiments were performed on the FIGARO neutron reflectometer located at the Institut Laue-Langevin (ILL) in Grenoble, France. It is a time-of-flight instrument with a broad wavelength band between 2 Å and 30 Å, provided by the cold source (liquid deuterium at 20 K) of the ILL reactor. A great advantage of this reflectometer is that the sample is fixed on a horizontal table, while the source and the detector arms rotate around to scan the different neutron wavevectors Q. The incident beam can be arranged either from top to bottom (for a dry brush in air), or from bottom to top (for a brush immersed in a liquid), depending on the needs of the sample. The horizontal geometry is particularly useful for experiments on free liquid surfaces and is also ideally suited for rheological studies which use a plate-plate or a plate-cone geometry.

3.3 Outlook

In all the brush systems that we have so far considered, both experimental and simulated, the brush collapse was occuring at a timescale governed by the reptation time of the free chains in solution, which in turn is determined by the free chain length P, (and the concentration). We have not found any dependence of the timescale on the parameters of the brush itself, such as its grafing density or the grafted chain length N. However, it must also be noted that in all the cases the free chains were equal or longer than the grafted chains: $P \gtrsim N$. The opposite regime where the grafted chains are much longer, $N \gg P$, was out of reach of our experimental capabilities. So far we do not know what happens in this regime where more than one free chain penetrates and entangles with every grafted chain. It may be possible that the brush starts collapsing at a shear rate of $\mathrm{Wi} \ll 1$, and the threshold should then depend on the brush parameters, rather than those of the bulk fluid. Such a brush-dominated system has been theoretically studied a long time ago [75], where the motivation is to dynamically control the slip length

$$b = \frac{\eta}{k} \tag{3.17}$$

where η is the bulk fluid viscosity and k is the friction coefficient with the brush-coated surface. An entangled polymer solution can have a very high viscosity $\eta \propto P^3$, and hence a very long slip length, provided that the friction coefficient k is small. In a brush-dominated regime the friction $k(\dot{\gamma})$ is thought to decrease before the shear thinning starts in the bulk, in which case one could expect a strong shear-dependent increase of the slip length b.

A brush-dominated entangled system has so far never been characterised experimentally, to the best of our knowledge. One would need to graft very long chains, let's say $M_w = 10^6\,\mathrm{g\,mol^{-1}}$ PS, which is in principle possible with standard grafting-to chemistry. However, when this brush swells once immersed in a bulk polymer solution, the brush density becomes much too low to influence the NR spectrum in a detectable way. To improve the detection limit, one will need to design an even sharper contrast between the free and the grafted chains, as well as longer neutron counting times.

In the meanwhile, computer simulations are readily available to investigate the brush-dominated, entangled regime $N \gg P$. This is considerably more time-consuming than the situation that we have simulated so far: $N = P/2$. Nevertheless, recent advances and the availability of affordable GPU computing make it relatively straightforward to tackle this challenge.

A Simulation of entangled polymer solutions

Authors: Airidas Korolkovas, Philipp Gutfreund, and Jean-Louis Barrat

An article published in the *Journal of Chemical Physics*, **145**, 124113 (2016)
(Received 23 March 2016; accepted 13 September 2016; published online 29 September 2016)

Author contributions:

Jean-Louis Barrat has formulated the problem and supervised the work.

Philipp Gutfreund has provided useful feedback and crucial support during the development and publication stages.

Airidas Korolkovas has proposed the mathematics to solve the problem, wrote the computer algorithm, analysed the data, and wrote the manuscript.

A16.03.0268

Simulation of Entangled Polymer Solutions

Airidas Korolkovas,[1, 2, a)] Philipp Gutfreund,[1] and Jean-Louis Barrat[1, 2]

[1)] *Institut Laue-Langevin, 71 rue des Martyrs, 38000 Grenoble, France*

[2)] *Université Grenoble Alpes, Liphy, 140 Rue de la Physique, 38402 Saint-Martin-d'Hères, France*

(Dated: 7 January 2017)

We present a computer simulation of entangled polymer solutions at equilibrium. The chains repel each other via a soft Gaussian potential, appropriate for semi-dilute solutions at the scale of a correlation blob. The key innovation to suppress chain crossings is to use a pseudo-continuous model of a backbone which effectively leaves no gaps between consecutive points on the chain, unlike the usual bead-and-spring model. Our algorithm is sufficiently fast to observe the entangled regime using a standard desktop computer. The simulated structural and mechanical correlations are in fair agreement with the expected predictions for a semi-dilute solution of entangled chains.

Keywords: Entanglement, computer simulation, semi-dilute polymer solution, coarse-graining

[a)] Electronic mail: korolkovas@ill.fr

I. INTRODUCTION

Simulation of entangled polymer solutions is a long standing challenge in the field of macromolecules. While it is possible to simulate polymer melts of sufficiently long chains where entanglement effects become visible, achieving a comparable result in polymer solutions remains evasive, despite ongoing increase in computer speed and algorithm efficiency. To start with, entanglement is not an interaction *per se* that one could insert in the simulation code. Rather, it is an emergent phenomenon due to the uncrossability of very long, interpenetrating polymer chains. The main challenge from the numerical point of view is to resolve chain motion with sufficient accuracy for there to be no crossings over a time span exceeding the one required for a chain to diffuse a distance equal to its own size.

Most of the previous simulation effort on entanglement was geared for polymer melts rather than their solutions. A popular model by Kremer and Grest[1] (KG) designed for melts is based on hard, impenetrable beads tightly bound by stiff nonlinear springs. The beads are often modeled by the steep repulsive part of the Lennard-Jones potential, also known as the Weeks-Chandler-Andersen (WCA) potential, whereas the connectivity is enforced by finitely extensible nonlinear elastic (FENE) springs. Alternatively, an even better barrier against crossings is obtained in lattice-based simulations[2], with the downside that the chain conformation is unrealistically limited to only a handful of coordinations which depend on the arbitrary choice of the lattice (cubic, face-centered cubic, etc.)

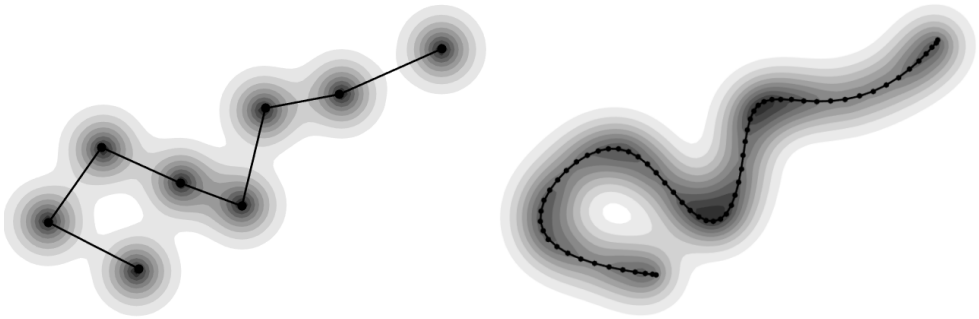

(a) Bead-and-spring model: $J = N = 8$.

(b) Pseudo-continuous model: $J = 8N = 64$.

FIG. 1: Two models of the same molecule with N degrees of freedom but different number of particles J. Shading denotes the repulsive potential Φ of range λ.

In a polymer melt the entanglement length is typically within a factor of 10-100 longer than the natural interatomic distances, which is not very far apart and so the KG method is an adequate approach to simulate the liquid. However, if we dilute the system by adding solvent, while at the same time increase molecular weight to maintain a high degree of chain interpenetration (the semi-dilute regime), the computational time becomes a major issue. The entanglement length is now much greater than the interatomic scale, and the rate of chain collision is many orders of magnitude lower than the timescale required to follow the hardcore WCA+FENE interactions. Often in applications we want to focus on the physics of entanglement and we are less interested in the small features on the atomic scale. The main strategy is hence to simulate the polymers at a coarser scale[3,4], which basically means softer beads and looser springs. Alas, this quickly opens up gaps along the backbone (see Figure 1a), through which the chains can cross each other and the entanglement behavior is lost.

To mimic the effects of entanglement, several recent studies have introduced temporary *attractive forces*, called slip-springs[5–8] or slip-links[9,10], between nearby beads. As an extreme example[11], one can replace the entire chain by just a single particle at the expense of having to invent and justify effective entanglement interactions with other such "particles".

A rival camp of thought introduces additional *repulsive forces*. One suggestion is to topologically detect the segments which have crossed during the time step, and then repel them back using the Twentanglement[12] algorithm. On second thought, why bother with topology at all instead of simply repelling the nearby segments even before they had a chance to cross, using the so-called segmental repulsive potential (SRP)[13–15]?

In our recent work[16] we briefly mentioned a model which takes the SRP strategy even further and completely blurs the distinction between "bead" and "segment". The present paper explores this idea in much greater detail. The chain in theory is a fully continuous curve with N degrees of freedom, which is discretized for computational purposes by drawing as many samples $J \gg N$ as needed such that the distance between consecutive points $|\mathbf{R}_j - \mathbf{R}_{j-1}| \ll \lambda$ is much smaller than the range of the excluded volume force, as shown in Figure 1b. A soft Gaussian potential is perfectly adequate to repel such pseudo-continuous chains, whereas a linear Hookean spring interaction keeps them connected. The time evolution is described by a stochastic first order equation of motion known as the Brownian thermostat. The random force is truncated at high frequencies, which reduces its peak

amplitude, thus making chain crossings even less likely.

One alleged disadvantage is that we end up with a very dense and computationally demanding N-body (or rather, $(J \gg N)$-body) problem. To mitigate this issue, in Section IV we propose an approximate algorithm which uses two staggered grids and splits the Gaussian potential into its short- and long-range contributions, each of which is very fast to evaluate. The code is highly parallel and is straightforward to further accelerate using GPU computing.

To validate our algorithm we have performed a series of computer simulations in the regime which can be mapped to semi-dilute polymer solutions. The obtained chain trajectories were analyzed to determine various structural and mechanical correlations. In particular, the self-diffusion coefficient scaled as $D \propto N^{-2}$, and the longest relaxation time scaled as $\tau_d \propto N^3$ for long $N > 256$ chains. While our model does not explicitly prevent chain crossings, it does suppress them sufficiently for the reptation behaviour to emerge, thus reaching a fair agreement with well-known experimental and theoretical facts.

II. THE CONTINUOUS MODEL

FIG. 2: Typical state of semi-dilute polymer in two dimensions. The chains have $N = 16$ degrees of freedom and keep a distance of about λ from each other.

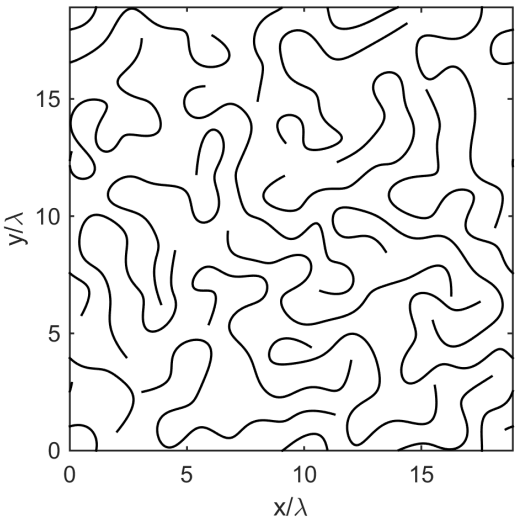

FIG. 3: $C = 16$ chains with $N = 32$ degrees of freedom in three dimensions. Yellow color indicates the tension $|\partial \mathbf{R}/\partial s|^2$, see Eq. (1).

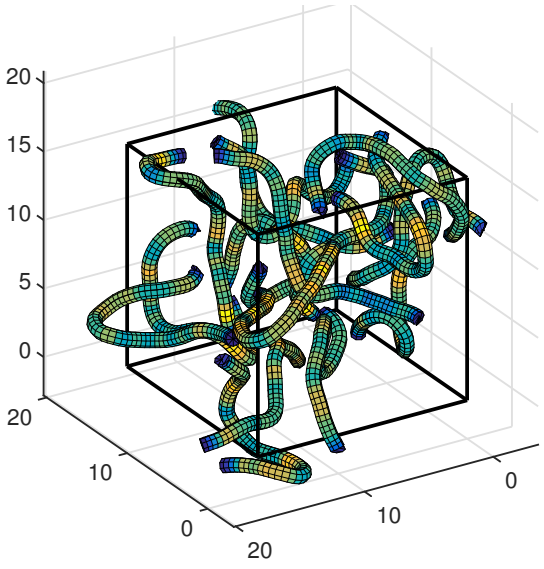

We consider a semi-dilute polymer solution consisting of a number C of chains in a

volume V, with periodic boundary conditions as shown for clarity in Figure 2 for the two dimensional case. All subsequent calculations will be carried out in the three dimensional case, illustrated in Figure 3. Each chain is nominally composed of N monomers, or blobs, linked by a linear spring interaction of length b. We start with the continuous coil, or Edwards model[17], where the c^{th} chain at time instant t is represented by a continuous path $\mathbf{R}_c(t,s)$ with the monomer label $s \in (0,1)$. The energy of a configuration is

$$H = \frac{3k_BT}{2Nb^2}\sum_{c=1}^{C}\int_0^1 ds\,\left|\frac{\partial \mathbf{R}_c}{\partial s}\right|^2 + \frac{N}{2}\sum_{c=1}^{C}\sum_{c'=1}^{C}\int_0^1\int_0^1 ds\,ds'\,\Phi[\mathbf{R}_c(s)-\mathbf{R}_{c'}(s')]. \qquad (1)$$

The first term is the attractive spring interaction of entropic origin,[18] while the function Φ denotes the excluded volume interaction, with $v \approx \lambda^3$ being the excluded volume parameter:

$$\Phi(\mathbf{r}) = vNk_BT\delta(\mathbf{r}) \approx Nk_BT\exp\left(-\frac{\mathbf{r}^2}{2\lambda^2}\right). \qquad (2)$$

The Dirac delta $\delta(\mathbf{r})$ approximation is commonly used in continuum theories, while the Gaussian approximation with its finite range $\lambda \approx b$ is more suited for numerical calculations[19].

At equilibrium, the model can be most readily identified with a semi-dilute polymer solution at density ρ and molecular weight M_w. Scaling theory[18] predicts the number of blobs and their size to scale as

$$N \propto \rho^{5/4}M_w \quad \text{and} \quad \lambda \propto \xi \propto \rho^{-3/4}. \qquad (3)$$

This mapping is valid for semi-dilute solutions $\rho^* \ll \rho \ll \rho^{**}$, but could also be extended to melts, provided that the correlation length $\lambda(\rho_{\text{melt}}) \gg b_0$ is substantially greater than the size of an atom b_0, which may be a reasonable assumption for some chemical species. A blob particle contains both the polymer and the associated solvent, so we do not add explicit solvent particles.

Far from equilibrium, such as under a strong shear flow, or just in general whenever the chains are highly stretched as in a polymer brush, the above mapping breaks down. The simulation can still be performed, but one will be obliged to use more blobs $N > N_{\text{eq}}$ and a sharper potential $\lambda < \lambda_{\text{eq}}$ until eventually the atomic scale is reached and one may as well switch back to a Kremer-Grest type of approach.

In a semi-dilute solution the hydrodynamic interactions are screened and are not important[20] for distances beyond $\xi \approx \lambda$, and therefore are not included in the model.

The chain dynamics can then be described by the stochastic Brownian equation of motion:

$$\zeta \frac{\partial \mathbf{R}_c(t,s)}{\partial t} = \left(\frac{3k_BT}{Nb^2}\right) \frac{\partial^2 \mathbf{R}_c(t,s)}{\partial s^2} - N\nabla U(\mathbf{r})_{\mathbf{r}=\mathbf{R}_c(t,s)} + \sqrt{2k_BT\zeta}\,\mathbf{W}_c(t,s) \tag{4}$$

where $\zeta = 6\pi\eta_s bN$ is the friction coefficient of the center of mass, $\mathbf{W}_c(t,s)$ is the Wiener process satisfying $\langle \mathbf{W}_c^\alpha(t,s)\mathbf{W}_{c'}^\beta(t',s')\rangle = \delta^{\alpha\beta}\delta_{cc'}\delta(t-t')\,\delta(s-s')$, and

$$U(\mathbf{r}) = \sum_{c=1}^{C} \int_0^1 ds\, \Phi[\mathbf{r} - \mathbf{R}_c(s)] \tag{5}$$

$$\approx \sum_{c=1}^{C} \sum_{j=1}^{J} \Phi_0(\mathbf{r} - \mathbf{R}_{c,j}) \tag{6}$$

is the total excluded volume field. The natural time unit is the microscopic Rouse time

$$\tau = \frac{6\pi\eta_s b^3}{k_BT}, \tag{7}$$

which is roughly the time it takes one blob to diffuse a distance equal to its own size. In contrast, the momentum relaxation time

$$\tau_m = \left(\frac{m}{6\pi\eta_s b} \approx \frac{\rho_0 b^2}{\eta_s}\right) \ll \left(\tau \approx \frac{\eta_s b^3}{k_BT}\right) \tag{8}$$

would be the time during which the thermal velocity $\langle \mathbf{v}^2\rangle = 3k_BT/(2m)$ of the coarse particle $\lambda \approx b$ decorrelates significantly from its initial value. The particle mass m is assumed to contain both the polymer and the surrounding solvent molecules, so the density $\rho_0 \approx 1\,\mathrm{g/cm}^3$ refers to the overall density of the liquid. The Brownian equation (4) of motion is justified as long as the above inequality $\tau_m \ll \tau$ holds and we can ignore inertia. In terms of physical polymer density ρ and using Equation (3), the inequality can be expressed as

$$\rho \ll \rho_0 \left(\frac{b_0\eta_s^2}{\rho_0 k_BT}\right)^{4/3} \approx \rho^{**} \tag{9}$$

where $b_0 \approx 1\,\mathrm{nm}$ is the size of the physical monomer. Highly concentrated $\rho \gtrsim \rho^{**}$ solutions and melts were not considered in the current study, but we can say that in this regime one must abandon the Brownian equation and use a second order equation of motion, such as the popular Dissipative Particle Dynamics[21] integrator. The pseudo-continuous $J \gg N$ model can still be applied similarly as in the present study, since the mechanistic chain model and the equation of motion employed to propagate that model in time are two separate things.

On passing, we emphasize that the linear spring interaction is appropriate for simulations of phenomena with a timescale $t \gg \tau$. As a counterexample, for an extreme shear flow $\dot\gamma \gtrsim \tau^{-1} = 10^6\,\mathrm{s}^{-1}$ one will require more expensive FENE springs.

III. THE DISCRETE MODEL

In this section we will provide a discrete counterpart to the continuous equation of motion, Equation (4), and integrate it over a short time step Δt. The details get a bit technical, but are worth following since a properly designed discretisation scheme is essential to suppress chain crossings.

The main idea is to sample the continuous backbone $s \in (0,1)$ using a finite number $j = 1, 2, \ldots, J$ of discrete points as shown in Figure 1. The potential of a fictitious j-"particle" centered around $s_0 = (2j-1)/(2J)$ is

$$\Phi_0(\mathbf{r}-\mathbf{R}_j) = \int_{s_0-1/(2J)}^{s_0+1/(2J)} ds\, \Phi(\mathbf{r}-\mathbf{R}(s)) \approx \left(\frac{N}{J}\right) k_B T \exp\left(-\frac{(\mathbf{r}-\mathbf{R}_j)^2}{2\lambda^2}\right). \tag{10}$$

The choice $J = N$ corresponds to the simplest bead-and-spring model, which has gaps that allow chains to cross their paths. The choice $J = 2N$ is similar to the situation obtained using SRP, except that in our case the potential on both the "beads" and the "segments" is exactly the same. In general, we will consider $J \gg N$ such that the largest gap $\texttt{max}|\mathbf{R}_j - \mathbf{R}_{j-1}| \ll \lambda$ is much smaller than λ. There exists a certain threshold, similar to the Nyquist rate in signal processing, beyond which the discrete model behaves just like the continuous Edwards chain would. We found that at equilibrium $J/N = 4$ is sufficient, whereas more points may be required in situations where the chains are stretched, such as under shear or in a polymer brush, or for more flexible chains with $\lambda < b$.

As is well known, the configuration of any given chain can equivalently be described by a set of Rouse[22] modes $\mathbf{a}_n = \int_0^1 ds\, \mathbf{R}(s)\cos(\pi n s)$, where $n = 0, 1, 2, \ldots, (N-1)$. In this work we retain $(N-1)$ modes $+1$ center of mass to be consistent with the number of blobs N. The equation of motion in the Rouse domain becomes

$$\zeta \frac{\partial \mathbf{a}_n(t)}{\partial t} = -\left(\frac{3\pi^2 n^2 k_B T}{N b^2}\right)\mathbf{a}_n(t) + \tilde{\mathbf{F}}_n(t) + \sqrt{(1+\delta_{0n})k_B T \zeta}\,\tilde{\mathbf{W}}_n(t) \tag{11}$$

where the Wiener process is $\langle \tilde{\mathbf{W}}^{\alpha}_{cn}(t)\tilde{\mathbf{W}}^{\beta}_{c'n'}(t')\rangle = \delta^{\alpha\beta}\delta_{cc'}\delta_{nn'}\delta(t-t')$ and the spectral force

$$\tilde{\mathbf{F}}_n = -N\int_0^1 ds\, \cos(\pi n s)\nabla U(\mathbf{r})_{\mathbf{r}=\mathbf{R}(s)} \tag{12}$$

$$\approx -\left(\frac{N}{J}\right)\sum_{j=1}^{J}\cos\left(\frac{\pi(2j-1)n}{2J}\right)\nabla U(\mathbf{r})_{\mathbf{r}=\mathbf{R}_j} \tag{13}$$

is the discrete cosine transform of the real force. We must now integrate the continuous Rouse equation (11) over a discrete time interval Δt. The main limitation on the time step

is that two blobs repelling at maximum strength should not move further than their own size. This leads to $\Delta t \lesssim (6\pi\eta_s b^3)/k_B T = \tau$. However, when we integrate the random force over the same time step, the mean blob displacement is $\sqrt{\langle \Delta \mathbf{R}^2 \rangle} = \sqrt{6 k_B T \Delta t/(6\pi\eta_s b)} = \sqrt{6}\, b$. This distance is $\sqrt{6} \approx 2.4$ times greater than the coarse-grained excluded volume force range $\lambda = b$, and therefore would cause plenty of chain crossings. It is not surprising, since the concept of a "blob" (see Equation (3)) was originally justified only in the thermodynamic long time $t \to \infty$ limit, while if observed at short times $t \approx \tau$ there are of course no such actual blobs. Therefore, to derive any meaningful information from our blob-based model, we must truncate the sampling rate of the random force. In particular, we propose to update the random force only once every $M \gg 1$ steps, while between the updates the blobs move ballistically with fixed increments of magnitude

$$\sqrt{\langle \Delta \mathbf{R}^2 \rangle} = \sqrt{\frac{6 k_B T \Delta t}{(6\pi\eta_s b) M}} \tag{14}$$

and random direction. In other words, we smooth out the Dirac delta correlation over a finite time span $(M\Delta t)$ while keeping the power spectrum at zero frequency unchanged, so that the long time properties are preserved but the instantaneous value of the force is smaller by $1/\sqrt{M}$. Specifically, the mean squared displacement over a long time $t \gg (M\Delta t)$ remains the same as in the continuum theory: $\langle \Delta \mathbf{R}^2 \rangle = 6 b^2 t/\tau$. We have used $M = 120$, which gives a random displacement of $(\sqrt{6/120} \approx 0.22) b$ per step, sufficiently small to be repelled by the excluded volume force which pushes the two blobs apart by one $\lambda = b$ during the same time step Δt. A larger value of M makes chain crossings less likely (see Figure 11), at the expense of having to discard more short-time correlation data as unphysical, such as seen at short time scales in Figure 8b.

The solution to Equation (11) is written as

$$\mathbf{a}_n(t + \Delta t) = \left\{ \mathbf{a}_n(t) + \frac{\Delta t}{\zeta} \tilde{\mathbf{F}}_n[\mathbf{a}_n(t)] + \sqrt{\frac{2 k_B T \Delta t}{\zeta M}}\, \tilde{\mathcal{R}}_n^{(3)} \right\} \Big/ \left(1 + \frac{\Delta t}{\tau_n} \right), \tag{15}$$

where the spring relaxation times are

$$\tau_n = \frac{1}{3\pi^2} \left(\frac{6\pi\eta_s b^3}{k_B T} \right) \left(\frac{N}{n} \right)^2, \tag{16}$$

and the symbol $\tilde{\mathcal{R}}_n^{(3)}$ stands for an isotropic random vector of mean zero and variance

$$\langle [\tilde{\mathcal{R}}_n^{(3)}]^2 \rangle = \frac{3}{2}(1 + \delta_{0n}). \tag{17}$$

To further minimize the largest possible displacement due to the random force, we use a uniform spherical distribution. First, generate $j = 1, 2, \ldots, N$ vectors $\mathcal{R}_j^{(3)}$ of fixed length $\sqrt{3}$ and random orientation. This corresponds to adding the random displacements directly on the beads shown in Figure 1a. The spectral displacements are then obtained by

$$\tilde{\mathcal{R}}_n^{(3)} = \frac{1}{\sqrt{N}} \sum_{j=1}^{N} \mathcal{R}_j^{(3)} \cos\left(\frac{\pi(2j-1)n}{2N}\right). \tag{18}$$

One can verify that the variance is indeed

$$\langle [\tilde{\mathcal{R}}_n^{(3)}]^2 \rangle = \frac{3}{N} \sum_{j=1}^{N} \cos^2\left(\frac{\pi(2j-1)n}{2N}\right) = \frac{3}{2}(1 + \delta_{0n}) \tag{19}$$

as imposed by Equation (17). It must be clear that the random force described above only makes sense in the limit of many steps $t \gg (M\Delta t)$. Our model does not contain any sensible microscopic information on the scale of a single step $t \lesssim (M\Delta t)$, where it cannot and should not be mapped to any real system.

IV. COMPUTATION OF THE EXCLUDED VOLUME FORCE

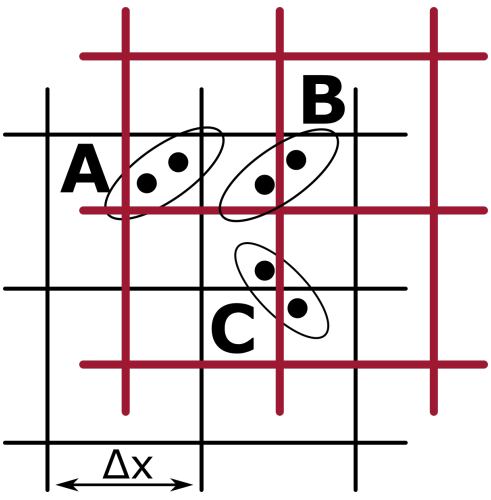

FIG. 4: Interacting particles as seen by two staggered grids. Line color and thickness serve only as a visual aid.

The most time demanding step of the program is the calculation of the field gradient $\mathbf{F} = -\nabla U(\mathbf{r})$ at the position of every j-particle. The use of standard domain decomposition techniques[23] would require an execution time proportional to the total number of

particles CJ times the number of neighbors that each particle has, const. $\times\, J/N$, in total $O(CN(J/N)^2)$, which is a factor $(J/N)^2$ higher than a corresponding bead-and-spring simulation. Here we propose a mesh-based approximation which only takes $O(CN\log(CN)) + O(CJ)$ computer time and does not suffer a significant slowdown in the important regime $J/N \gg 1$. We will need two rectangular grids, each having a large mesh size $\Delta x \lesssim \lambda$, and the origin staggered along all axes by half a spacing $\Delta x/2$ with respect to each other, as shown in Figure 4. The force on every particle $\mathbf{F}(\mathbf{R}_{c,j})$ is evaluated twice, using each of the two grids, and the average is fed to the equation of motion. We take into account the "short range" and the "long range" contributions. All particle pairs which share the same cell, such as the pair A, will interact via a short range routine. The pairs which fall into separate cells, such as the pair C, will interact via a long range routine. Lastly, borderline pairs such as B will interact via short range in one of the grids, and via long range in the other grid.

The first step in the force routine is to bin the coordinate $\mathbf{R}$ of each j-particle into its nearest cell in the central box:

$$\begin{pmatrix} k_x \\ k_y \\ k_z \end{pmatrix} = \texttt{ceil}\left(\left[\mathbf{R} - V^{1/3}\texttt{floor}\left(\frac{\mathbf{R}}{V^{1/3}}\right)\right]/\Delta x\right) \tag{20}$$

where each 3D-cell index is $k_\alpha = 1,\, 2,\, \ldots,\, K$, with $K = \texttt{round}\left(V^{1/3}/\Delta x\right)$ the total number of cells per spatial dimension, and $\Delta x = V^{1/3}/K$ re-adjusted so that K is always an integer.

The short range routine is based on the linearization of the Gaussian force $\mathbf{F} = \mathbf{r}e^{-\mathbf{r}^2/(2\lambda^2)} \approx \mathbf{r}$ valid for $r \lesssim \lambda$. That way, the force on the particle located at $\mathbf{R}_p$ due to all the other nearby Q particles which are in the same cell, is

$$\mathbf{F}_{\text{short}}(\mathbf{R}_p) = \sum_{q=1}^{Q}(\mathbf{R}_p - \mathbf{R}_q) = Q\mathbf{R}_p - \sum_{q=1}^{Q}\mathbf{R}_q. \tag{21}$$

The computational task is to count the total number Q of particles in each cell, and sum all their coordinates $\sum \mathbf{R}_q$, followed by the cheap algebra of Equation (21), which costs little more than the very cheapest step in the code, Equation (20).

The interactions of particles across cell boundaries are taken into account by the long range routine. It is accurate for separations $r \gtrsim \Delta x$ and is the standard particle-mesh calculation[24] which has been used for soft Gaussian potentials before[25,26]. Here we recycle

the particle count Q to reshape it into a three dimensional array $\rho(\mathbf{r}')$ and imagine that the particles are all located at the center $\mathbf{r}' = (k_x\hat{\mathbf{x}} + k_y\hat{\mathbf{y}} + k_z\hat{\mathbf{z}})\,\Delta x$ of their corresponding cell. The force on every particle in a given cell $\mathbf{r}$ is then obtained by the convolution theorem:

$$\mathbf{F}_{\text{long}}(\mathbf{r}) = \texttt{IFFT}\left\{\texttt{FFT}[\rho(\mathbf{r}')]\cdot\texttt{FFT}\left[\mathbf{r}'e^{-\mathbf{r}'^2/(2\lambda^2)}\right]\right\} \tag{22}$$

where `(I)FFT` is the standard (Inverse) Fast Fourier Transform in three dimensions, which automatically incorporates the periodic boundary conditions. The total force on each particle is the sum

$$\mathbf{F}_{\text{total}} = \left\langle \mathbf{F}_{\text{short}} + \mathbf{F}_{\text{long}} \right\rangle_{\text{grid}}, \tag{23}$$

averaged over the two grids.

The error suffered by this algorithm is eventually smeared over the redundant j-particles and the final spectral force in Equation (13) is more trustworthy than it may seem judging from the real space perspective. We also wish to draw attention to the fact that even the most accurate evaluation of the interparticle force is only exact at one particular instant in time t, after which it is inevitably subject to the bias of the time integrator, which is usually $o(\Delta t^2)$ accurate in itself. Consistent with these reasons, we found that the simulation results were virtually identical for all grid sizes $\Delta x \leq \lambda$, so we kept $\Delta x = \lambda$ for maximum speed.

V. SIMULATION ALGORITHM

In this section we consolidate all our ideas into an algorithm which is the basis for the computer code. The goal is to start with a configuration $\mathbf{a}_n(t)$ as the input and predict a thermodynamically likely future configuration $\mathbf{a}_n(t + \Delta t)$ as the output.

1. **Generate the $C \times N$ random vectors** $\mathcal{R}_{c,n}$ of unit length $\sqrt{3}$ and random orientation. This step is updated only once every $M = 120$ iterations.

2. **Sample the chain conformation in real space** using J points indexed at regular intervals along the backbone s:

$$\mathbf{R}_j = \mathbf{a}_0 + 2\sum_{n=1}^{N-1}\mathbf{a}_n\cos\left(\frac{\pi(2j-1)n}{2J}\right) \tag{24}$$

with $j = 1, 2, \ldots, J$. These locations will be used to compute the excluded volume interaction between different chains. The complexity of this step is $O(J\log J)$ per chain, if evaluated using an efficient `FFT`-based code[27].

3. **Evaluate the excluded volume force** $\mathbf{F}_j = -\nabla U(\mathbf{r})_{\mathbf{r}=\mathbf{R}_j}$ on each j-particle using the approximate Equation (23). Then, convert it to the Rouse domain $\tilde{\mathbf{F}}_n$ using Equation (13).

4. **Integrate the equation of motion** using the Backwards Euler formula in Equation (15) to obtain the new configuration $\mathbf{a}_n(t + \Delta t)$ which now includes the random walk, the excluded volume and the spring forces.

5. Repeat steps 2-4 for $M = 120$ iterations using the same set of random displacements. Then, start over from step 1.

6. As a final remark, we note that the random numbers $\mathcal{R}_{c,j}$ do not instantaneously add up to zero, which leads to an overall diffusion of the entire system. Hence, we manually reset the system center of mass by translating all the particles

$$\mathbf{R}_{c,j}(t) \to \mathbf{R}_{c,j}(t) - \frac{1}{CJ}\sum_{c',j'}^{C,J} \mathbf{R}_{c',j'}(t) \tag{25}$$

which guarantees $\sum \mathbf{R}_{c,j} = \text{const.} = 0$ at all times. This correction is required to remove the finite-size artifact from the trajectories, as explained in the appendix of reference[1].

Before the start of the simulation, we need to decide on all the input parameters. As an example, suppose that we want to simulate polystyrene of molecular weight M_w dissolved in toluene at density $\rho^* \ll \rho \ll \rho^{**}$. Using the mapping in Equation (3) we convert this into the number of blobs N and the blob size λ. Depending on the chemical species and temperature, one then has to choose the stiffness λ/b and the excluded volume v/λ^3 parameters. In principle, any (positive) values are possible, but it will be computationally fastest to reach entanglement dynamics when both of these ratios are set equal to one, which is what we have done in the present study, and what seems to apply fairly well for a common system like polystyrene-toluene.

Solvent viscosity, blob hydrodynamic radius $\approx b$ and temperature all coalesce to define the time unit $\tau = 6\pi\eta_s b^3/(k_B T)$, but its absolute value is not important from the algorithm point of view, just like the absolute length λ is not important, only the ratios λ/b and v/λ^3.

Next, we need to impose either the pressure or the blob density of our system. According to the semi-dilute theory, a polymer solution can be viewed as a melt of closely-packed

correlation blobs, which leads to the simulation box size

$$V = \bar{v}_0 \lambda^3 N C, \tag{26}$$

where $\bar{v}_0$ is the dimensionless volume associated with a single blob. If $\bar{v}_0$ is too small, the blobs are too crowded and the interblob potential, Equation (2), is unable to prevent chain crossings. If $\bar{v}_0$ is too big, the entanglement length grows and one needs longer chains to see the same level of chain interpenetration. We have found that a suitable compromise is $\bar{v}_0 = 2(4\pi/3)$. In terms of chains per unit volume,

$$\frac{C}{V} = \frac{1}{\bar{v}_0 \lambda^3 N} \propto \frac{\rho}{M_w}. \tag{27}$$

This chain density ensures that the osmotic pressure scales as

$$\Pi \approx \frac{k_B T}{\lambda^3} \propto \rho^{9/4} \tag{28}$$

which is the well-known des Cloiseaux law, and in our case it means that the pressure is the same regardless of chain length N. We have verified numerically that this is true for sufficiently long $N > 32$ chains. Alternatively, one could fix the pressure Π and let the box volume V fluctuate in an isobaric fashion, but we have not tried this.

Finally, there are some technical/discretisation/finite-size settings: the number of chains $C/\sqrt{N} \gg 1$, the level of chain continuity $J/N \gg b/\lambda$, and the grid size $\Delta x/\lambda \ll 1$. As for the time step, we must ensure that the excluded volume force does not overshoot its own range:

$$\Delta R = \left(\frac{v}{\lambda^3}\right)\left(\frac{k_B T}{6\pi\eta_s b}\right)\left(\frac{\Delta t}{\lambda}\right) \ll \lambda \tag{29}$$

which leads to time step limitation

$$\frac{\Delta t}{\tau} \ll \left(\frac{\lambda}{b}\right)^2 \left(\frac{\lambda^3}{v}\right). \tag{30}$$

Lastly, it is crucial that the random displacement be smaller than the repulsive one:

$$b\sqrt{\frac{\Delta t}{M\tau}} \ll \Delta R = \left(\frac{v}{\lambda^3}\right)\left(\frac{k_B T}{6\pi\eta_s b}\right)\left(\frac{\Delta t}{\lambda}\right), \tag{31}$$

which dictates the random force sampling cutoff:

$$M \gg \left[\left(\frac{\lambda^3}{v}\right)\left(\frac{\lambda}{b}\right)\right]^2 \frac{\tau}{\Delta t} \tag{32}$$

and gives the absolute shortest time scale beyond which the blob model is not applicable:

$$t_{\text{allowed}} \gg t_{\text{min}} = M\Delta t = \tau \left[\left(\frac{\lambda^3}{v} \right) \left(\frac{\lambda}{b} \right) \right]^2 . \tag{33}$$

In the limits quoted above, our numerical algorithm is expected to approach the exact analytical solution for the multi-chain problem, Equation (4). Of course, computational time becomes very long, so initially we simulate the system with a reasonable choice $\Delta x = \lambda$ and calculate some physical property such as the diffusion coefficient. Then, we repeat the simulation with $\Delta x = 0.5\lambda$ and obtain an identical result, whereas $\Delta x = 2\lambda$ produces a significantly different outcome, and so we conclude that $\Delta x = \lambda$ is the upper safety limit. This test is repeated for all the technical parameters to ensure that the physical results do not depend on their choice.

The initially chosen configuration $\mathbf{a}_n(t = 0)$ should be close to thermal equilibrium which is a priori not known. To reach the equilibrium state quickly, we use Ref.[28] method where every simulation is started with only $N = 1$ blob per chain which is just Gaussian particles in a box, a model for a solution at density $\rho = \rho^*$, or the border between dilute and semi-dilute. After a few dozen iterations, the particles have repelled each other sufficiently and we can add the second mode $N = 2$ to replace each ball with a randomly oriented Gaussian rod. After the rods have settled into their equilibrium distribution, we double the chain length again to $N = 4$ and this process continues until the desired N is obtained. The acquisition phase then starts where we record chain trajectories for analysis of various quantities and correlations of interest. We must acquire enough time steps to cover the dynamics for a time frame much longer than the system's own longest relaxation time.

VI. RESULTS

The purpose of this section is to demonstrate the feasibility and usefulness of our newly developed simulation method. A reasonably fast implementation was achieved by writing a custom MATLAB executable subroutine containing CUDA code and running on an Nvidia Quadro M4000 GPU. The computation time was about 4×10^{-7} s per time step, per chain, per Rouse mode. The source code is available upon request to the corresponding author.

We have simulated $C = 64$ chains with the number of Rouse modes spanning $N =$ 8, 16, 32, 64, 128, 256, 512, 1024, and 2048, while keeping all other parameters constant.

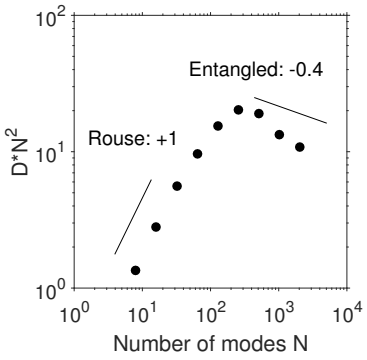

FIG. 5: Self-diffusion DN^2

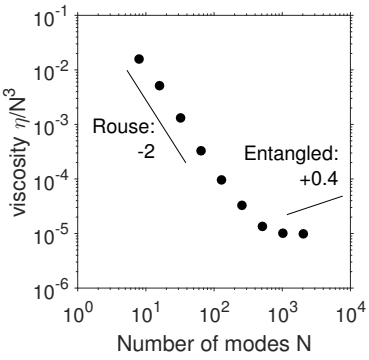

FIG. 6: Viscosity η/N^3

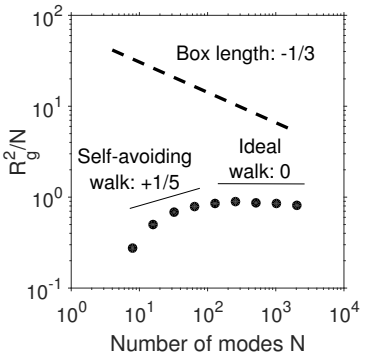

FIG. 7: Radius R_g^2/N

The primitive path analysis of an equilibrated static configuration for the $N = 1024$ chains was performed using the Z1 code[29] available online, which found $Z = 17.5$ entanglements per chain. The entanglement length is thus $N_e = N/Z = 59$, quite consistent with the departure from Rouse dynamics seen in Figures 5 and 6.

The longest run with $N = 2048$ modes lasted for about four months and was enough to reach one relaxation time as can be seen from the emerging plateaus in Figures 8b and 9b. This computational effort was sufficient to clearly reveal the departure from Rouse dynamics and into the entangled regime.

A. Mean squared displacement

Perhaps the most famous fact about entangled polymers[18] is that their motion is confined to an imaginary tube, created by the constraints imposed by all other nearby chains. The strongest topological constraint is felt by the central $j = J/2$ monomer, whereas the chain ends $j = 1$, J are more mobile and show less reptation. It is rather well established that the mean squared displacement of the central monomer

$$g_1(t) = \langle [\mathbf{R}_{J/2}(t) - \mathbf{R}_{J/2}(0)]^2 \rangle \tag{34}$$

scales as $g_1 \propto t^{1/4}$ in the range $(\tau_e \approx \tau N_e^2) < t < (\tau_R \approx \tau N^2)$, which is a signature of anisotropic diffusion along the randomly curved tube, in the presence of chain countour length fluctuations. In contrast, unentangled phantom chains would scale as $g_1 \propto t^{1/2}$ at the slowest, as described by the Rouse model with full details available in a textbook reference[30]. Therefore, we plot $g_1(t)/\sqrt{t}$ in Figure 8a, where the negative slope of $t^{-1/4}$

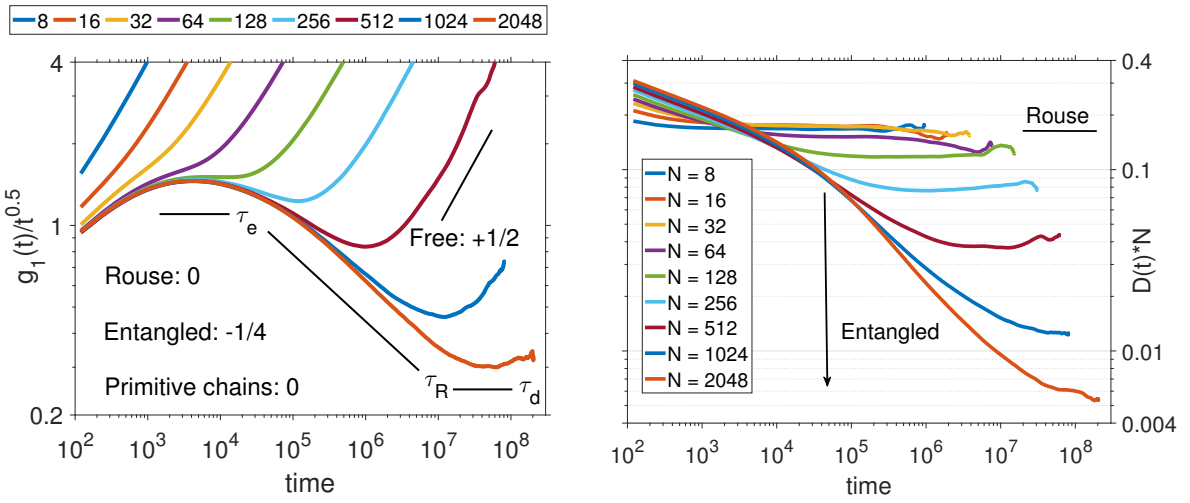

(a) Central monomer MSQD divided by $\sqrt{t}$ (b) Center of mass MSQD multiplied by $N/6t$

FIG. 8: Mean squared displacement

clearly indicates a departure from Rouse dynamics and the onset of reptation. For the very longest chains $N = 2048$ we start to see the beginnings of a new dynamical regime $(\tau_R \approx \tau N^2) < t < (\tau_d \approx \tau(N/N_e)^3)$, where the contour length fluctuations die out and pure reptation starts to dominate: $g_1 \propto t^{1/2}$ once again.

From an experimentalist point of view, it is more common to measure the mean squared displacement of the center of mass,

$$g_3 = \langle [\mathbf{a}_0(t) - \mathbf{a}_0(0)]^2 \rangle \,, \tag{35}$$

which can be used to calculate the self-diffusion coefficient

$$D = \lim_{t\to\infty} \frac{g_3(t)}{6t}. \tag{36}$$

Phantom chains would scale as $D_1 = k_B T/(6\pi\eta_s bN)$ which is the result for a group of N independent random walkers. However, entangled chains are confined to move in a tube of length $L \propto N\lambda$, and the time it takes to diffuse this far is $\tau_{\text{tube}} \propto L^2/D_1 \propto N^3$. During this time the chain center of mass has been displaced a distance of about its own radius of gyration $R_g \propto N^{1/2}\lambda$, so the actual self-diffusion coefficient is $D \propto R_g^2/\tau_{\text{tube}} \propto k_B T/(6\pi\eta_s b)N^{-2}$.

To emphasize the cross-over from Rouse to entanglement, we plot $g_3 N/6t$ in Figure 8b. In the long time $t \to \infty$ limit a plateau develops and its value gives the self-diffusion coefficient DN. On the short-time scale one expects all $g_3 N/6t$ curves to overlap, but instead we see

a slight overshoot due to the way that the random force was implemented (Equation (14)) in our equation of motion. Therefore, our data can only be considered valid after at many M-sized random steps, which is to say $t \gg (M\Delta t) = 120\tau$.

To focus on the entanglement behaviour, the result is rescaled to DN^2 and plotted in Figure 5. The shape of $D(N)$ is quite similar to the one measured in experiments[31,32] and other simulations[33], and specifically it takes about one decade worth of N to transit from $D = 1/N$ to $D = 1/N^2$ slope. We have not made a direct comparison to experiment in order to avoid a bias in the design of our own algorithm. As a side note, we mention that more elaborate theories[34] invoke contour length fluctuation in addition to pure reptation, and predict $D \propto N^{-2.4}$. This law is obeyed fairly well by our last three points $512 < N < 2048$.

B. Shear relaxation modulus

For long $N \gtrsim 100$ chains the instantaneous shear stress is dominated by the spring force contribution and is calculated[35] by

$$\sigma^{\alpha\beta} = -\frac{1}{V}\sum_{p=1}^{P} \mathbf{F}_p^{\alpha}\mathbf{R}_p^{\beta} \tag{37}$$

$$= \frac{6\pi^2 k_B T}{VNb^2}\sum_{c=1}^{C}\sum_{n=1}^{N-1} n^2 \mathbf{a}_{c,n}^{\alpha}\mathbf{a}_{c,n}^{\beta}. \tag{38}$$

Various mechanical and rheological properties can be deduced from the knowledge of the shear stress autocorrelation function, also known as the shear relaxation modulus:

$$G(t) = \frac{V}{10k_B T}\sum_{\alpha,\beta=1}^{3} \left\langle P^{\alpha\beta}(t)P^{\alpha\beta}(0)\right\rangle, \tag{39}$$

where $P^{\alpha\beta}$ is the traceless portion of the stress tensor $\sigma^{\alpha\beta}$, defined as

$$P^{\alpha\beta} = \sigma^{\alpha\beta} - \frac{1}{3}\delta^{\alpha\beta}\sum_{\gamma=1}^{3}\sigma^{\gamma\gamma}. \tag{40}$$

This formula[36] utilizes all six stress components for best possible statistics. Further, we register the stress of each chain $\sigma_c^{\alpha\beta}$ separately and only include intrachain $c = c'$ correlations[37], since the interchain contribution $\langle\sigma_c^{\alpha\beta}(t)\sigma_{c'\neq c}^{\alpha\beta}(0)\rangle$ should in theory average to zero in the long run, and therefore provides little valuable information, only useless noise.

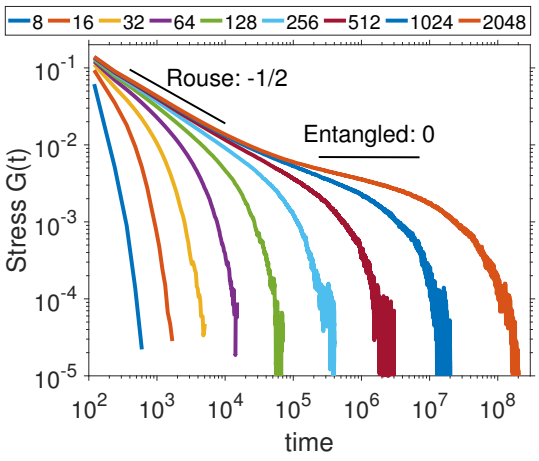

(a) Shear relaxation modulus $G(t) = \langle \sigma_{xy}(t)\sigma_{xy}(0)\rangle$ in units of k_BT/b^3

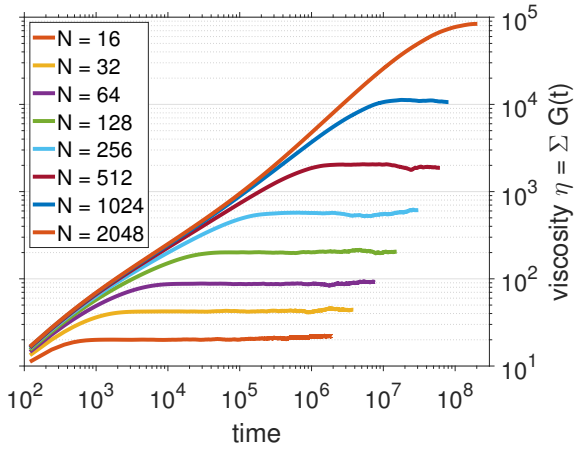

(b) Polymeric viscosity $\eta = \int G(t)\, dt$ in units of $6\pi\eta_s$

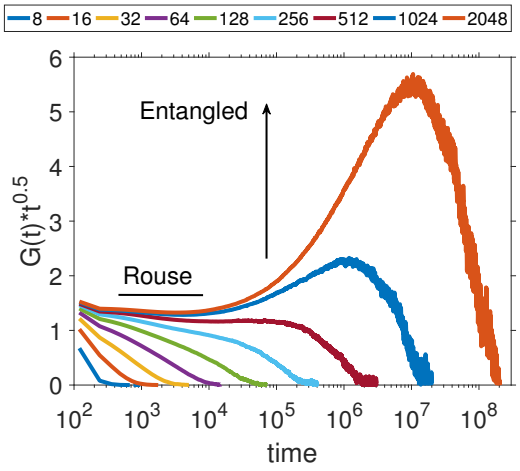

(c) Rescaled $G(t)\sqrt{t}$

FIG. 9: Analysis of shear stress fluctuations at equilibrium

The resulting $G(t)$ is plotted in Figure 9a. This can be compared to bead-and-spring simulations for melts, presented in Ref.[38]. We can see that the overall number of time steps, about 10^8, as well as the range of the $G(t)$ axis, about 10^4, is similar in both types of simulations. The main difference is that our chains are based on soft blobs, which ultimately lead to unrealistic behaviour on short time scales, but the long time scales are reasonable and can be mapped to semi-dilute solutions described by $N \propto \rho^{5/4} M_w$ blobs of unlimited size $\lambda \propto \rho^{-3/4}$. In contrast, the KG model assumes very specific FENE-WCA interactions

designed to reproduce short-time behavior in melts, which is then a strong limitation from the polymer solution point of view.

For entangled chains, either molten or semi-dilute, one expects a plateau G_0 to emerge with a value of roughly

$$G_0 = \nu k_B T, \tag{41}$$

where ν is the number of entanglements per unit volume which in our case can be estimated as $\nu = ZC/V = 0.002/b^3$. Our chains are not sufficiently long yet to see an actual flat plateau, but judging from the trend in Fig. 9a, in particular the inflection point where the $G(t)$ slope starts to be flatter than $t^{-0.5}$, a value between 0.001 and 0.005 seems quite reasonable.

Further, we can estimate the zero-shear viscosity using the Green-Kubo relationship: $\eta(t) = \int_0^t G(t')\,dt' \approx \Delta t \sum G(t')$, plotted in Figure 9b. The actual viscosity is obtained in the limit of $t \to \infty$, so in practice we must simulate long enough for the integral to flatten out, which can then be extrapolated to infinity and its value recorded in Fig. 6. A simple reptation argument predicts the viscosity $\eta \propto N^3$, but most experiments and detailed theories[39] quote the law as $\eta \propto N^{3.4}$. We therefore rescale our data to η/N^3 and find that while our longest chains are clearly not Rouse anymore ($\eta \approx N^{3.0}$), they are unfortunately not yet long enough to exhibit the experimental law. This is not surprising and is in fact corroborated by other experiments and single-chain models[40] which agree that the onset of fully entangled dynamics in terms of viscosity occurs at larger N, compared to the structural correlations such as self-diffusion (see Fig. 5). Other multi-chain bead-and-spring simulations[41] do report slopes exceeding +3, but they are extrapolated from data under shear flow. With our present model we have not yet performed such non-equilibrium simulations.

For phantom chains which can cross each other, the shear stress relaxation modulus should behave according to the Rouse model:

$$G^{\text{Rouse}}(t) \propto \frac{1}{N}\sum_{n=1}^{N} e^{-3\pi^2(t/\tau)(n/N)^2} \approx \int_0^N \frac{dn}{N}\, e^{-3\pi^2(t/\tau)(n/N)^2} \approx \sqrt{\frac{\tau}{t}}. \tag{42}$$

At large N, a power-law decay emerges: $G(t) \propto t^{-0.5}$, valid for timescales $1 \ll 3\pi^2 t/\tau \ll N^2$. In contrast, the simulated data $G(t)\sqrt{t}$, plotted in Figure 9c, shows that for chains $N = 512$ and longer, our stress relaxation is clearly slower than $t^{-0.5}$. This is a further indication that we are entering the entangled regime.

C. Radius of gyration

The focus of this paper is on the dynamics of entangled polymers, but for the sake of completeness we also present one static quantity, namely the radius of gyration:

$$R_g^2 = \int_0^1 |\mathbf{R}(s) - \mathbf{a}_0|^2 \, ds = 2 \sum_{n=1}^{\infty} |\mathbf{a}_n|^2 \tag{43}$$

$$\approx \left(2 \sum_{n=1}^{N-1} |\mathbf{a}_n|^2 \right) + R_0^2, \tag{44}$$

where one may optionally add a constant $R_0 \approx \lambda$ to compensate for all the higher Rouse modes which were truncated. We have plotted R_g^2/N in Figure 7 to show that for long chains, the scaling is $R_g \propto \sqrt{N}$, and therefore the excluded volume force is fully screened and the chains obey ideal random walk statistics.

We also show that the largest radius of gyration is roughly a factor of three smaller than the size of the box $V^{1/3}$, which should be enough to ensure that the chains do not interact with their own periodic selves.

D. Test for chain crossings

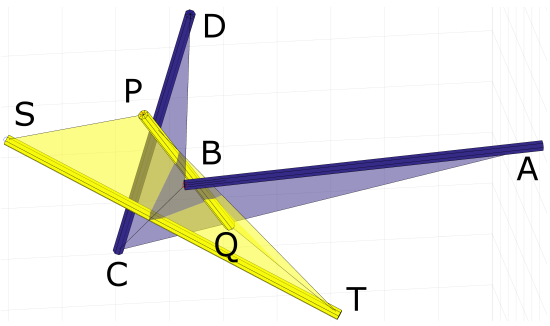

FIG. 10: Topological analysis of two moving rods detects a crossing in this particular example

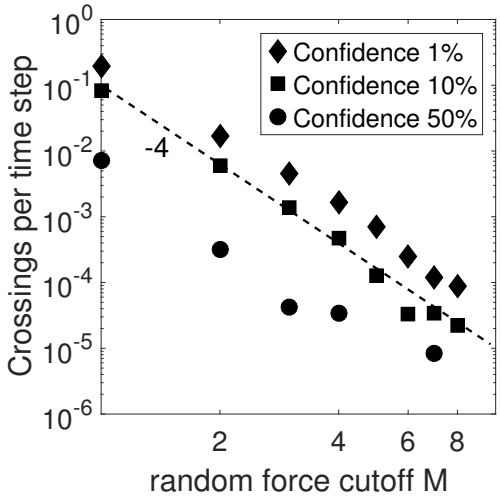

FIG. 11: Suspected crossing rate of $C = 8$ chains and $N = 16$ modes

So far we have analyzed various physical properties of our simulation and they all indicate the emergence of reptation dynamics for long chains. This implies that chain crossings are

unlikely on the scale exceeding the longest relaxation time $\tau_d \propto N^3$. To further strengthen the validity of our model, we now also present a direct calculation of chain crossing unlikelihood.

We shall analyze how the chain arrangement with respect to each other evolves from one time step to the next, and use a geometrical argument to estimate whether a crossing may have taken place. Every segment $(\mathbf{R}_j - \mathbf{R}_{j+1})(t) = \mathbf{AB}$ sweeps out a surface area, as it moves to its new position $(\mathbf{R}_j - \mathbf{R}_{j+1})(t + \Delta t) = \mathbf{CD}$. This unknown surface can be approximated by two adjoining triangles $\mathbf{ABC}$ and $\mathbf{BCD}$ (although a choice $\mathbf{ABD} \to \mathbf{ACD}$ is also possible and may produce a different result).

Before we can start the analysis, we need a mathematical criterion to determine if a fixed rod $\mathbf{PQ} = (\mathbf{P} - \mathbf{Q})$ intersects a fixed triangle $\mathbf{ABC}$. The rod $\mathbf{PQ}$ is defined by the set of all points

$$\mathbf{x}(t) = \mathbf{P} + (\mathbf{Q} - \mathbf{P})t, \quad (t > 0)\,\&\,(t < 1) \tag{45}$$

(the parameter t is not to be confused with the time variable), while the triangle $\mathbf{ABC}$ is the set of all points

$$\begin{gathered}\mathbf{y}(u, v) = \mathbf{A} + (\mathbf{B} - \mathbf{A})u + (\mathbf{C} - \mathbf{A})v, \\ (u > 0)\,\&\,(v > 0)\,\&\,(u + v) < 1\end{gathered} \tag{46}$$

To find the intersection $\mathbf{x}(t) = \mathbf{y}(u, v)$ we must solve the system of three equations

$$\mathbf{PQ}t + \mathbf{BA}u + \mathbf{CA}v = \mathbf{PA} \tag{47}$$

and find the three unknowns

$$\begin{pmatrix} t \\ u \\ v \end{pmatrix} = \frac{1}{\mathbf{PQ} \cdot (\mathbf{BA} \times \mathbf{CA})} \begin{pmatrix} \mathbf{PA} \cdot (\mathbf{BA} \times \mathbf{CA}) \\ \mathbf{PA} \cdot (\mathbf{CA} \times \mathbf{PQ}) \\ \mathbf{PA} \cdot (\mathbf{PQ} \times \mathbf{BA}) \end{pmatrix} \tag{48}$$

Since the triangle is merely an approximation for the true (unknown) surface, we assign an intersection certainty score

$$I^{(1)} = f(t)f(u)f(v)f(1 - t)f(1 - u - v) \tag{49}$$

where $f(x) = (1 + \mathrm{erf}(x/\sigma))/2$ is a fuzzy step function with a fuzziness parameter which we fixed to $\sigma = 0.05$, whereas a choice $\sigma \to 0$ would lead to an unrealistically crisp logic. A

second test $I^{(2)}$ is performed with the same rod **PQ** and the second triangle **BCD**. A score $I = 1$ means that the rod clearly intersects the triangle, $I = 0$ means that the rod is clearly outside the triangle, while some intermediate value $I \approx 0.5$ signals that the intersection is very close to the edge of the triangle and/or extremity of the rod, and the test result should be interpreted with caution.

As explained in Ref.[42], a fixed rod **PQ** crosses the path of another moving rod **AB** as it travels to **CD** if and only if one of the triangles **ABC** or **BCD** intersects the fixed rod **PQ**, and the other triangle does not. If both or neither of the triangles intersect the rod, the crossing has not taken place. Logically, this is an "exclusive or" operation, which for a fuzzy input is computed[43] as

$$I = \texttt{xor}\left(I^{(1)}, I^{(2)}\right) = I^{(1)} + I^{(2)} - 2I^{(1)}I^{(2)}. \tag{50}$$

Lastly, we take into account that both rods are in fact moving simultaneously. As suggested by Ref.[44], four tests must be done: 1) a moving rod **AB** $\rightarrow$ **CD** intersects a stationary rod **PQ**, 2) a moving rod **AB** $\rightarrow$ **CD** intersects a stationary rod **ST**, 3) a moving rod **PQ** $\rightarrow$ **ST** intersects a stationary rod **AB**, 4) a moving rod **PQ** $\rightarrow$ **ST** intersects a stationary rod **CD**. The overall certainty of an intersection having taken place is then calculated by

$$I = I_1 I_2 \bar{I}_3 \bar{I}_4 + I_1 \bar{I}_2 I_3 \bar{I}_4 + \bar{I}_1 I_2 \bar{I}_3 I_4 + \bar{I}_1 \bar{I}_2 I_3 I_4, \tag{51}$$

where $\bar{I} = \texttt{not}(I) = 1 - I$ is the logical `not` operator.

Since the topological analysis is time consuming, we have only simulated a small system with $C = 8$ chains having $N = 16$ degrees of freedom, as depicted in Figure 3. It would be interesting to quantify the amount of chain crossings as a function of chain continuity parameter J/N, but unfortunately that would be an unfair comparison. The topological testing outlined above is prone to error near segment termini, and as we increase J/N there are many more segments describing the same topology, and therefore the test becomes less valid.

However, we can compare the crossing rate as a function of the random force cutoff parameter M, plotted in Figure 11. All bond pairs were examined at each of the 10^5 time steps, and their crossing certainty score was binned into a histogram. We report the number of events exceeding the crossing score at levels of 1, 10, and 50%. This number drops very sharply with M. One may expect a Boltzmann-like exponential decay e^{-M}, but the

available data suggests that a power M^{-4} falloff is more appropriate. For larger M it is not entirely clear whether the few detected crossings are actual topological violations, or whether they can be attributed to the imperfection of the analysis method itself. We have visually inspected the configuration using a rotatable 3D plot, and could not confirm the analytically reported crossings. On the other hand, it is not impossible that some true chain crossings may have occurred during the 10^5 steps and went unreported by the topological analysis.

Either way, if we extrapolate the crossing rate with the help of the dashed line in the plot, then for a simulation with $M = 120$ cutoff the crossing rate is 10^{-9}. Scaling up to a bigger box with $C = 64$ chains, $N = 2048$ modes, we arrive at 1 crossing per 10^8 time steps, per chain. This very crude estimate shows that some occasional crossings may have occurred, and their effect would be a small bias showing less entanglement than there should be.

VII. CONCLUSION AND OUTLOOK

In this paper we have explored a pseudo-continuous model of a polymer in semi-dilute solution, consisting of long repulsive chains whose motion is resolved using large Brownian time steps. By studying structural and mechanical correlations we have verified that the chains are indeed entangled and that their dynamical properties agree fairly well with the expected scaling laws. The model presented in this work is adequate to describe semi-dilute solutions at long time and distance scales. We have only assumed a linear spring attraction on the backbone and a soft Gaussian repulsive potential between the chains.

In closing, we emphasize that the goal of our simulation is not to prevent *all* chain crossings, but only to *reduce* their rate sufficiently for entanglement dynamics to emerge. The merit of a computer simulation is judged by various facets, including most importantly a realistic description of physics, but also the execution speed, the simplicity of the code, the number of assumptions and input parameters required, as well as its elegance and beauty. While no code can be perfect in all of these regards, we have tried to strike a suitable balance and we hope that our work will find many practical applications. These could include the study of polymer solutions under shear, in confined geometries, and using different chain architectures (star, comb, ring, brush), as well as heterogeneous polymer blends.

ACKNOWLEDGMENTS

The authors thank Marcus Müller, Ralf Everaers, Giovanna Fragneto, and Felix Roosen-Runge for their useful comments on the draft version of this work. We also thank Anton Devishvili for programming help, as well as Mark Johnson and Luca Marradi for their assistance with the computational resources. Lastly, we acknowledge the use of `tubeplot` script by Janus H. Wesenberg to produce Figure 3 in MATLAB.

REFERENCES

[1]K. Kremer and G. S. Grest, The Journal of Chemical Physics **92**, 5057 (1990).

[2]J. R. Dorgan, N. A. Rorrer, and C. M. Maupin, Macromolecules **45**, 8833 (2012).

[3]J. Padding and W. Briels, Journal of Physics: Condensed Matter **23**, 233101 (2011).

[4]Y. Masubuchi, Annual Review of Chemical and Biomolecular Engineering **5**, 11 (2014), pMID: 24498953, http://dx.doi.org/10.1146/annurev-chembioeng-060713-040401.

[5]V. C. Chappa, D. C. Morse, A. Zippelius, and M. Müller, Phys. Rev. Lett. **109**, 148302 (2012).

[6]M. Langeloth, Y. Masubuchi, M. C. Böhm, and F. Müller-Plathe, The Journal of Chemical Physics **138**, 104907 (2013), http://dx.doi.org/10.1063/1.4794156.

[7]T. Uneyama and Y. Masubuchi, The Journal of Chemical Physics **137**, 154902 (2012), http://dx.doi.org/10.1063/1.4758320.

[8]A. Ramírez-Hernández, B. L. Peters, M. Andreev, J. D. Schieber, and J. J. de Pablo, The Journal of Chemical Physics **143**, 243147 (2015), http://dx.doi.org/10.1063/1.4936878.

[9]Y. Masubuchi, J.-I. Takimoto, K. Koyama, G. Ianniruberto, G. Marrucci, and F. Greco, The Journal of Chemical Physics **115**, 4387 (2001).

[10]A. Ramírez-Hernández, M. Muller, and J. J. de Pablo, Soft Matter **9**, 2030 (2013).

[11]P. Kindt and W. J. Briels, The Journal of Chemical Physics **127**, 134901 (2007), http://dx.doi.org/10.1063/1.2780151.

[12]J. T. Padding and W. J. Briels, The Journal of Chemical Physics **115**, 2846 (2001).

[13]G. Pan and C. W. Manke, International Journal of Modern Physics B **17**, 231 (2003), http://www.worldscientific.com/doi/pdf/10.1142/S0217979203017400.

[14]F. Lahmar, C. Tzoumanekas, D. N. Theodorou, and B. Rousseau, Macromolecules **42**,

7485 (2009), http://dx.doi.org/10.1021/ma9011329.

[15]M. Yamanoi, O. Pozo, and J. M. Maia, The Journal of Chemical Physics **135**, 044904 (2011), http://dx.doi.org/10.1063/1.3615504.

[16]A. Korolkovas, Physical Review E **94**, 021302 (2016).

[17]S. F. Edwards, Proceedings of the Physical Society **85**, 613 (1965).

[18]P.-G. De Gennes, *Scaling concepts in polymer physics* (Cornell university press, 1979).

[19]P. G. Bolhuis, A. A. Louis, J. P. Hansen, and E. J. Meijer, The Journal of Chemical Physics **114**, 4296 (2001).

[20]P.-G. De Gennes, Macromolecules **9**, 594 (1976), http://dx.doi.org/10.1021/ma60052a012.

[21]P. Espanol and P. Warren, EPL (Europhysics Letters) **30**, 191 (1995).

[22]P. E. Rouse Jr, The Journal of Chemical Physics **21**, 1272 (1953).

[23]S. Plimpton, Journal of computational physics **117**, 1 (1995).

[24]D. S. Cerutti, R. E. Duke, T. A. Darden, and T. P. Lybrand, Journal of chemical theory and computation **5**, 2322 (2009).

[25]S. A. Baeurle, R. Martoňák, and M. Parrinello, The Journal of chemical physics **117**, 3027 (2002).

[26]G. Zhang, K. C. Daoulas, and K. Kremer, Macromolecular Chemistry and Physics **214**, 214 (2013).

[27]J. Makhoul, Acoustics, Speech and Signal Processing, IEEE Transactions on **28**, 27 (1980).

[28]G. Subramanian, The Journal of chemical physics **133**, 164902 (2010).

[29]N. C. Karayiannis and M. Kröger, International journal of molecular sciences **10**, 5054 (2009).

[30]A. E. Likhtman, "Viscoelasticity and molecular rheology," (2012).

[31]L. Léger, H. Hervet, and F. Rondelez, Macromolecules **14**, 1732 (1981).

[32]P. Callaghan and D. Pinder, Macromolecules **14**, 1334 (1981).

[33]M. Pütz, K. Kremer, and G. S. Grest, EPL (Europhysics Letters) **49**, 735 (2000).

[34]A. L. Frischknecht and S. T. Milner, Macromolecules **33**, 5273 (2000).

[35]M. Doi and S. F. Edwards, *The theory of polymer dynamics*, Vol. 73 (oxford university press, 1988).

[36]M. Mondello and G. S. Grest, The Journal of Chemical Physics **106**, 9327 (1997).

[37]M. Vladkov and J.-L. Barrat, Macromolecular theory and simulations **15**, 252 (2006).

[38]A. E. Likhtman, S. K. Sukumaran, and J. Ramirez, Macromolecules **40**, 6748 (2007).

[39]S. Milner and T. McLeish, Physical Review Letters **81**, 725 (1998).

[40]A. E. Likhtman, Macromolecules **38**, 6128 (2005).

[41]M. Kröger and S. Hess, Physical review letters **85**, 1128 (2000).

[42]S. P. Holleran and R. G. Larson, Rheologica Acta **47**, 3 (2007).

[43]J. E. Hernandez and J. Nava, in *Fuzzy Information Processing Society (NAFIPS), 2011 Annual Meeting of the North American* (2011) pp. 1–6.

[44]F. Goujon, P. Malfreyt, and D. J. Tildesley, The Journal of chemical physics **129**, 034902 (2008).

B Simulating confined particles with a flat density profile

Author: Airidas Korolkovas

A Rapid Communication published in the *Physical Review E*, **94**, 021302(R) (2016)
(Received 13 April 2016; revised manuscript received 4 June 2016; published 15 August 2016)

Author contributions:

Airidas Korolkovas has identified the problem, found a solution, wrote the algorithm, analysed the data, and wrote the manuscript.

LR15153

Simulating confined particles with a flat density profile

Airidas Korolkovas*

Institut Laue-Langevin, 71 rue des Martyrs, 38000 Grenoble, France and

Université Grenoble Alpes, Liphy, 140 Rue de la Physique,

38402 Saint-Martin-d'Hères, France

(Dated: October 6, 2016)

Abstract

Particle simulations confined by sharp walls usually develop an oscillatory density profile. For some applications, most notably soft matter liquids, this behavior is often unrealistic and one expects a monotonic density climb instead. To reconcile simulations with experiments, we propose mirror-and-shift boundary conditions where each interface is mapped to a distant part of itself. The main result is that the particle density increases almost monotonically from zero to bulk, over a short distance of about one particle diameter. The method is applied to simulate a polymer brush in explicit solvent, grafted on a flat silicon substrate. The simulated density profile agrees favorably with neutron reflectometry measurements and self-consistent field theory results.

INTRODUCTION

Liquids at interfaces are ubiquitous: functionalized surfaces, lipid membranes, microphase separation, pores and cavities, microfluidic devices, and just about any other place where a liquid comes into contact with a solid, a gas, or another incompatible liquid. The fluid properties close to the wall are often markedly different from the bulk and it is interesting to study them using computer simulations. In particle-based models one must usually apply some confinement force at the interface and in doing so break the homogeneity of space. This invariably results in an oscillatory density profile with large deviations from the bulk level. For some systems, such as hard liquids at very crisp walls, the oscillations are realistic and match experimental data[1, 2]. In other situations, most notably coarse-grained softer fluids, the experimental density profile is usually flat[3], and so the simulated oscillations should be seen as an unwanted computational artifact. In this letter we show how to suppress such modeling bias and provide a better agreement between experiment and simulation. The main idea is to avoid border discontinuities altogether by mapping each interface back onto a distant part of itself, via mirror-and-shift boundary conditions.

MODEL SYSTEM

Our prototype system will be a liquid soft matter sample made up of large molecules with a characteristic size in the range of $\lambda \in (1;\, 100)$ nanometers. This length scale describes the dominant features for colloids, dendrimers, polymers, surfactants, etc. The liquid is placed on a flat surface, such as a silicon wafer, with roughness $\sigma \in (0.1;\, 1)\,\mathrm{nm} \ll \lambda$, much smaller than the size of the soft particles. In this scenario the chemical details of the interface are not important and cannot possibly be resolved by the coarse calculations. Therefore, the example is equally applicable to liquid/air, liquid/solid, or liquid/liquid interfaces.

A number N of particles is closely packed in a box of volume

$$V = L^3 = \frac{4\pi}{3} N \lambda^3, \tag{1}$$

and in the case of polymers this corresponds to the cross-over density between dilute and semi-dilute: $\rho = \rho^*$. It is clear from experiment[4] that the particle concentration increases monotonically from zero outside the box, to N/V inside the box, and in a simulation we

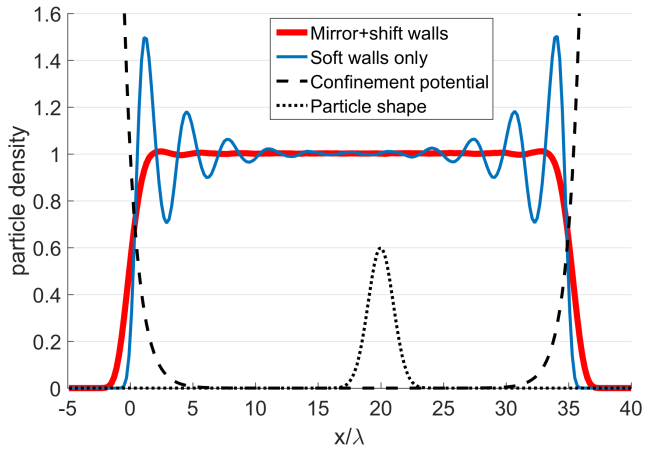

FIG. 1. Density of soft repulsive particles, closely packed between two walls is shown by the thin blue line. The oscillations can be suppressed by using mirror-and-shift boundary conditions, without compromising the sharpness of the interface, as shown by the thick red line. The dashed line shows the confinement potential $U(x)$ and the dotted line shows the particle shape $\Phi(\mathbf{r})$, on an arbitrary y-scale.

should ideally be able to resolve the climb within one particle diameter 2λ, as shown with the thick red line in Figure 1.

Surprisingly, it is quite difficult to achieve this behavior with a particle-based model, and most attempts will lead to an oscillatory density profile shown with a thin blue curve in Figure 1. As a concrete example, let the particles repel each other by a Gaussian potential

$$\Phi(\mathbf{r}) = \epsilon \exp\left(-\frac{\mathbf{r}^2}{2\lambda^2}\right), \tag{2}$$

where $\epsilon \gg k_B T$ is the repulsive strength chosen so that the particles cannot cross each other. The most common way to model a confining surface is to impose an external field $U(x)$. It will not be possible to resolve small surface features σ using particles of large size λ, and so the sharpest confinement could have its roughness equal to the particle size, $|\partial U/\partial x| \approx U/\lambda$, which leads to

$$U(x) = u\left(e^{-x/\lambda} + e^{-(L-x)/\lambda}\right) \tag{3}$$

with the confinement strength parameter u adjusted so that the density in the middle of the box equals N/V, to fulfill Equation (1). The resulting density profile is oscillating as shown with the thin blue curve in Figure 1. Similar oscillations occur with various other shapes of

the confinement $U(x)$ and the excluded volume force $\Phi(\mathbf{r})$. The oscillations do not decrease in larger $N \to \infty$ systems. They also persist for more complex fluids containing rods, chains, or polydisperse mixtures of various shapes. In general, the density oscillations are always present on the scale of the smallest particle size λ, provided that the surface roughness is on the same scale or smaller: $\sigma \lesssim \lambda$.

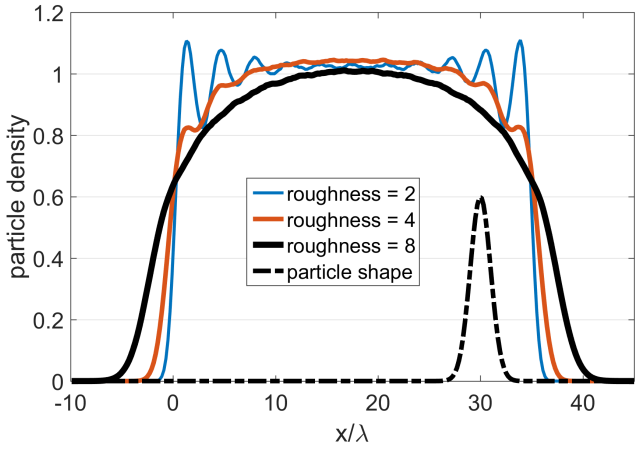

FIG. 2. Density profile dependence on surface roughness

The most obvious way to avoid the oscillations is to assume a large surface roughness $\sigma \gtrsim 6\lambda$, as demonstrated in Figure 2. Unfortunately, this assumption is not valid in many important applications, most notably soft matter at flat walls: $\lambda \gg \sigma$. This issue has been recognized in the literature before and several studies have reported alternative methods of confinement. The main idea[5–7] was to invert the density oscillations by applying a counter-oscillating confinement force. While such an approach does deliver a flat density profile, there remain several shortcomings: the confinement force has to extend many λ's deep into the bulk of the box, and the detailed shape of the force must be recalculated for every different fluid chemistry.

In this work we explore a new strategy aimed to alleviate these problems. Our main contribution is to notice that an exact counter-oscillating confinement force is already available to us, without requiring any further models or calculations. We simply map each interface back onto itself by a mirror transformation as shown in Figure 3. It is also crucial to shift the mirror images along the walls to avoid the particles interacting with themselves, as this would create unnatural correlations which behave differently from the bulk. This mapping

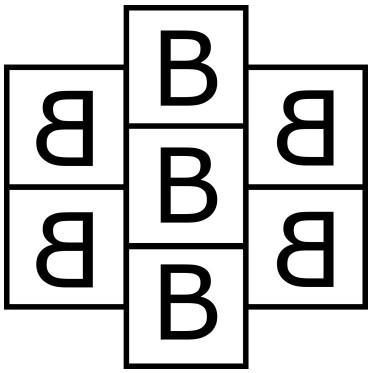

FIG. 3. Mirror-and-shift boundary condition

equalizes most of the osmotic pressure across the boundary, and the only force left to drive the particles out of the box is just random diffusion. Fortunately, the energy of a random walk is only one thermal unit $k_BT \ll \epsilon$, which is small and can be repelled back to the main box by the same external field $U(x)$ from Eq. (3), but with a weak amplitude $u \approx 1\,k_BT$. The system perceives this repulsion as a small perturbation to an otherwise perfectly balanced system, and as a result, the density oscillations are almost entirely suppressed, whereas the width of the boundary remains just a few λ's which is about as sharp as one can hope for.

METHOD

To dig straight to the root of the problem, we propose a very simple model of a fluid confined between two walls. We will work in two dimensions and so the box width is set to $L = \sqrt{4\pi\lambda^2 N}$. The position of each particle $\mathbf{R}_n$ evolves according to the Brownian equation of motion

$$\zeta \frac{\partial \mathbf{R}_n}{\partial t} = \sqrt{2\zeta k_B T}\,\mathbf{W}_n(t) - \mathbf{F}_n \tag{4}$$

where $\langle \mathbf{W}_n^\alpha(t)\mathbf{W}_m^\beta(t')\rangle = \delta^{\alpha\beta}\delta_{nm}\delta(t-t')$ is the Wiener process and

$$\mathbf{F}_n = -\nabla\left(U(\mathbf{r}) + \sum_{m=1}^{N}\Phi(\mathbf{r}-\mathbf{R}_m)\right)\Big|_{\mathbf{r}=\mathbf{R}_n} \tag{5}$$

is the confinement plus the interparticle forces. Care has been taken to resolve the equation of motion very accurately to ensure that the oscillations at the wall are an actual property of the model and not some discretisation error. Integration over a short time Δt using the

mid-point rule gives

$$\mathbf{R}_n^{(\mathtt{i})}(t+\Delta t) = \mathbf{R}_n(t) + \mathcal{R}_n\sqrt{\frac{2k_BT\Delta t}{\zeta}} + \frac{\Delta t}{\zeta}\left(\frac{\mathbf{F}_n(t)+\mathbf{F}_n^{(\mathtt{i})}(t+\Delta t)}{2}\right). \tag{6}$$

The random vector $\mathcal{R}_n$ has a fixed radius of $\sqrt{2}$ and a random orientation $\theta \in (0; 2\pi)$. Since the force at the end of the time step $\mathbf{F}_n(t+\Delta t)$ is not known, we initially guess $\mathbf{F}_n^{(\mathtt{1})}(t+\Delta t) = \mathbf{F}_n(t)$, and then evaluate all the forces again using the $\mathbf{R}_n^{(\mathtt{1})}$ configuration to obtain a better guess $\mathbf{F}_n^{(\mathtt{2})}(t+\Delta t)$. This process is repeated until the residual $\mathtt{max}|\mathbf{R}_n^{(\mathtt{i})} - \mathbf{R}_n^{(\mathtt{i-1})}| < 0.01\lambda$ is only a tiny fraction of the particle size. The dimensionless time step $\lambda^2\Delta t/\zeta \approx 1/\epsilon$ is chosen so that the above convergence criterion is met in $\mathtt{i} \approx 3$ iterations on average.

The first run was simulated on a system with $N = 100$ particles, $\epsilon = 100k_BT$ interparticle barrier and $u = 6.5k_BT$ confinement strength. Periodic boundary condition was applied on the y-axis:

$$y_{nm} \to y_{nm} - L\,\mathtt{round}\,(y_{nm}/L)\,, \tag{7}$$

and no such condition on the confined x-axis. The resulting long-time average density profile is shown with a blue oscillating line in Figure 1.

In the second run we have simulated the same system but included additional interparticle pairs. For every particle $\mathbf{R}_m$ we construct its mirror-and-shifted counterparts on the left and right sides of the box:

$$\mathbf{R}_m^{(\mathrm{L})} = \begin{pmatrix} -x_m \\ y_m + L/2 \end{pmatrix} \quad \text{and} \quad \mathbf{R}_m^{(\mathrm{R})} = \begin{pmatrix} 2L - x_m \\ y_m + L/2 \end{pmatrix} \tag{8}$$

and then every original particle $\mathbf{R}_n$ feels three sets of interactions: $\mathbf{R}_{nm}^{(L,0,R)} = \mathbf{R}_n - \mathbf{R}_m^{(L,0,R)}$. The usual periodic boundary condition on the y-axis is afterward applied to all the pairs, using Eq. (7). In short, every particle $\mathbf{R}_n$ interacts with all the other particles $\mathbf{R}_m$ as well as their both mirror-shifted images as defined above. Of course, in practice only sufficiently nearby pairs $\mathbf{R}_{nm} \lesssim 6\lambda$ have to be considered, and our number of such pairs is exactly the same as in a standard bulk simulation with periodic boundary conditions. Therefore, the computational cost is similar to the bulk case[8] of a comparable size.

An external field from Equation (3) is still required to confine random diffusion, but now a much weaker barrier $u = 1\,k_BT$ was sufficient to keep the density in the center of the box at the nominal level N/V as designated by Eq. (1). The density profile thus obtained is

shown by the thick red line in Figure 1. Admittedly, there still remains a slight, about 1% high, overshoot after the boundary, but it is a considerable reduction from 50% overshoot which is obtained without the use of mirrors.

APPLICATION: POLYMER BRUSH

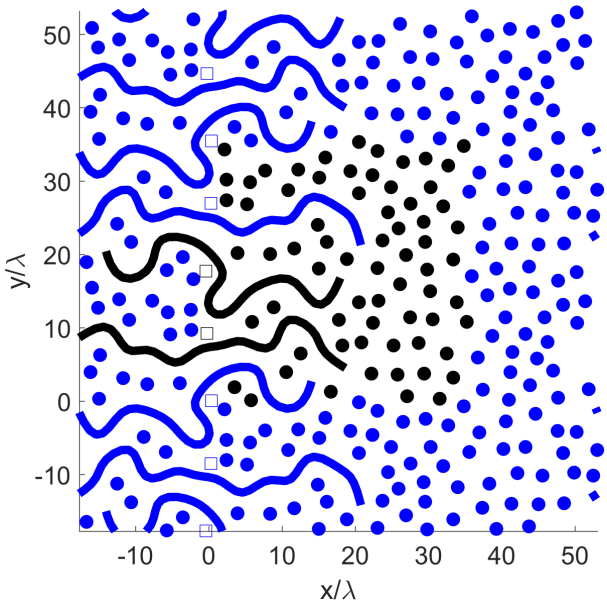

FIG. 4. Polymer brush in a good solvent. The main box is the black region $\mathbf{r} \in (0; 35.4)^2$. Grafting points are shown by hollow squares.

To demonstrate the usefulness of our new method, we present one real-world application whose simulation necessitates confinement. We will study a polymer brush grafted on a flat silicon wafer and immersed in a good solvent, as shown in Figure 4. It is essentially the same simulation as in the previous section, with the solvent molecules now coarse-grained into blobs of size λ, and $N = 16$ of the blobs are connected into a chain by linear springs of length $b = \lambda$. We have added $C = 2$ of such chains on the $x = 0$ interface, corresponding to a grafting density $\sigma = 2C\lambda/L = 0.11$. The chains are overlapping and are in the stretched brush regime.[9]

To suppress the likelihood of the chains crossing each other, the polymer is described by

a continuous curve with N degrees of freedom:

$$\mathbf{R}(s) = \mathbf{a}_0 + 2\sum_{n=1}^{N-1} \mathbf{a}_n \cos(\pi s n), \quad s \in (0;\, 1) \tag{9}$$

which is sampled at discrete points $j = 1,\, 2,\, \ldots,\, J \geq N$,

$$\mathbf{R}_j = \mathbf{a}_0 + 2\sum_{n=1}^{N-1} \mathbf{a}_n \cos\left[\pi\left(\frac{2j-1}{2J}\right) n\right], \tag{10}$$

and we have used $J = 3N+1 = 49$, but the precise choice is not important as long as $J \gg N$. The motion of every j-particle follows the same Equation (4) as the solvent particles, with a few minor alterations. First, the intermolecular potential stemming from a $j = (Js_0 + 1/2)$ particle is

$$\Phi_j(\mathbf{r} - \mathbf{R}_j) = \int_{s_0-1/(2J)}^{s_0+1/(2J)} ds\, N\Phi(\mathbf{r} - \mathbf{R}(s)) \tag{11}$$

$$\approx \left(\frac{N}{J}\right)\Phi(\mathbf{r} - \mathbf{R}_j) \tag{12}$$

reduced by N/J. The friction coefficient is also decreased: $\zeta_j = (N/J)\zeta$, but so is the coupling to the potential field: $\mathbf{F}_j = -(N/J)\nabla(U + \sum \Phi)$. A linear spring force

$$\mathbf{F}_{\text{spring}} = \left(\frac{3k_BT}{Nb^2}\right)\frac{\partial^2 \mathbf{R}}{\partial s^2} \tag{13}$$

is included by first going to the Rouse representation

$$\mathbf{a}_n = \int_0^1 ds\, \mathbf{R}(s)\cos(\pi s n) \tag{14}$$

$$\approx \frac{1}{J}\sum_{j=1}^{J} \mathbf{R}_j \cos\left[\pi\left(\frac{2j-1}{2J}\right) n\right], \tag{15}$$

and then applying the Backwards Euler scheme:

$$\mathbf{a}_n \to \frac{\mathbf{a}_n}{1 + 3\pi^2\left(\frac{k_BT\Delta t}{\zeta b^2}\right)\left(\frac{n}{N}\right)^2}. \tag{16}$$

At this point, the configuration in real space $\mathbf{R}_j$ is recovered by Eq. (10), and the next iteration can begin.

The chains are uniformly grafted at $x = 0$ plane, where "uniformly" means at equidistant points, plus a random number of variance λ in all directions. The grafting model should at the very least: 1) keep the interface as homogeneous as possible, to avoid density oscillations,

and 2) ensure that the solvent particles do not sneak in between the grafted chain and the wall. One way to satisfy these requirements is to anchor the central point $s_0 = 1/2 \to j_0 = (J+1)/2$ to its designated grafting location using a soft attractive potential

$$U_{\text{graft}}(\mathbf{r}) = -k_B T \cosh(\mathbf{r}/\lambda). \tag{17}$$

Next, the first half of the chain $s < 1/2$ is assigned to the main box, and feels the wall $U(x)$ from Eq. (3), just like all the solvent particles. The second half of the chain $s > 1/2$ is assigned to the mirror box where it feels the reflected wall $U(-x)$. A snapshot of the resulting conformation is plotted in Figure 4, showing that each chain plays a tug of war between the main box and its shifted mirror, contributing two bristles of length $N/2$ to the brush.

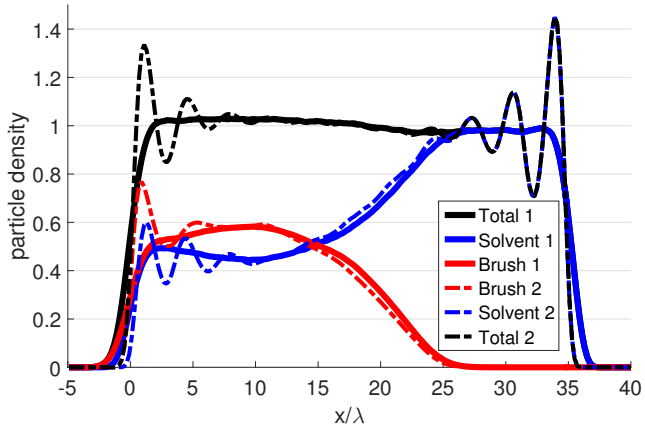

FIG. 5. Brush density profile. Solid lines result from mirror-and-shift walls, whereas dashed oscillating lines originate from external confinement alone.

The density profile of the brush and the solvent is shown in Figure 5. Notice that the polymer is slightly denser than the chemically identical solvent, which is to be expected because of the spring attraction. Our result is quite similar to the self-consistent field theory calculations[10] as well as experimental data of PDMS[11] and polystyrene[12] brushes swollen in toluene and measured using neutron reflectometry. Most importantly, the experiments decidedly exclude density oscillations of 50% which would be present in a simulation without mirror walls (dashed lines), and as seen in other simulation studies[13].

CONCLUSION

In general, particles under confinement will develop density oscillations if the surface roughness σ is not substantially greater than the smallest particle size λ. This has been a common problem for coarse-grained simulations where the confining surface can be atomically crisp, while the liquid "particles" are large clusters of many atoms, grouped together for computational convenience. In most experiments the density profile is monotonic, whereas the majority of simulations report an oscillating density.

In this study we have succeeded to suppress the oscillations considerably by mirroring the interface back onto a distant part of itself, so that the system self-equilibrates and remains quasi-homogeneous at the boundary. The only imperfection is that we must still add a weak external confinement to counteract thermal diffusion, but this is a small perturbation and the remaining density oscillations are tiny.

The mirror-and-shift boundary conditions do not require any input parameters and are scale-independent. Therefore, they could in principle be applied to any other situation, as a replacement of the usual periodic boundary conditions. One could also use the method to just alter the topological connectivity of the simulation box, without adding the confining field.

ACKNOWLEDGMENTS

The author thanks Jean-Louis Barrat and Philipp Gutfreund for critical comments during the preparation of this manuscript.

---

* korolkovas@ill.fr

[1] L. Cheng, P. Fenter, K. Nagy, M. Schlegel, and N. Sturchio, Physical Review Letters **87**, 156103 (2001).

[2] H. Mo, G. Evmenenko, and P. Dutta, Chemical physics letters **415**, 106 (2005).

[3] M. Maccarini, Biointerphases **2**, MR1 (2007).

[4] R. K. Thomas and J. Penfold, Current Opinion in Colloid & Interface Science **1**, 23 (1996).

[5] I. V. Pivkin and G. E. Karniadakis, Physical review letters **96**, 206001 (2006).

[6] E. Kotsalis, J. H. Walther, and P. Koumoutsakos, Physical Review E **76**, 016709 (2007).

[7] K. Issa and P. Poesio, Physical Review E **89**, 043307 (2014).

[8] S. Plimpton, Journal of computational physics **117**, 1 (1995).

[9] P. de Gennes, Macromolecules **13**, 1069 (1980).

[10] E. Zhulina, O. Borisov, and L. Brombacher, Macromolecules **24**, 4679 (1991).

[11] C. Marzolin, P. Auroy, M. Deruelle, J. Folkers, L. Léger, and A. Menelle, Macromolecules **34**, 8694 (2001).

[12] C. Devaux, F. Cousin, E. Beyou, and J.-P. Chapel, Macromolecules **38**, 4296 (2005).

[13] T. Kreer, Soft Matter (2016).

C Polymer brush collapse under shear flow

Authors: Airidas Korolkovas, César Rodriguez-Emmenegger, Andres de los Santos Pereira, Alexis Chennevière, Fréderic Restagno, Maximilian Wolff, Franz Adlmann, Andrew J.C. Dennison, and Philipp Gutfreund

(submitted to *Macromolecules*)

Author contributions:

The experiment was designed by M.W., P.G., A.K., and F.R.

Rheo-NR data was collected and analysed by P.G. and A.K. with participation of M.W., A.C., and F.A.

The "grafting-to" brush was made by A.C. and F.R.

The "grafting-from" brush was made by A.S.P. and C.R.E. with participation of A.K.

Simulations and theory were performed by A.K.

The manuscript was written by A.K. with the contribution of all authors.

Polymer brush collapse under shear flow

Airidas Korolkovas,[*,†,‡] Cesar Rodriguez-Emmenegger,[¶] Andres de los Santos Pereira,[§] Alexis Chennevière,[‖] Frédéric Restagno,[⊥] Maximilian Wolff,[#] Franz Adlmann,[#] Andrew J.C. Dennison,[@,†,△] and Philipp Gutfreund[*,†]

†*Institut Laue-Langevin, 71 rue des Martyrs, 38000 Grenoble, France*

‡*Université Grenoble Alpes, Liphy, 140 Rue de la Physique, 38402 Saint-Martin-d'Hères, France*

¶*DWI - Leibniz Institute for Interactive Materials and Institute of Technical and Macromolecular Chemistry, RWTH Aachen University, Forckenbeckstraße 50, 52074 Aachen, Germany*

§*Institute of Macromolecular Chemistry, Academy of Sciences of the Czech Republic v.v.i., Heyrovsky Sq. 2, 162 06 Prague, Czech Republic*

‖*Laboratoire Léon Brillouin, CEA, CNRS, Université Paris-Saclay, Saclay 91191 Gif-sur-Yvette Cedex, France.*

⊥*Laboratoire de Physique des Solides, CNRS, Univ. Paris-Sud, Université Paris-Saclay, 91405 Orsay Cedex, France*

#*Division for Material Physics, Department for Physics and Astronomy, Uppsala University, Box 516, 75120 Uppsala, Sweden*

@*Department of Chemistry, Technical University Berlin, 10623 Berlin, Germany*

△*Department of Physics and Astronomy, University of Sheffield, S102TN Sheffield, UK*

E-mail: korolkovas@ill.fr; gutfreund@ill.fr

January 11, 2017

Abstract

Shear responsive surfaces offer potential advances in a number of applications. Surface functionalisation using polymer brushes is one route to such properties, particularly in the case of entangled polymers. We report on neutron reflectometry measurements of polymer brushes in entangled polymer solutions performed under controlled shear, as well as coarse-grained computer simulations corresponding to these interfaces. Here we show a reversible and reproducible collapse of the brushes, increasing with the shear rate. Using two brushes of greatly different chain lengths and grafting densities, we demonstrate that the dynamics responsible for the structural change of the brush are governed by the free chains in solution rather than the brush itself, within the range of parameters examined. The phenomenon of the brush collapse could find applications in the tailoring of nanosensors, and as a way to dynamically control surface friction and adhesion.

Introduction

A polymer brush is a unique type of surface functionalisation, consisting of long polymer chains densely tethered by one end to a surface.[1,2] The conformation of a solvated polymer brush is markedly different to that of chains in bulk polymer solution as the brush must stretch away from the surface to minimize contact with the densely grafted neighbouring chains. Polymer brushes have broad interest across a variety of sectors since tuning interfacial properties (e.g. chemical composition, molecular weight, grafting density) can yield surface coatings with a high degree of control and in some cases completely new functionality.

One of the most common uses for brushes is to inhibit protein adsorption and prevent surface fouling.[3,4] Various other applications are also under investigation[5] ranging from bioactive interfaces,[6] to brush-mediated lubrication,[7,8] to soil release in textiles,[9] and even semiconductor manufacturing.[10,11] Another emerging application is the use of polymer brushes as nanosensors reacting to various stimuli including pressure,[12] light,[13] temperature,[14] and

pH,[15] among others. Remarkably, the sensitivity of these nanoscale sensors can be finely tuned by the amount of the brush swelling,[16] which in turn depends on the nature of the solvent, but can also be affected by other factors such as shear stress as will be shown in this article.

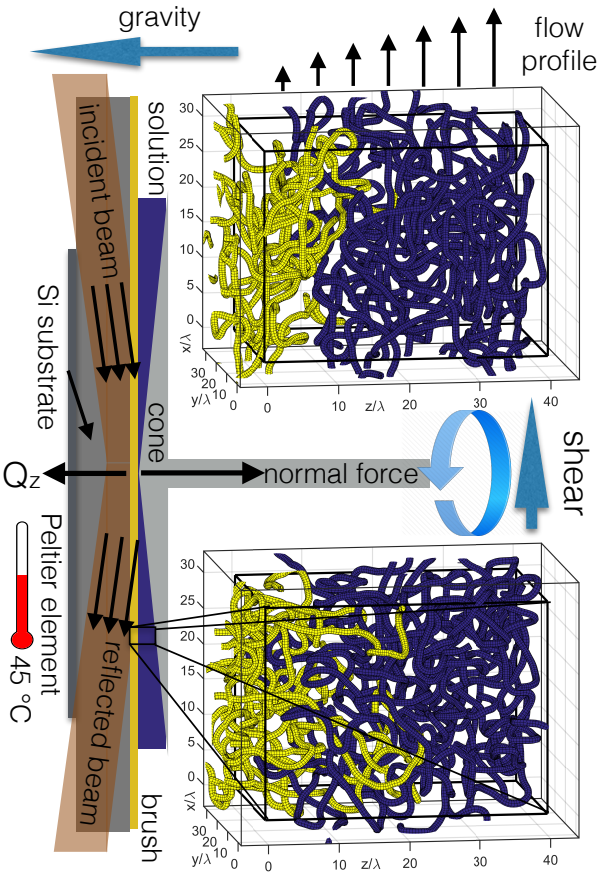

Figure 1: Experimental setup and simulated polymer conformation. The experiments are conducted with the silicon-polymer interface horizontally oriented. The wavevector transfer Q_z is perpendicular to the interface. The temperature of the silicon substrate is controlled by a Peltier element from the bottom side. Shear is applied by the rheometer *via* a titanium cone or plate. The lower right panel shows a conformation snapshot plotted from the simulation data. The interpenetration of the polymer brush (yellow) and free chains (blue) is clearly visible. With applied shear (upper right panel) the free chains are pulled out of the brush, the mean thickness of the brush decreases and the interface becomes sharper. The density profiles along the z-direction are compared to the neutron reflectometry data.

The static properties of polymer brushes are well understood thanks to extensive theoretical,[17] computer simulation,[18,19] and experimental[20–23] studies. The knowledge of brush

dynamics, however, is still incomplete, even though it is crucial for the design of the aforementioned sensors. To help fill this demand, our study will focus on the response of brushes to an applied shear stress while swollen and deeply interpenetrated with a bulk polymer solution, illustrated in Fig 1. Aside from use in sensors, surfaces decorated with brushes may also play a key role to control adhesion,[24,25] lubrication,[26] friction,[27,28] and in microfluidic devices[29] and confined channels.[30] In our experimental conditions, the chains are strongly entangled reaching a relaxation time on the order of $\tau_d = 1\,\mathrm{s}$, which has immediate practical importance since it can dynamically interact with the flows encountered in the aforementioned real world applications, which commonly have similar time scales. However, the brush-bulk interface remains very challenging to investigate either theoretically[31] or experimentally, due to its complex, heterogeneous, strongly interacting, non-equilibrium, and confined nature. We have therefore taken a two pronged approach and used a recently developed computer simulation technique[32] as well as state-of-the-art experimental rheology - neutron reflectometry (rheo-NR)[33] capabilities. This combination enables greater insight into what is occurring at the interface compared to the two approaches taken separately.

Simulation of polymer brushes under shear[34,35] is a vibrant field: brushes in good solvent,[36,37] two opposing polyzwitterionic brushes,[38] brushes in contact with short melt chains,[39] and stiff brushes related to biological membranes,[40] just to name a few recent publications. However, most of the simulations (molecular dynamics, dissipative particle dynamics, and various kinds of Monte Carlo) are based on $\lambda \approx 1\,\mathrm{nm}$ size beads running at time steps of about $\tau_m = 10^{-12}\,\mathrm{s}$, required to follow the thermal fluctuations of the bead momentum. Current computers can typically perform 10^8 time steps within a reasonable execution time; insufficient to bridge the gap to our experimental goal of $\tau_d = 1\,\mathrm{s}$.

The next level of coarse-graining is the Brownian dynamics where we abandon the bead momentum altogether and only track their positions, which take about $\tau = 10^{-9}\,\mathrm{s}$ to relax after diffusing a distance greater than their own size. This technique has already been used to predict a brush collapse under shear.[41] However, the reported collapse occurred at a shear

rate approaching $\dot{\gamma} \approx 1/\tau \approx 10^9\,\mathrm{s}^{-1}$ and was due to the finite extensibility of the polymer backbone. Such extreme shear rates are more akin to an explosion than a well controlled shear experiment and this mode of brush collapse is not related to the entanglement dynamics at $\dot{\gamma} \approx 1/\tau_d \approx 1\,\mathrm{s}^{-1}$ relevant to realistic flow conditions measured in our study.

Our experiments are done using polystyrene (PS) in a good solvent at $\phi = 30\,\%$ fraction by weight. To describe this liquid, the appropriate coarse particle is called a blob[42] and its size corresponds to the typical distance between neighbouring polymer chains: $\lambda = a\phi^{-3/4}$, where $a \approx 7\,\text{Å}$ is the size of one styrene monomer. The blob repulsion is best quantified by an effective Gaussian potential which results in the correct static structure.[43] Dynamically, however, this blob potential was considered too weak and too soft to prevent chain crossings[44] and therefore unable to produce any entanglements. A recent study,[32] however, has proposed to smear out the Gaussian potential in both time and space, thus suppressing chain crossings while retaining the long Brownian time step τ adequate to describe our experiments.

Neutron Reflectometry (NR) is a powerful experimental tool for the structural and dynamical investigation of polymer brushes, thanks to the possibility of isotopic replacement to enhance the contrast between the grafted and the bulk polymers, as well as its atomic resolution and non-invasive nature. A unique advantage of NR is that most engineering materials like aluminium or silicon are transparent for the neutrons which permits direct measurement of the brush-bulk interface through the silicon substrate.[33] Structural investigations of brushes under shear load have been performed by NR measurements on PS brushes in solvents,[45,46] but found no measurable effect. Next, we look at two studies which examined a PS brush in contact with a PS melt. The first one was measured *in situ* while shearing.[47] No reproducible result could be obtained and it was explained by metastable states of the brush. However, very high torques were applied in that study and the brushes were not characterised after the shear experiments. It has been shown by NR that PS brushes can be destroyed by high torque shear[48] and such a scenario is likely in the aforementioned experiment. The second study also sheared PS brushes in a PS melt,[49] which were then rapidly

quenched below their glass transition temperature and measured *ex situ* with NR, reporting a reproducible retraction of the brush. In our present study we have used NR for an *in situ* characterisation of the behaviour of PS brushes under shear by an entangled PS solution in diethyl phthalate (DEP, a good solvent of very low volatility). The use of solution rather than melt is more relevant to biological processes as well as microfluidic applications.

Here we show both experimentally and computationally that the entangled polymer brush thickness decreases with shear. More precisely, we observe a shrinking of brushes proportional to the square of the applied shear rate. This non-linear effect is attributed to the normal stress difference, which is an excess pressure buildup perpendicular to the applied shear flow, and is well-known to occur in bulk entangled polymer fluids, where it leads to the so-called Weissenberg effect.[50] The time scale of the brush collapse is determined by the reptation time of the free chains in solution, rather than the internal dynamics of the brush. The brush thickness returns to equilibrium upon cessation of shear, and the effect can by cycled many times over. The experimental and simulation findings are in good agreement and are further corroborated by a simple phenomenological theory.

Experimental

Materials

N,N,N',N",N"-Pentamethyldiethylenetriamine (PMDETA, 99 %), styrene (99 %), diethoxy(3-glycidyloxypropyl)methysilane (99 %), dichloromethane (99 %) and diethyl phthalate (DEP) (99 %) were purchased from Sigma-Aldrich (Czech Republic). Deuterated polystyrene (dPS), $M_w = 627\,\mathrm{kg\,mol^{-1}}$, $M_w/M_n = 1.09$, correspopnding to $P = M_w/112.2\,\mathrm{g\,mol^{-1}} = 5570$, was purchased from Polymer Source, Canada. Monocrystalline silicon blocks of size $7 \times 7 \times 1$ cm, orientation (1, 0, 0), were purchased from CrysTec, Germany. Styrene was distilled over CaH_2 under reduced pressure and stored under Ar.

[11-(2-Bromo-2-methyl)propionyloxy]undecyltrichlorosilane was synthesized according to a

previously published protocol.[51]

Preparation of Brush-long-sparse: "grafting-to" approach

The amino end-functionalized PS was synthesized in-house to a molecular weight of M_n = 218 kg/mol ($N = M_n/104.15\,\mathrm{g\,mol^{-1}} = 2093$) and a polydispersity of 1.23. Then it was grafted onto a self-assembled monolayer (SAM) of diethoxy(3-glycidyloxypropyl)methysilane) deposited on a single crystal silicon block. Details about the sample preparation can be found in Ref.[52] The thickness of the SAMs was determined by ellipsometry and found to be 1.0 nm for both brushes corresponding to fully stretched and upright standing chains in accord with previous samples.[52] The silicon oxide thickness was determined by NR as described in the SI.

Preparation of Brush-short-dense: "grafting-from" approach

PS brushes were grafted from an initiator-coated substrate by surface-initiated atom transfer radical polymerization (ATRP) employing a literature procedure,[53] modified to achieve a lower grafting density and high thickness. Firstly, a self-assembled monolayer of ATRP initiator was immobilized on the surface. The substrate (silicon slab) was rinsed with toluene, acetone, ethanol, and deionized water, blown dry with nitrogen, and activated in a UV/O_3 cleaner for 20 min. Without delay, the sample was placed in a custom-made reactor vessel, which was then sealed, evacuated, and refilled with Ar. A 1 µg mL^{-1} solution of (11-(2-bromo-2-methyl)propionyloxy)undecyltrichlorosilane in anhydrous toluene was added until the sample was fully immersed. The immobilization of the initiator was allowed to proceed for 3 h at room temperature and the sample was subsequently removed from the reactor, rinsed copiously with toluene, acetone, ethanol, and deionized water, and dried by blowing with nitrogen.

To achieve a lowered grafting density, a fraction of the surface-grafted ATRP initiator groups were deactivated by nucleophilic substitution with NaN_3. The sample was placed in

a custom-made reactor, which was then sealed, evacuated, and refilled with Ar, and placed in a thermostatic bath at 60 °C for 1 h to reach thermal equilibrium. A solution of NaN_3 (3.4 mg mL^{-1}) in anhydrous *N,N*-dimethylformamide (DMF), previously heated to 60 °C, was added to completely cover the sample and the reaction was allowed to proceed at 60 °C for 8 h. Subsequently, the reaction was stopped by replacing the solution in the reactor with pure DMF. The sample was removed from the reactor, rinsed copiously with DMF, ethanol, and deionized water, and dried by carefully blowing with nitrogen.

For the surface-initiated ATRP, styrene (40 mL, 349 mmol), anhydrous toluene (20 mL), and PMDETA (760 µL, 3.64 mmol) were degassed in Schlenk flask via three freeze-pump-thaw cycles. The solution was transferred under Ar to another Schlenk flask containing CuBr (496 mg, 3.46 mmol) and $CuBr_2$ (40 mg, 0.179 mmol), which had been previously deoxygenated by three vacuum/Ar-backfilling cycles. The flask containing the polymerization solution was placed in thermostatic bath at 90 °C and stirred vigorously for 1 h. The initiator-functionalized substrate was placed vertically in a custom-made reactor, which was subsequently closed, deoxygenated by three cycles of vacuum/Ar-backfilling, and placed in a thermostatic oil bath at 90 °C to allow the temperature to equilibrate. The polymerization solution was transferred under Ar to the reactor containing the substrate and the reaction was allowed to proceed at 90 °C for 22 h. The reaction was stopped by opening the reactor and adding toluene and the substrate was rinsed copiously with toluene, acetone, ethanol, and deionized water and dried by blowing with nitrogen. The dry thickness of the layers was measured by spectroscopic ellipsometry and NR.

Rheology

Deuterated polystyrene (dPS, 0.3 g) was mixed at 30 % weight fraction with diethyl phthalate (DEP, 0.7 g, a good solvent of low volatility), in a round bottom flask. It was topped with an abundant amount (50 mL) of dichloromethane (also a good solvent, but high volatility), and stirred for several hours to fully dissolve the dPS. The dichloromethane was then slowly

removed in a rotary evaporator under reduced pressure, which ensured that no gas bubbles were left trapped in the resulting viscous liquid.

A teflon spatula was used to transfer the dPS-DEP solution onto the brush-coated silicon crystal. The liquid was then contained in an Anton-Paar MCR 501 rheometer in cone-plate or plate-plate geometry (1° cone angle, 50 mm diameter for cone or plate) to allow *in situ* rheology as explained in Ref.[33] The rotating cone or plate on top was made of titanium and its surface was sand-blasted to reduce surface slip at the moving interface. The temperature on the stationary brush-coated side was kept constant at 45 °C throughout the experiment.

Neutron experiment details

Neutron reflectometry was carried out on FIGARO at the Institut Laue-Langevin, Grenoble, France.[54] The measurements were performed in time-of-flight mode using a wavelength band from 2.2 - 21 Å and a wavelength resolution of 7 %. Two reflection angles (0.62° and 2.72°) were used to cover the full Q-range by rotating the incident beam and the detector around the sample keeping the rheometer horizontal at all times. The relative angular divergence was set to $\Delta\theta/\theta = 1.5\,\%$ for both reflection angles. The acquisition time was 1 - 5 min for the first reflection angle and 25 min for the second angle and all measurements under shear were reproduced and cycled several times to exclude any transient phenomena. The footprint of the neutron beam (39×35 mm^2) was centered to the cone/plate, hence the scattering momentum transfer is parallel to the shear gradient. The rheo-NR setup with the neutrons entering through the side of the stationary silicon substrate (see Fig. 1) is explained in more detail in Ref.[33]

Simulation method

Each chain is described by a continuous path $\mathbf{R}(s)$ where $s \in (0, 1)$ is the monomer label. The chains have N degrees of freedom and repel one another via a Gaussian potential

$\Phi(\mathbf{r}) = k_B T e^{-\mathbf{r}^2/(2\lambda^2)}$, while the backbone stays connected via a harmonic spring interaction of the same strength $k_B T$ and the same length λ. The continuous backbone s is sampled by a number of $J = 4N$ discrete points:

$$\mathbf{R}_j = \mathbf{a}_0 + 2\sum_{n=1}^{N-1} \mathbf{a}_n \cos\left(\frac{\pi(2j-1)n}{2J}\right) \tag{1}$$

which ensures that neighbouring points $|\mathbf{R}_j - \mathbf{R}_{j+1}| \ll \lambda$ are closer together than the potential range of the blob λ, and hence there are effectively no gaps through which the chains could cross. The propagation in time is carried out in terms of N Rouse modes:

$$\mathbf{a}_n(t+\Delta t) = \mathbf{a}_n(t) + (\mathbf{F}_{\text{spring}} + \mathbf{F}_{\text{exvol}})\Delta t + \lambda\sqrt{6\Delta t/(\tau M)}\,\mathcal{R}_n, \tag{2}$$

where standard formulas are used to evaluate the spring and the excluded volume forces. The Brownian time unit can be estimated by the Einstein-Stokes formula:

$$\tau = \frac{6\pi\eta_s\lambda^3}{k_B T} \approx 10^{-9}\,\text{s}, \tag{3}$$

where $\eta_s = 1.7 \times 10^{-2}\,\text{Pa}\,\text{s}$ is the viscosity of DEP.

The important novelty in this simulation is that its time resolution is deliberately truncated by updating the random vector $\mathcal{R}_n$ only at intervals of $M = 120$ steps instead of every single $M = 1$ step. This ensures that the random force strength is much weaker than the excluded volume one (by a factor of $\sqrt{M}$), thereby suppressing any chances of chain crossings and giving rise to entanglement dynamics.

Here we note that the maximum applicable shear rate is also limited to about $\dot{\gamma}(M\tau) \ll 1$, and the fastest one we have used was $\text{Wi} = \dot{\gamma}\tau_d = 50$. This leaves us with a safety margin of $1/(M\dot{\gamma}\tau) = 17$, so we do not expect too many chain crossings. Either way, this shear rate is already an order of magnitude faster than the experimental one, leaving us plenty of room for comparison with the experimental data.

In the simulation we did not reconstruct a one-to-one correspondence with either of the experimental brushes. Instead, the simulated brush density was deliberately chosen to be smaller than the experimental one, because of two reasons. First, the experimental samples, especially the Brush-short-dense, are mostly composed of the "dry" interior region, which would consume a lot of computing time to simulate, without resulting in any interesting effects under shear. Second, a dry and strongly stretched brush cannot be described using the same blob potential as the bulk chains. Instead, smaller blobs must be used[55] to ensure incompressibility which requires the total polymer density to be constant across the whole box (see Fig. 4a). Also, the brush blob size would have to shrink further as the brush collapses under shear. This introduces another complication into an already difficult system, whereas we prefer to present the absolutely simplest possible model.

Confinement

To confine the system between two walls, we have used the recently developed mirror-and-shift boundary conditions.[56] Briefly, the entire system is mirrored around the $z = 0$ plane and shifted by half the box length along the other two dimensions. The original system together with its mirror-shifted image is then periodically replicated in all three directions as usual, and all particles interact with their neighbours in the standard way. In other words, every particle interacts with every other particle, as well as its mirror-and-shifted images.

At this point we have a perfectly homogeneous system, and the only force driving the particles across the boundaries is the thermal noise of strength $1/\sqrt{M} \ll 1$. To block this and create the actual walls, a soft repulsive potential

$$U(z) = 0.05 k_B T e^{-z/(2\lambda)} \tag{4}$$

is applied on both sides. The range corresponds to the diameter of one blob, while the amplitude is adjusted so that the particle density in the middle of the box is equal to one.

The resulting confinement force is comparatively weak, and therefore is perceived as a small perturbation to an otherwise homogeneous system. The coveted result is that the particle density (Fig. 4a) goes monotonically from zero outside the box, to one inside the box, without any overshoot or density oscillations. The wall roughness barely exceeds one blob diameter, and is about as sharp as possible. The monotonic density climb is in agreement with all of our NR measurements which strongly rule out the possibility of pronounced density oscillations near the surface.

Grafting and shear

To create a brush, we first generate the locations of the grafting points. For simplicity, they are arranged on a square lattice on the $z = 0$ plane, plus one random number of variance λ in all directions to make it more realistic. To "graft" a chain, we simply add an attractive potential between the grafting point and the central $j = J/2$ monomer:

$$U_{\text{graft}}(\mathbf{r}) = k_B T \cosh(r/\lambda) \tag{5}$$

Half of the grafted chain $j > J/2$ is assigned to the main box and feels the same confinement potential, Eq. (4), as all the free chains. The other half $j < J/2$ is assigned to the mirrored box, and feels the mirrored confinement $U(-z)$. This "grafting" technique is further explained in Ref.[56] In essence, at our coarse scale it is rather important to attach the central monomer and thread the chain halfway through the wall, instead of the more obvious attachment of a chain end, since this would leave a gap between the confining wall and the grafting point, and then the free chains would have a chance to unphysically cross through that gap.

In terms of traditional end-grafted chains, our bristles have an effective length $N = 256/2 = 128$ and there are $B = 2 \times 8 = 16$ of them. The chain length ratio was kept to $P/N = 2$ for simplicity, and is similar to the Brush-long-sparse experimental situation where the ratio is about 3. The grafting density was 0.006 bristles per $\lambda^2 = (a\phi^{-3/4})^2$. This is

about 16 times sparser than the experimental Brush-long-sparse system, but it was chosen on purpose to leave more empty space in which the brush could collapse under a broad range of shear rates, and therefore explore a wider range of conditions than possible experimentally.

The shear flow is generated by adding a Couette velocity profile:

$$\mathbf{v}_{\text{shear}} = \dot{\gamma}|z|\hat{\mathbf{x}} \tag{6}$$

The profile is mirrored across the $z = 0$ plane, so that the $j < J/2$ particles of the grafted chains also feel the shear flow in the correct direction. No slippage or shear-bands were assumed and could not easily occur in our simulation, due to the phenomenologically imposed shear flow profile. A more realistic model could better assume a constant shear stress and let the velocity profile develop instead, but we have not attempted such a simulation.

Results

Our main experimental result is shown in Fig. 2. The applied shear rate $\dot{\gamma}$ is given in dimensionless Weissenberg number

$$\text{Wi} = \dot{\gamma}\tau_d \tag{7}$$

normalized to the longest relaxation time τ_d of the bulk liquid which was measured by oscillatory rheology (see Supplementary Fig. 7). The rheo-NR experiment was performed with two brushes prepared by different chemical methods which gave large differences in grafting density and molecular weight, summarized in Table 1: "grafting-to" produced a long, sparsely grafted brush (Brush-long-sparse, or Brush-LS) while "grafting-from" gave a shorter, denser brush (Brush-short-dense, or Brush-SD). The polymer solution was the same in both cases, $\phi = 30\,\%$ dPS in $70\,\%$ DEP. The NR spectrum is displayed in panels a) and b), showing an increase of 50 % in the reflected intensity between the static and the sheared brush. It is a strong and direct indication that the brush-bulk interface becomes sharper

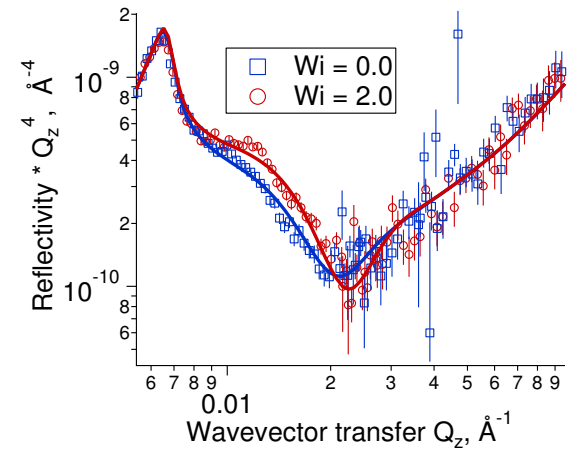

(a) Brush-long-sparse, NR spectrum

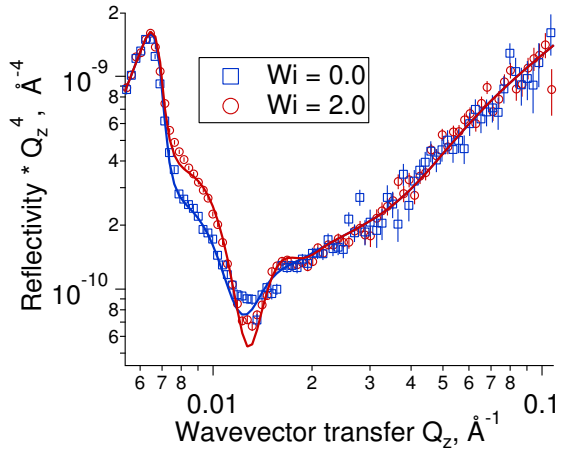

(b) Brush-short-dense, NR spectrum

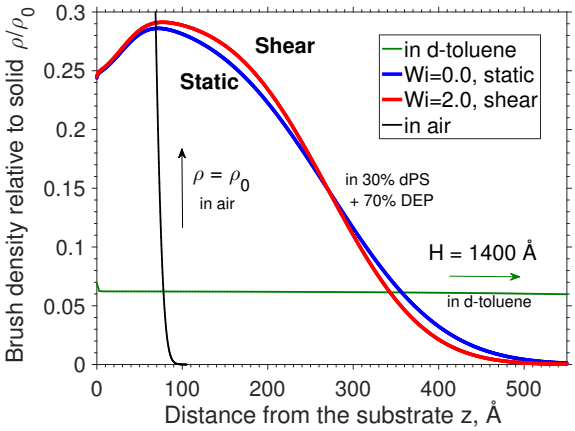

(c) Brush-long-sparse, density profiles

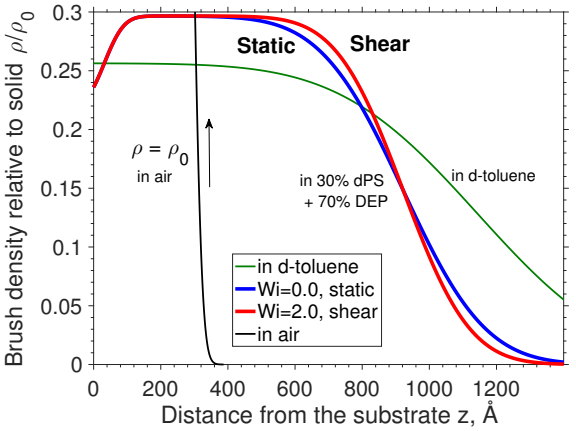

(d) Brush-short-dense, density profiles

Figure 2: Experimentally determined brush structure. Panels a) and b) show NR data (points) and the fits (solid lines) for the two brushes in solution of 30% dPS and 70 % DEP. Panels c) and d) show the corresponding fitted brush density profiles (thick lines), as well as additional fits of NR measurements in air (fully collapsed), and in deuterated toluene (fully stretched). The profiles in air and d-toluene emphasize the differences between the static structure of the two brushes, whereas the relative effect of shear is about the same for both samples.

upon shearing. The shear was cycled on and off multiple times to demonstrate that the effect is reversible and reproducible (see Supplementary Fig. 4).

To quantify the effect more precisely, we have fitted the data [solid lines in panels a) and b)] and revealed the actual brush structure in panels c) and d) respectively. The model used for the fit was verified to be consistent with information obtained by further complimentary measurements, namely the NR spectrum of the brush in air (dry, fully collapsed brush), as well as in a good solvent (maximally swollen brush) which in our case was deuterated toluene. These spectra and details about fitting are available in the SI.

The main difference between the two brushes is their grafting density σ, defined as the number B of chains per substrate area A, normalized by the monomer size of an effective value $a = 7\,\text{Å}$ as given in Ref.:[57]

$$\sigma = \frac{Ba^2}{A}. \tag{8}$$

Experimentally this is obtained by measuring the dry brush thickness in air

$$H_{\text{air}} = a\sigma N, \tag{9}$$

where N is the number of monomers per grafted chain. In the case of the "grafting-from" brush, we do not know N and σ separately. Therefore, the brush is further characterized by immersing it in a good solvent (deuterated toluene at 20 °C), so the brush swells to a height[58]

$$H_{\text{good solvent}} = aNP^{-1/3}\sigma^{1/3}, \tag{10}$$

where $P = 1$ is the length of the free chains, in this case just a single solvent molecule. The dimensionless surface coverage can then be estimated by

$$\sigma = \left(\frac{H_{\text{air}}}{H_{\text{good solvent}}}\right)^{3/2}, \tag{11}$$

comparing the dry brush thickness in air versus the thickness in a good solvent. The estimate

of σ from Eq. (11) is valid for the brushes presented here, however, it should be noted that the theoretical scaling law 3/2 may not be exactly obeyed in general, especially for very low density brushes (mushrooms), or very short chains.

Table 1: Summary of experimental NR results.

	Brush-LS	Brush-SD
Chain length N	2093	808
Grafting density σ	0.016	0.16
H = Mean thickness (slab model), Å		
In air	89	333
In d-toluene	1400	1167
In 30% dPS, 70% DEP	278	958
h = Brush-bulk roughness (Gaussian), Å		
Wi = 0.0 (static)	105	194
Wi = 0.5	–	191
Wi = 1.0	96	–
Wi = 2.0	88	157

The summary of the brush properties determined by NR is listed in Table 1. There is a factor of $\sigma_{\mathrm{SD}}/\sigma_{\mathrm{LS}} = 10$ difference between the grafting densities of the two brushes, as well as a factor of $N_{\mathrm{SD}}/N_{\mathrm{LS}} = 0.4$ difference in chain length. One can better appreciate these numbers by comparing how far the Brush-LS swells in toluene (a good solvent), with respect to a more modest relative swelling of the Brush-SD, as shown in Figs. 2c and 2d. When immersed in a 30 % homopolymer solution, as opposed to a pure solvent, the excluded volume repulsion between the bristles is partially screened and the brush shrinks considerably, but is still much more swollen than the brush in air. In solution, the density profiles show two regions: 1) an interior region close to the wall where the free chains are almost completely expelled, and 2) an overlap region further out where the grafted and free chains overlap and interpenetrate.

Despite the fact that the two brushes are different, the relative effect of shear on both seems to be similar, and is restricted to the overlap region. In the case of Brush-SD, its wide interior region is not affected by shear at all. Therefore, to quantify the relative change in brush structure under shear, we propose to focus on where the effect occurs and use only the

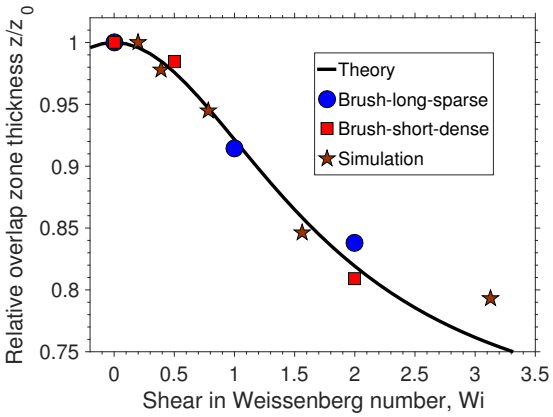

Figure 3: Brush thickness under shear, normalized to the equilibrium thickness. Only the brush-bulk overlap region is considered in this comparison. The fit (solid line) is made using Eq. (21).

mean thickness of the overlap region, which for simplicity we describe by a triangular shape

$$\rho(z) = \phi\left(1 - \frac{z}{h}\right), \quad 0 < z < h \tag{12}$$

and therefore its mean thickness

$$\langle z \rangle = \frac{\int z\rho\, dz}{\int \rho\, dz} = h/3, \tag{13}$$

is simply proportional to the brush-bulk roughness h, and does not involve the full brush thickness H. The relative change in the overlap thickness

$$\frac{\langle z(\mathrm{Wi}) \rangle}{\langle z(0) \rangle} \equiv \frac{h(\mathrm{Wi})}{h(0)} \tag{14}$$

as a function of the applied shear is plotted in Fig. 3. Clearly, in these reduced units both brushes seem to follow a universal behaviour, within the accessible parameter range.

To better understand the brush collapse, a series of computer simulations were performed using a previously reported algorithm for entangled polymer solutions in bulk,[32]

here extended for confined brush-bulk systems under shear flow. We have chosen one set of reasonable parameters resembling the "grafting-to", or Brush-LS sample, and have only varied the applied shear rate. In total, we have used $C = 64$ free chains of length $P = 256$ in contact with a brush containing $B = 16$ grafted chains of length $N = 128$. An entanglement length of $N_e = 59$ was reported in the original study,[32] obtained using primitive path analysis,[59] leading to $Z = P/N_e = 4.3$ entanglements per chain in the bulk. The box volume is set fixed to

$$V = 2\left(\frac{4\pi}{3}\right)\lambda^3(CP + BN) \tag{15}$$

and its aspect ratio is adjusted so that the grafted chains stay far away from the opposite side of the box. To visualise the system, a smaller version was also simulated and the resulting polymer conformations were plotted in 3D, shown as insets in Fig. 1.

Every simulated degree of freedom corresponds to one "blob", which can be mapped to the experimental system using a scaling law[42]

$$N_{\text{blobs}} = \phi^{5/4} N_{\text{monomers}}. \tag{16}$$

The above equation is a theoretical prediction for an ideal semi-dilute solution, up to a numerical prefactor of order one. It may require a correction if the solution is too concentrated $\phi \to 1$, which is likely for our experiment. In any case, we have made no attempt to establish an absolute one-to-one correspondence between simulation and experiment, and will content ourselves by comparing only the relative change of the brush structure as a function of the dimensionless Weissenberg number, as shown in Fig. 3.

One advantage of simulation is that we can explore a much wider range of shear rates than possible experimentally. A shortcoming is that the computation time grows very rapidly $t \propto Z^{4.5}$ (or $t \propto Z^{3.5}$ + overhead for parallel implementations) with the number of entanglements Z, and systems bigger than $Z > 10$ are not very practical. Keeping these considerations in mind, we simulate a lower grafting density, $\sigma_{\text{Sim}} = 0.006$ bristles per λ^2, in comparison

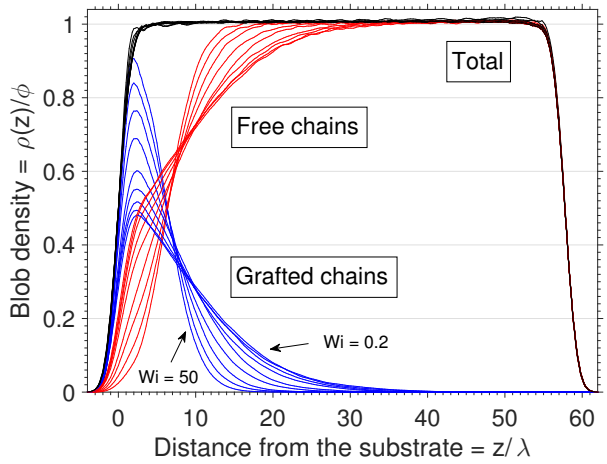

(a) Density profiles under various shear rates given in Weissenberg number $\mathrm{Wi} = \dot{\gamma}\tau_d = 50/2^{1,2,\ldots,9}$.

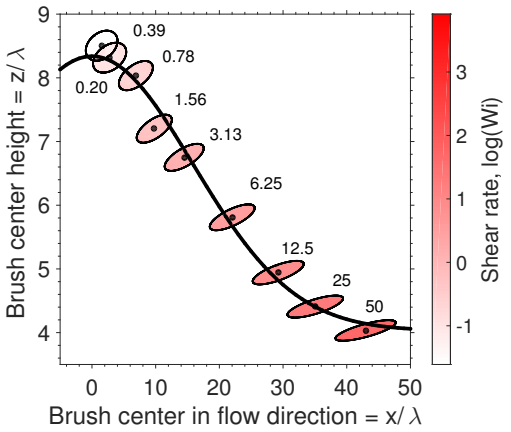

(b) Position of the brush chain centre of mass relative to its grafting point, as defined in Eq. (17). Ellipses show the radius of gyration scaled to the x-axis (see SI).

Figure 4: Simulated brush structure under shear flow

to $\sigma_{\mathrm{LS}} = 0.016$ per $a^2 = \left(\lambda\phi^{3/4}\right)^2$ for the experimental Brush-LS system. The simulated brush is thus fully overlapping with the bulk and we do not waste precious computer time to simulate any interior region which is not crucial for the brush collapse to occur. A broad range of shear rates could then be easily examined, ranging from $\mathrm{Wi} = 0.2$ to $\mathrm{Wi} = 50$. The resulting density profiles are shown in Fig. 4a, where the blob density is normalized to the number of blobs in the box, Eq. (15). Each blob contains a ϕ percentage of polymer and $(1-\phi)$ percentage of solvent as mapped out by Eq. (16). The simulated density profile can be compared with the experimental one in Fig. 2c. Even though there is a roughly $\phi^{-3/2}\sigma_{\mathrm{LS}}/\sigma_{\mathrm{Sim}} = 16$-fold difference in the grafting density and about $\phi^{5/4}N_{\mathrm{LS}}/N_{\mathrm{Sim}} = 3.6$ times difference in the chain length, the overall shape of the brush density profile and its change upon shear seem to be qualitatively similar.

For a more quantitative comparison, we have used the definition in Eq. (13) to calculate the mean thickness of the simulated brush, and plotted the value normalized to equilibrium in Fig. 3. When compared in terms of reduced units, there emerges a single unified trendline between the simulation and the two experiments, suggesting a common mechanism for shear-

induced brush collapse in conditions where the bulk solute is entangled with the brush. Currently, we are not aware of any theoretical description which could calculate the observed brush density profiles (experimental Figs. 2c, 2d and simulation Fig. 4a). A scaling law analysis has earlier been reported[60] which roughly quantifies the brush deformation along the shear flow, but it was only intended for short, unentangled chains in which case there is no normal stress difference and hence no change in brush thickness.

Here we continue in the same scaling law spirit and propose a phenomenological explanation of our entangled brush system. At equilibrium, each bristle has a density profile $\rho(x, z)$ around its grafting point. For simplicity we will restrict ourselves to two dimensions with the z-direction perpendicular to the interface and the flow direction x. Our data indicates (Fig. 2d) that the interior region of the brush (if present) is not affected by shear flow and therefore we will only focus on the overlap region, where the effect takes place. Its center of mass at zero shear is located at

$$\langle x \rangle_0 = \frac{\int x\rho \, dx \, dz}{\int \rho \, dx \, dz} = 0 \tag{17a}$$

$$\langle z \rangle_0 = \frac{\int z\rho \, dx \, dz}{\int \rho \, dx \, dz} \approx h \tag{17b}$$

where h denotes the overlap region thickness. Under a steady shear flow, the center of mass moves to some different location $\langle x, z \rangle$. If the shear rate is very small, one can assume phenomenologically that the displacement along the flow $\langle x \rangle$ is linearly proportional to the shear rate (see Supplementary Fig. 9) and to the overlap thickness:

$$\langle x \rangle = (\dot{\gamma}\tau_d) \langle z \rangle , \tag{18}$$

where τ_d is the brush-bulk relaxation time, presumably governed by reptation: $\tau_d \approx \tau(P/N_e)^3 \approx 10^5\tau$, for the simulated case. The energy penalty of the deformed brush can be estimated by

$$E/k_BT = \langle x - x_0 \rangle^2 + \langle z - z_0 \rangle^2 = (\dot{\gamma}\tau_d \langle z \rangle)^2 + \langle z - z_0 \rangle^2 . \tag{19}$$

A non-linear fluid such as ours exhibits normal stress differences and hence has a mechanism to couple the stress along various axes. The brush will therefore seek an energy minimum which can be found by solving $dE/d\langle z\rangle = 0$, resulting in

$$\langle x\rangle = \left(\frac{\dot{\gamma}\tau_d}{1+(\dot{\gamma}\tau_d)^2}\right)\langle z\rangle_0 \tag{20a}$$

$$\langle z\rangle = \frac{\langle z\rangle_0}{1+(\dot{\gamma}\tau_d)^2} \tag{20b}$$

This reasoning shows that the overall chain deformation will be smallest if the overlap thickness $\langle z\rangle$ shrinks below its equilibrium value, thereby avoiding some of the friction from the free chains flowing by. Of course, the brush cannot shrink to zero height, and will have to saturate to no thinner than its dry state. The simplest modification could be

$$\frac{\langle z\rangle}{\langle z\rangle_0} = \frac{1-\alpha}{1+(\beta\dot{\gamma}\tau_d)^2} + \alpha \tag{21}$$

with fitting parameters $\alpha = 0.68$ and $\beta = 0.57$, used to fit the trend in Fig. 3.

Another great advantage of simulations is that we gain access to practically any quantity or correlation of interest, including for instance the brush center of mass displacement along the flow, $\langle x\rangle$, which is unavailable experimentally. We have plotted the simulated height $\langle z\rangle$ as a function of $\langle x\rangle$ for various shear rates in Fig. 4b. In this plot both axes refer to distances, and therefore we could additionally superimpose the ellipses of inertia showing the radius of gyration of the grafted chains around their respective center of mass (more details can be found in the SI). The ellipses show that not only is the brush displaced, but it is also deformed by the shear flow, stretching in the x-direction, shrinking in the z-direction (and to a lesser extent also shrinking in the y-direction, see SI), and developing an anisotropic tilt, which signals the presence of shear stress.[61] Another possible extension to Eq. (20b) could be a Gaussian shape:

$$\frac{\langle z\rangle}{\lambda} = 4.3\exp\left[-\left(\frac{\langle x\rangle}{22.4\lambda}\right)^2\right] + 4.0 \tag{22}$$

which was used to fit the simulation data in Fig. 4b. This function also shrinks quadratically at small shear rates, $\langle \Delta z \rangle \propto -\langle x \rangle^2$, and saturates to $\langle z \rangle \to$ const. at very large shear rates, but without a proper theory both Eqs. (21) or (22) are just guesses. Actually, the simple theoretical Eq. (20a) predicts that the $\langle x \rangle$-displacement will reach a maximum at $\dot{\gamma}\tau_d = 1$, and then slowly retract to zero. The simulation data in Fig. (4b) clearly rules out this possibility, instead showing that the $\langle x \rangle$-displacement always grows monotonically and eventually saturates to some fixed value.

Discussion

At short time scales the brush behaves like a liquid, while at very long time scales like an elastic solid. The grafted chains of length N relax primarily by the arm retraction mechanism[62] $\tau_a = O(N^3 e^{N/N_e})$. This characteristic time may be further slowed [52] to $\tau_a = O(P^3 N^2 e^{N/N_e})$ during interdigitation with an entangled bulk polymer of length P. These very slow brush-brush relaxation processes do not couple easily to a transverse shear flow: the bristles are immobilised and cannot flow past each other. An applied shear flow only tilts the entire brush structure including its internal topological arrangements, but does not interfere with the inner brush-brush dynamics. The truly interesting coupling is between the brush and the bulk chains. These flow past each other and therefore the brush-bulk overlap region should show similar behaviours to those of the pure bulk fluid, including shear thinning and normal stress differences, expected to occur at a time scale $\tau_d = O(P^3)$ dictated by the reptation of the free chains, which should overwhelm the slower arm retraction of the brush.

The structural change observed by NR occurs almost instantly upon switching on the shear for both Brush-LS and Brush-SD, suggesting that the brush-bulk dynamics are governed by a relaxation process faster than the NR time resolution (about 1 min), and therefore consistent with reptation dynamics $\tau_d \approx 1\,\mathrm{s}$. Overall, the brush-bulk relaxation is too fast to measure with our current setup, and the upper limit is about one minute. More information

on the kinetics of the brush may be obtained in the future, using an oscillatory shear flow combined with stroboscopic NR.[63] If arm retraction of the brush was to play a role, the relaxation time should be exponentially e^{N/N_e} longer, and very much different for the two brushes: $\tau_{\mathrm{LS}}/\tau_{\mathrm{SD}} = (N_{\mathrm{LS}}/N_{\mathrm{SD}})^3 e^{(N_{\mathrm{LS}}-N_{\mathrm{SD}})/N_e} \approx 100$. In our experiment we could not detect any difference in the dynamics of the two brushes, and therefore conclude that the effect of coupling to shear flow is governed by the free chain reptation, not by the brush itself. This conclusion is corroborated by the fact that the relative brush collapse of both experimental systems and the simulation fall onto a master curve (see Fig. 3) in spite of the different grafting densities and chain lengths of the three systems.

We emphasize that the universality of the brush collapse refers only to the brush-bulk overlap region, and does not take into account the interior brush region, which was shown here (Fig. 2d) not to couple to the transverse shear flow, at least for the experimentally accessible shear rates. In fact, for very dense brushes the overlap region becomes too narrow to entangle with the bulk chains, in which case we could not observe any NR signal change upon shear (data not shown). We can say that the saturation parameter in Eq. (21) becomes $\alpha = 1$, meaning that for these very dense brushes the overlap region is already fully collapsed even at shear rate $\dot{\gamma} = 0$.

One important parameter range that we have not explored is when the grafted chains are much longer than the free chains $N \gg P$, and the grafting density is sufficiently low so that more than one free chain can entangle with every grafted chain. In such a scenario the concentration of the brush is too faint to be detected by NR, at least with our present setup. Regardless of neutrons, it may happen for this system that the brush starts collapsing at $\mathrm{Wi} \ll 1$, much sooner than the shear-thinning can erode the viscosity of the bulk liquid. If this is the case, then it may be possible[64] that the liquid loses grip with the surface and displays a large shear-dependent surface slip. In all the cases that we studied, $N \lesssim P$, brush collapse happens at the same time as the shear-thinning in the bulk, which prevents a large slip from occurring. So far it has not been possible to characterize an appropriate $N \gg P$

system, and the surface slip question remains open.

In summary, we have used a combination of *in situ* rheo-neutron reflectometry, coarse grained computer simulations and phenomenological theory to show that it is possible to engineer polymer brushes responding to shear stimuli exerted by an entangled polymer solution. At the same time we provide strong evidence that the time scale of this shear response is governed by the solution dynamics, which sets a clear limit on the tailoring of the shear-response of polymer brushes.

Data availability

Neutron reflectometry data is available at doi.ill.fr/10.5291/ILL-DATA.9-11-1683, doi.ill.fr/10.5291/ILL-DATA.9-11-1784, doi.ill.fr/10.5291/ILL-DATA.9-11-1723, doi.ill.fr/10.5291/ILL-DATA.9-11-1745

Simulation algorithm is a custom written Matlab code, available upon request to the corresponding author A.K.

Author contributions

The experiment was designed by M.W., P.G., A.K., and F.R. The "grafting-to" brush was made by A.C. and F.R. The "grafting-from" brush was made by A.S.P. and C.R.E. with participation of A.K. Rheo-NR data was collected and analysed by P.G. and A.K. with participation of M.W., A.C., and F.A. Simulations and theory were performed by A.K. The manuscript was written by A.K. with the contribution of all authors. The authors declare no competing financial interests.

Acknowledgements

The authors thank Jean-Louis Barrat and Lilliane Léger for their invaluable comments and help. We also acknowledge the use of the Partnership for Soft Condensed Matter (PSCM) facilities and the ILL for according beam time.

References

(1) Milner, S. T. Polymer Brushes. *Science* **1991**, *251*, 905–914.

(2) Brittain, W. J.; Minko, S. A structural definition of polymer brushes. *Journal of Polymer Science Part A: Polymer Chemistry* **2007**, *45*, 3505–3512.

(3) Schöttler, S.; Becker, G.; Winzen, S.; Steinbach, T.; Mohr, K.; Landfester, K.; Mailänder, V.; Wurm, F. R. Protein adsorption is required for stealth effect of poly (ethylene glycol)-and poly (phosphoester)-coated nanocarriers. *Nature nanotechnology* **2016**, *11*, 372–377.

(4) Butcher, N. J.; Mortimer, G. M.; Minchin, R. F. Drug delivery: Unravelling the stealth effect. *Nature nanotechnology* **2016**,

(5) Azzaroni, O. Polymer brushes here, there, and everywhere: Recent advances in their practical applications and emerging opportunities in multiple research fields. *Journal of Polymer Science Part A: Polymer Chemistry* **2012**, *50*, 3225–3258.

(6) Bauer, M.; Kekicheff, P.; Iss, J.; Fajolles, C.; Charitat, T.; Daillant, J.; Marques, C. M. Sliding tethered ligands add topological interactions to the toolbox of ligand-receptor design. *Nature Communication* **2015**, *6*.

(7) Raviv, U.; Giasson, S.; Kampf, N.; Gohy, J.-F.; Jérôme, R.; Klein, J. Lubrication by charged polymers. *Nature* **2003**, *425*, 163–165.

(8) Klein, J. Repair or Replacement–A Joint Perspective. *Science* **2009**, *323*, 47–48.

(9) Yang, H.; Esteves, A. C. C.; Zhu, H.; Wang, D.; Xin, J. H. In-situ study of the structure and dynamics of thermo-responsive PNIPAAm grafted on a cotton fabric. *Polymer* **2012**, *53*, 3577–3586.

(10) Pinto, J.; Whiting, G.; Khodabakhsh, S.; Torre, L.; Rodríguez, A.; Dalgliesh, R.; Higgins, A.; Andreasen, J.; Nielsen, M.; Geoghegan, M.; Huck, W.; Sirringhaus, H. Organic Thin Film Transistors with Polymer Brush Gate Dielectrics Synthesized by Atom Transfer Radical Polymerization. *Advanced Functional Materials* **2008**, *18*, 36–43.

(11) Youm, S. G.; Hwang, E.; Chavez, C. A.; Li, X.; Chatterjee, S.; Lusker, K. L.; Lu, L.; Strzalka, J.; Ankner, J. F.; Losovyj, Y.; Garno, J. C.; Nesterov, E. E. Polythiophene Thin Films by Surface-Initiated Polymerization: Mechanistic and Structural Studies. *Chemistry of Materials* **2016**, *28*, 4787–4804.

(12) Reinhardt, M.; Dzubiella, J.; Trapp, M.; Gutfreund, P.; Kreuzer, M.; Gröschel, A. H.; Müller, A. H. E.; Ballauff, M.; Steitz, R. Fine-Tuning the Structure of Stimuli-Responsive Polymer Films by Hydrostatic Pressure and Temperature. *Macromolecules* **2013**, *46*, 6541–6547.

(13) Brown, A. A.; Azzaroni, O.; Huck, W. T. S. Photoresponsive Polymer Brushes for Hydrophilic Patterning. *Langmuir* **2009**, *25*, 1744–1749.

(14) Lutz, J.-F. Thermo-Switchable Materials Prepared Using the OEGMA-Platform. *Advanced Materials* **2011**, *23*, 2237–2243.

(15) Tokareva, I.; Minko, S.; Fendler, J. H.; Hutter, E. Nanosensors based on responsive polymer brushes and gold nanoparticle enhanced transmission surface plasmon resonance spectroscopy. *Journal of the American Chemical Society* **2004**, *126*, 15950–15951.

(16) Stuart, M. A. C.; Huck, W. T. S.; Genzer, J.; Mueller, M.; Ober, C.; Stamm, M.; Sukhorukov, G. B.; Szleifer, I.; Tsukruk, V. V.; Urban, M.; Winnik, F.; Zauscher, S.; Luzinov, I.; Minko, S. Emerging applications of stimuli-responsive polymer materials. *Nature Materials* **2010**, *9*, 101–113.

(17) Milner, S.; Witten, T.; Cates, M. Theory of the grafted polymer brush. *Macromolecules* **1988**, *21*, 2610–2619.

(18) Murat, M.; Grest, G. S. Interaction between grafted polymeric brushes: A molecular-dynamics study. *Physical review letters* **1989**, *63*, 1074.

(19) Binder, K.; Milchev, A. Polymer brushes on flat and curved surfaces: How computer simulations can help to test theories and to interpret experiments. *Journal of Polymer Science Part B: Polymer Physics* **2012**, *50*, 1515–1555.

(20) Kelley, T. W.; Schorr, P. A.; Johnson, K. D.; Tirrell, M.; Frisbie, C. D. Direct force measurements at polymer brush surfaces by atomic force microscopy. *Macromolecules* **1998**, *31*, 4297–4300.

(21) Jones, R. A.; Richards, R. W. *Polymers at surfaces and interfaces*; Cambridge University Press, 1999.

(22) Currie, E.; Norde, W.; Stuart, M. C. Tethered polymer chains: surface chemistry and their impact on colloidal and surface properties. *Advances in Colloid and Interface Science* **2003**, *100–102*, 205 – 265.

(23) Kato, K.; Uchida, E.; Kang, E.-T.; Uyama, Y.; Ikada, Y. Polymer surface with graft chains. *Progress in Polymer Science* **2003**, *28*, 209 – 259.

(24) Malham, I. B.; Bureau, L. Density effects on collapse, compression, and adhesion of thermoresponsive polymer brushes. *Langmuir* **2009**, *26*, 4762–4768.

(25) La Spina, R.; Tomlinson, M. R.; Ruiz-Pérez, L.; Chiche, A.; Langridge, S.; Geoghegan, M. Controlling network–brush interactions to achieve switchable adhesion. *Angewandte Chemie International Edition* **2007**, *46*, 6460–6463.

(26) Durliat, E.; Hervet, H.; Leger, L. Influence of grafting density on wall slip of a polymer melt on a polymer brush. *Europhysics Letters* **1997**, *38*, 383.

(27) Léger, L.; Raphal, E.; Hervet, H. *Polymers in confined environments*; Adv. Polymer Sci.; Springer, 1999; Vol. 138; pp 185–225.

(28) Cohen, C.; Restagno, F.; Poulard, C.; Leger, L. Incidence of the molecular organization on friction at soft polymer interfaces. *Soft Matter* **2011**, *7*, 8535–8541.

(29) Thorsen, T.; Maerkl, S.; Quake, S. Microfluidic large-scale integration. *Science* **2002**, *298*, 580–584.

(30) Raviv, U.; Giasson, S.; Kampf, N.; Gohy, J.-F.; Jerome, R.; Klein, J. Lubrication by charged polymers. *Nature* **2003**, *425*, 163–165.

(31) Larson, R. G.; Desai, P. S. Modeling the rheology of polymer melts and solutions. *Annual Review of Fluid Mechanics* **2015**, *47*, 47–65.

(32) Korolkovas, A.; Gutfreund, P.; Barrat, J.-L. Simulation of Entangled Polymer Solutions. *The Journal of Chemical Physics* **2016**, *145*, 124113.

(33) Wolff, M.; Kuhns, P.; Liesche, G.; Ankner, J. F.; Browning, J. F.; Gutfreund, P. Combined neutron reflectometry and rheology. *Journal of Applied Crystallography* **2013**, *46*, 1729–1733.

(34) Grest, G. S. *Polymers in Confined Environments*; Springer, 1999; pp 149–183.

(35) Binder, K.; Kreer, T.; Milchev, A. Polymer brushes under flow and in other out-of-equilibrium conditions. *Soft Matter* **2011**, *7*, 7159–7172.

(36) Müller, M.; Pastorino, C. Cyclic motion and inversion of surface flow direction in a dense polymer brush under shear. *EPL (Europhysics Letters)* **2007**, *81*, 28002.

(37) Singh, M. K.; Ilg, P.; Espinosa-Marzal, R. M.; Kröger, M.; Spencer, N. D. Polymer Brushes under Shear: Molecular Dynamics Simulations Compared to Experiments. *Langmuir* **2015**, *31*, 4798–4805.

(38) Mendonça, A. C.; Goujon, F.; Malfreyt, P.; Tildesley, D. J. Monte Carlo simulations of the static friction between two grafted polymer brushes. *Physical Chemistry Chemical Physics* **2016**, *18*, 6164–6174.

(39) Pastorino, C.; Binder, K.; Kreer, T.; Müller, M. Static and dynamic properties of the interface between a polymer brush and a melt of identical chains. *The Journal of chemical physics* **2006**, *124*, 064902.

(40) Römer, F.; Fedosov, D. Dense brushes of stiff polymers or filaments in fluid flow. *EPL (Europhysics Letters)* **2015**, *109*, 68001.

(41) Saphiannikova, M. G.; Pryamitsyn, V. A.; Cosgrove, T. Self-consistent Brownian dynamics simulation of polymer brushes under shear. *Macromolecules* **1998**, *31*, 6662–6668.

(42) de Gennes, P. G. *Scaling Concepts in Polymer Physics*; Cornell University Press, 1979.

(43) Bolhuis, P.; Louis, A.; Hansen, J.; Meijer, E. Accurate effective pair potentials for polymer solutions. *The Journal of Chemical Physics* **2001**, *114*, 4296–4311.

(44) Nikunen, P.; Vattulainen, I.; Karttunen, M. Reptational dynamics in dissipative particle dynamics simulations of polymer melts. *Physical Review E* **2007**, *75*, 036713.

(45) Baker, S. M.; Smith, G. S.; Anastassopoulos, D. L.; Toprakcioglu, C.; Vradis, A. A.; Bucknall, D. G. Structure of Polymer Brushes under Shear Flow in a Good Solvent. *Macromolecules* **2000**, *33*, 1120–1122.

(46) Ivkov, R.; Butler, P. D.; Satija, S. K.; Fetters, L. J. Effect of Solvent Flow on a Polymer Brush: A Neutron Reflectivity Study of the Brush Height and Chain Density Profile. *Langmuir* **2001**, *17*, 2999–3005.

(47) Sasa, L. A.; Yearley, E. J.; Jablin, M. S.; Gilbertson, R. D.; Lavine, A. S.; Majewski, J.; Hjelm, R. P. Shear-induced metastable states of end-grafted polystyrene. *Physical Review E* **2011**, *84*, 021803.

(48) Wolff, M.; Gutfreund, P.; Rühm, A.; Akgun, B.; Zabel, H. Nanoscale discontinuities at the boundary of flowing liquids: a look into structure. *Journal of Physics: Condensed Matter* **2011**, *23*, 184102.

(49) Chennevière, A.; Cousin, F.; Boué, F.; Drockenmuller, E.; Shull, K. R.; Léger, L.; Restagno, F. Direct Molecular Evidence of the Origin of Slip of Polymer Melts on Grafted Brushes. *Macromolecules* **2016**, *49*, 2348–2353.

(50) Weissenberg, K. A continuum theory of rheological phenomena. *Nature* **1947**, *159*, 310–311.

(51) Rodriguez-Emmenegger, C.; Janel, S.; de los Santos Pereira, A.; Bruns, M.; Lafont, F. Quantifying bacterial adhesion on antifouling polymer brushes via single-cell force spectroscopy. *Polymer Chemistry* **2015**, *6*, 5740–5751.

(52) Chennevière, A.; Drockenmuller, E.; Damiron, D.; Cousin, F.; Boué, F.; Restagno, F.; Léger, L. Quantitative Analysis of Interdigitation Kinetics between a Polymer Melt and a Polymer Brush. *Macromolecules* **2013**, *46*, 6955–6962.

(53) Ell, J. R.; Mulder, D. E.; Faller, R.; Patten, T. E.; Kuhl, T. L. Structural determination of high density, ATRP grown polystyrene brushes by neutron reflectivity. *Macromolecules* **2009**, *42*, 9523–9527.

(54) Campbell, R.; Wacklin, H.; Sutton, I.; Cubitt, R.; Fragneto, G. FIGARO: The new horizontal neutron reflectometer at the ILL. *The European Physical Journal Plus* **2011**, *126*, 107.

(55) Gay, C. Wetting of a polymer brush by a chemically identical polymer melt. *Macromolecules* **1997**, *30*, 5939–5943.

(56) Korolkovas, A. Simulating confined particles with a flat density profile. *Physical Review E* **2016**, *94*, 021302.

(57) Karim, A.; Satija, S. K.; Douglas, J. F.; Ankner, J. F.; Fetters, L. J. Neutron Reflectivity Study of the Density Profile of a Model End-Grafted Polymer Brush: Influence of Solvent Quality. *Physical Review Letters* **1994**, *73*, 3407–3410.

(58) Leibler, L.; Ajdari, A.; Mourran, A.; Coulon, G.; Chatenay, D. *Ordering in Macromolecular Systems*; Springer, 1994; pp 301–311.

(59) Karayiannis, N. C.; Kröger, M. Combined molecular algorithms for the generation, equilibration and topological analysis of entangled polymers: Methodology and performance. *International journal of molecular sciences* **2009**, *10*, 5054–5089.

(60) Kreer, T. Polymer-brush lubrication: a review of recent theoretical advances. *Soft matter* **2016**, *12*, 3479–3501.

(61) Janeschitz-Kriegl, H. *Polymer melt rheology and flow birefringence*; Springer Science & Business Media, 2012; Vol. 6.

(62) Lang, M.; Werner, M.; Dockhorn, R.; Kreer, T. Arm Retraction Dynamics in Dense Polymer Brushes. *Macromolecules* **2016**, *49*, 5190–5201.

(63) Adlmann, F. A.; Gutfreund, P.; Ankner, J.; Browning, J.; Parizzi, A.; Vacaliuc, B.; Halbert, C.; Rich, J.; Dennison, A.; Wolff, M. Towards neutron scattering experiments

with sub-millisecond time resolution. *Journal of Applied Crystallography* **2015**, *48*, 220–226.

(64) Brochard, F.; De Gennes, P. G. Shear-dependent slippage at a polymer/solid interface. *Langmuir* **1992**, *8*, 3033–3037.

Graphical TOC Entry

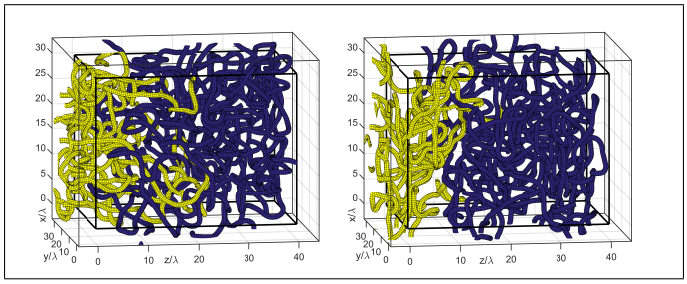

Polymer brush collapse under shear flow

Supplementary Information

Airidas Korolkovas,* Cesar Rodriguez-Emmenegger, Andres de los Santos Pereira, Alexis Chennevière, Frédéric Restagno, Maximilian Wolff, Franz Adlmann, Andrew J.C. Dennison, and Philipp Gutfreund*

E-mail: korolkovas@ill.fr; gutfreund@ill.fr

Physical characterisation of the brushes

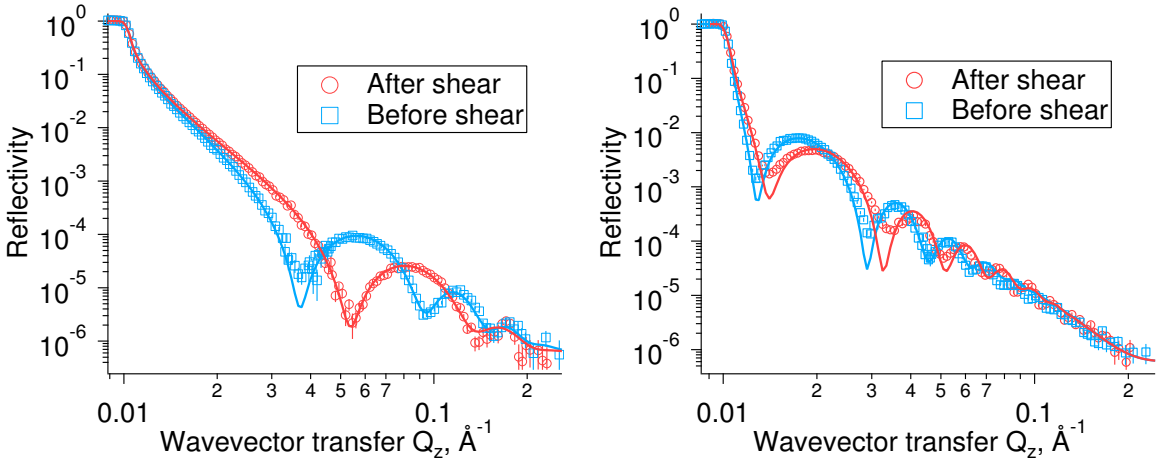

(a) Brush-long-sparse (b) Brush-short-dense

Supplementary Figure 1: Neutron reflectivity in air

The physical characterisation of a brush starts with a NR measurement in air shown in Supplementary Fig. 1. The dry brush thickness H_{dry} can be determined by the distance

between consecutive fringes ΔQ:

$$H_{\mathrm{dry}} = \frac{2\pi}{\Delta Q} \tag{S.1}$$

A more precise result, listed in Table 1, was obtained by fitting the entire spectrum using standard Motofit software, which also takes into account the native silicon dioxide layer, 18 Å and 24 Å thick, respectively.

After all the shear experiments, the brushes were thoroughly rinsed with toluene to remove any ungrafted chains. The dry air measurement was repeated again and revealed that the samples have lost 12 % and 34 % of their original thickness, respectively. We presume that the brushes were gradually degraded by the strong shear stress. To simplify the remaining analysis, we will use the average thickness of before and after measurements, and assume it constant throughout the experiment.

In the dry state, the brush is fully collapsed and its height is calculated by

$$H_{\mathrm{air}} = a\sigma N \tag{S.2}$$

where $N \propto M_w$ is the number of monomers, σ is the dimensionless grafting density, and a is the size of the monomer. In the case of the "grafting-from" brush, we do not know N and σ separately. Therefore, the brush is further characterized by immersing it in a good solvent (deuterated toluene at 20 °C), so the brush swells to a height

$$H_{\text{good solvent}} = aNP^{-1/3}\sigma^{1/3}, \tag{S.3}$$

where $P = 1$ is the length of the free chains, in this case just a single solvent molecule. The dimensionless surface coverage can then be estimated by

$$\sigma = \left(\frac{H_{\mathrm{air}}}{H_{\text{good solvent}}}\right)^{3/2}. \tag{S.4}$$

The corresponding NR result is shown in Supplementary Fig. 2. To fit the data, we have

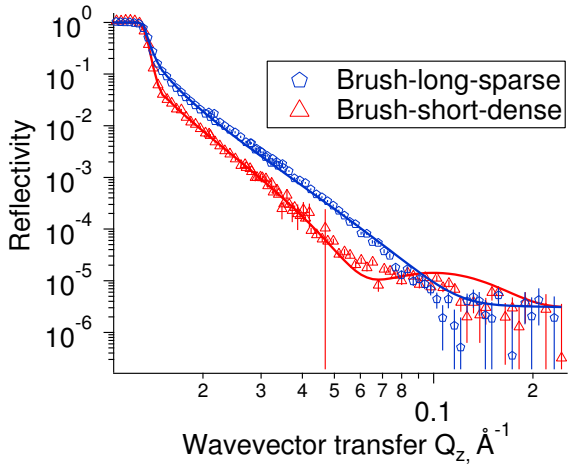

Supplementary Figure 2: Brushes swollen in deuterated toluene

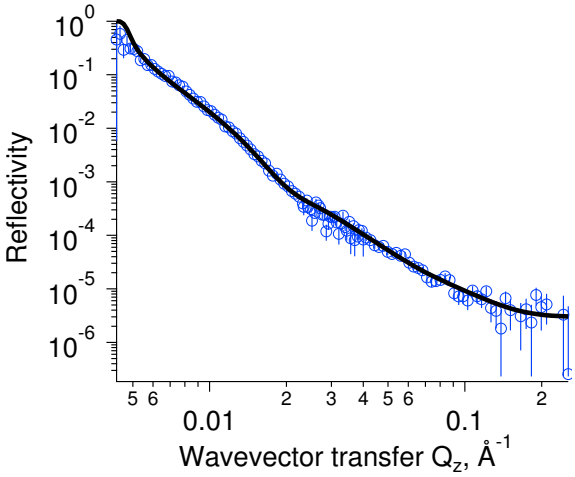

Supplementary Figure 3: Brush-long-sparse in solution of 10 % hPS + 20 % dPS + 70 % DEP

assumed that the total mass of the brush is conserved, and therefore the brush height is constrained to be

$$H_{\text{good solvent}} = H_{\text{air}}/\phi_g, \tag{S.5}$$

where $0 < \phi_g < \phi$ is the concentration of the grafted chains, obtained from the fitted neutron scattering length density (SLD) of the brush layer:

$$\underbrace{\text{SLD[hPS-dTOL]}}_{\text{from fit}} = \underbrace{\text{SLD[hPS]}}_{1.41}\,\phi_g + \underbrace{\text{SLD[dTOL]}}_{5.74}(1-\phi_g) \tag{S.6}$$

In the case of the Brush-short-dense we had to include an insoluble 13 Å thick layer with SLD $= 1.41 \times 10^{-6}$ Å^{-2} at the base of the brush. It is attributed to the bulky ATRP initiator molecule which has a similar SLD to the h-polystyrene, but does not swell in toluene. This thickness is subtracted from the apparent dry brush thickness in air, Eq. (S.1), where the two species are almost indistinguishable for neutrons.

Using Eqs. (S.2), (S.3), and the known chain length $N_{\text{LS}} = 2093$ of the Brush-long-sparse,

we can estimate the unknown Brush-short-dense length:

$$N_{\mathrm{SD}} = N_{\mathrm{LS}} \left(\frac{H_{\mathrm{SD}}}{H_{\mathrm{LS}}} \right)^{3/2}_{\mathrm{wet}} \left(\frac{H_{\mathrm{LS}}}{H_{\mathrm{SD}}} \right)^{1/2}_{\mathrm{dry}} = 808. \tag{S.7}$$

In the following stage, we remove the toluene by blow drying, and load the dPS-DEP solution of density $\phi = 0.3$. The repulsion between the bristles is now mostly screened by the bulk $P = 5570$ chains and the brush density profile should shrink to more of a Gaussian with height

$$H_{\mathrm{Gauss}} = aN^{1/2}. \tag{S.8}$$

The data in Figures 2a and 2b is fitted by constraining the brush density not to exceed the bulk level of $\phi = 0.3$, and maintaining the conservation of mass within reasonable bounds of 10 %. Here we should mention that while the brush density profile changes under shear, the overall polymer concentration cannot be affected much. The relative polymer density change $\Delta\phi/\phi$ can be estimated by comparing the pressure on the cone (normal force measured at no more than $F = 5\,\mathrm{N}$, spread out over a disc of radius $r = 2.5\,\mathrm{cm}$, see also Supplementary Fig. 8), against the osmotic pressure Π of the polymer solution:

$$\frac{\Delta\phi}{\phi} \approx \frac{\Delta\Pi}{\Pi} \approx \frac{F\lambda^3}{\pi r^2 k_B T} \approx 0.001, \tag{S.9}$$

where we have estimated the blob size at $\lambda \approx a/\phi^{3/4} \approx 7\,\mathrm{Å}$. Thus we can see that the shear-induced concentration change is minuscule and can be disregarded.

The NR fits are considerably improved if we allow for a slightly depleted ($\phi_d \approx 0.24$) thin layer at the base of the brush. This assumption is verified by measuring the brush in a different contrast, consisting of 10 % hPS and 20 % dPS solution in DEP, shown in Supplementary Fig. 3 for the Brush-long-sparse. The fit was produced assuming the same brush structure, but different SLD weights. The only small discrepancy was that in the second contrast, the thin depletion layer had a smaller density of $\phi_g = 0.18$. The final brush

height reported in Table 1 is just the sum of the depleted and the main brush layers.

It is apparent that the simple Eq. (S.8) is not obeyed by our samples: $(H_{\mathrm{SD}}/H_{\mathrm{LS}} = 3.4) \neq (\sqrt{N_{\mathrm{SD}}/N_{\mathrm{LS}}} = 0.6)$. Therefore, the brushes cannot be considered Gaussian, especially the denser Brush-short-dense. In the case of polymer melt, one could interpolate Eqs. (S.2), (S.3) and (S.8) with this function:

$$H = aN^{1/2}\left(1 + \frac{N^{1/2}\sigma^{1/3}}{P^{1/3}}\left(1 + \sigma^{2/3}P^{1/3}\right)\right) \tag{S.10}$$

$$= aN^{1/2}\left(1 + \left(\frac{N}{P}\right)^{1/2}\left(P\sigma^2\right)^{1/6}\left(1 + \left(P\sigma^2\right)^{1/3}\right)\right) \tag{S.11}$$

In a semi-dilute solution of density $(\phi^* \approx 0.03) < (\phi = 0.3) < (\phi^{**} \approx 0.5)$, the above equation can be extended by a mapping from the blob theory: $N \to \phi^{5/4}N$, $P \to \phi^{5/4}P$, $a \to \lambda = a\phi^{-3/4}$ and $\sigma \to (\lambda/a)^2\sigma = \phi^{-3/2}\sigma$. The brush height in the general case can then be interpolated as

$$H = a\left(\frac{N}{\phi^{1/4}}\right)^{1/2}\left(1 + \alpha\left(\frac{N}{P}\right)^{1/2}\beta\left(\frac{P\sigma^2}{\phi^{7/4}}\right)^{1/6}\left(1 + \beta^2\left(\frac{P\sigma^2}{\phi^{7/4}}\right)^{1/3}\right)\right). \tag{S.12}$$

The above equation is fitted using our six height measurements, to obtain the three fitting parameters: $a = 1.19\,\text{Å}$, $\alpha = 1.95$, and $\beta = 0.94$. The locations of the various brush states are indicated in the phase diagram, Supplementary Fig. (5). It turns out that the Brush-short-dense in 30 % dPS solution is best described as dry, meaning that the free dPS chains are largely expelled from the brush. The Brush-long-sparse is quite close to the triple cross-over between dry, Gaussian and stretched, but leans more to the dry side.

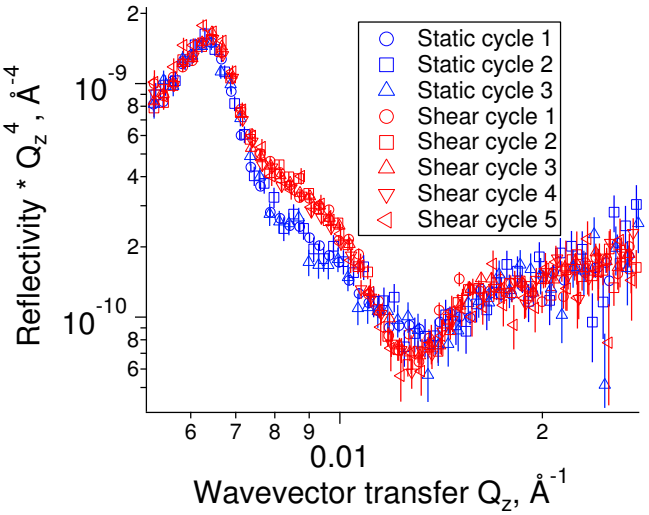

Supplementary Figure 4: Reproducibility of the brush collapse (Brush-short-dense sample)

Confirmation of Chemical Structure of PS Brushes via FTIR spectroscopy

The chemical structure of the "grafted-from" PS Brush-short-dense was confirmed via Fourier-transform infrared spectroscopy in attenuated total reflectance mode (ATR-FTIR) employing a Nexus 870 spectrometer (Nicolet, Czech Republic) equipped with a VariGATR ATR accessory (Harrick Scientific Products, USA). Measurements were performed using 256 scans at $4\,\mathrm{cm}^{-1}$ on a sample prepared in parallel with the sample for neutron reflectometry. The spectrum obtained is shown in Supplementary Fig. 6, displaying features characteristic for PS. The CH_2 stretching modes of the polymer backbone are observed at $2924\,\mathrm{cm}^{-1}$ (symmetric) and $2850\,\mathrm{cm}^{-1}$ (asymmetric) while the band at $1452\,\mathrm{cm}^{-1}$ arises mostly from the CH_2 bending mode. A series of 5 weak bands between 1945 and $1672\,\mathrm{cm}^{-1}$ are the result of combination vibrations of the aromatic ring and the bands appearing at 1602 and $1492\,\mathrm{cm}^{-1}$ arise from in-plane ring vibrations. The strong bands at 702 and $760\,\mathrm{cm}^{-1}$ correspond to out-of-plane ring deformations.

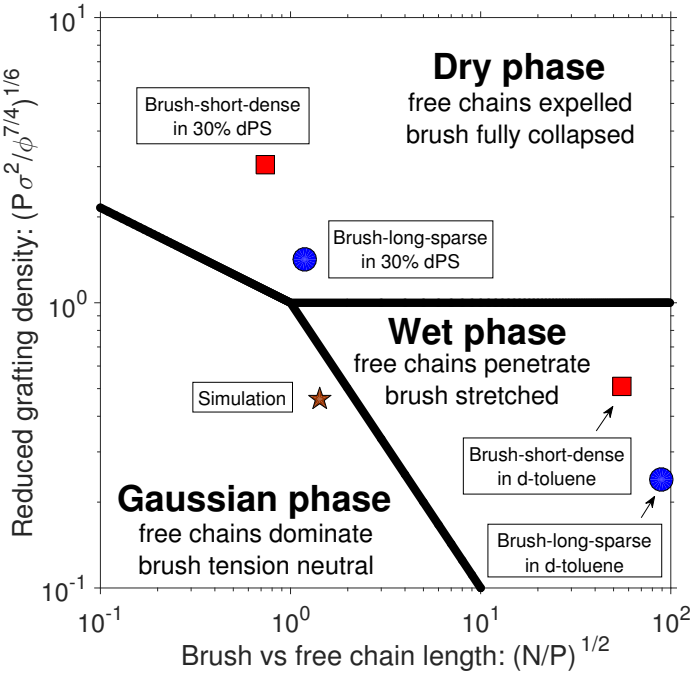

Supplementary Figure 5: Thermodynamic phase diagram indicating the various brush states.

Rheological characterisation

The viscoelastic properties of the bulk dPS solution were characterised by measuring the storage $G'(\omega)$ and loss $G''(\omega)$ moduli against the angular frequency ω of the applied shear rate, shown in Supplementary Fig. 7. The curves are typical for a viscoelastic fluid, and their cross-over at frequency $\omega^* = 10\,\mathrm{s}^{-1}$ determines the longest relaxation time of the bulk polymer, in this case $\tau_d = 1/\omega^* = 0.1\,\mathrm{s}$. The shear stress as well as the normal stress measured during the NR data acquisition is also shown in Supplementary Fig. 8. It is clear that that after $\mathrm{Wi} \gtrsim 1$ we enter into a non-Newtonian shear-thinning regime. The outwards normal stress on the cone also starts rapidly increasing at this point. These rheological observations coincide closely with the onset of the brush collapse as measured by NR.

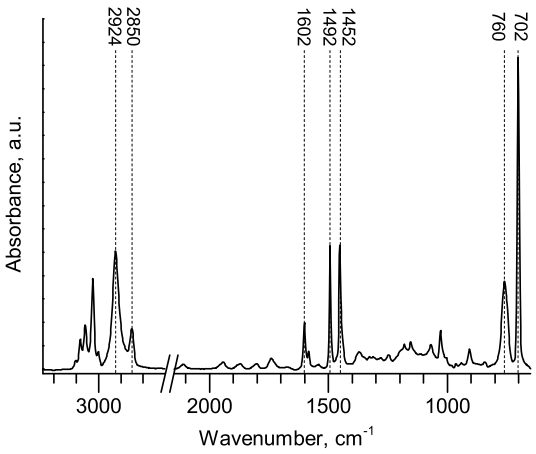

Supplementary Figure 6: FTIR spectrum of "grafted-from" PS brush

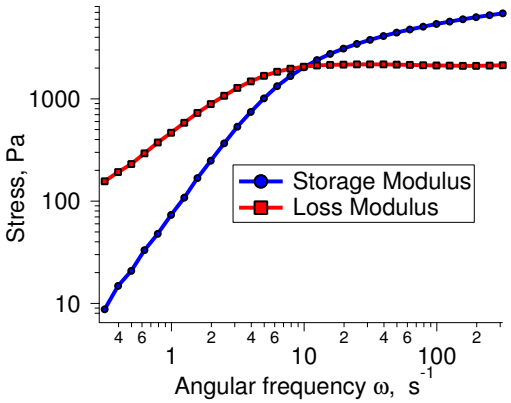

Supplementary Figure 7: Storage and loss moduli of 30 % dPS solution in DEP at 5 % strain amplitude.

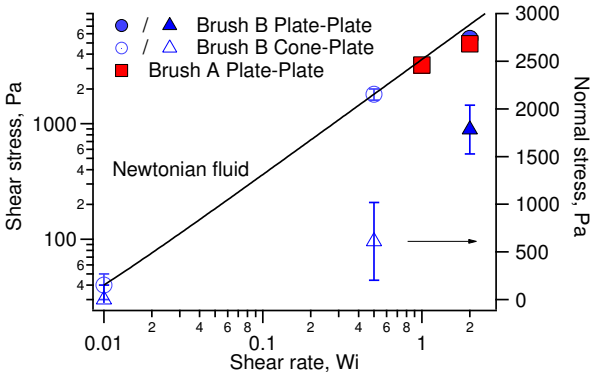

Supplementary Figure 8: Steady-state shear and normal stresses as recorded during the *in situ* rheo-NR measurements

Simulated brush structural analysis

The density profiles in Fig. 4a are histograms obtained by counting the number of particles in small bins and averaging over about $10\tau_d$ time steps. Further information on the brush structure is obtained by calculating the average position of the center of mass for the average bristle, with respect to its grafting point. The mean position is shown by black points in Fig. 4b. We have also calculated the components of the inertia tensor:

$$R_{\alpha\beta} = \langle (R - R_0)_\alpha (R - R_0)_\beta \rangle \,, \tag{S.13}$$

where $\mathbf{R}_0$ is the instantaneous position of the center of mass, and the average is taken over all the j-particles. At equilibrium, the sum of diagonals $R_{xx} + R_{yy} + R_{zz} = R_g^2$ is known as the radius of gyration. Under shear, there will also be a non-zero off-diagonal component R_{xz} and the inertia tensor can be described as an ellipse. To quantify its shape, we must solve the diagonalization problem:

$$(R_{xx} - A)\cos\alpha + R_{xz}\sin\alpha = 0 \tag{S.14}$$

$$R_{xz}\cos\alpha + (R_{zz} - A)\sin\alpha = 0 \tag{S.15}$$

The solution is the tilt angle:

$$\tan 2\alpha = \frac{2R_{xz}}{R_{xx} - R_{zz}} \tag{S.16}$$

and the principal axes of inertia:

$$R_{1,2} = \frac{1}{2}\left[(R_{xx} + R_{zz}) \pm \sqrt{(R_{xx} - R_{zz})^2 + 4R_{xz}^2}\right] \tag{S.17}$$

The resulting ellipse is drawn around the position of the brush center in Fig. 4b. The ellipse dimensions are scaled to the values on the x-axis, which has a ratio of 10:1 with respect to the y-axis. The shear rate in Weissenberg number is denoted by the color inside each ellipse and also the number next to it. The full dataset is further shown in Supplementary Fig. 9 in a plain format.

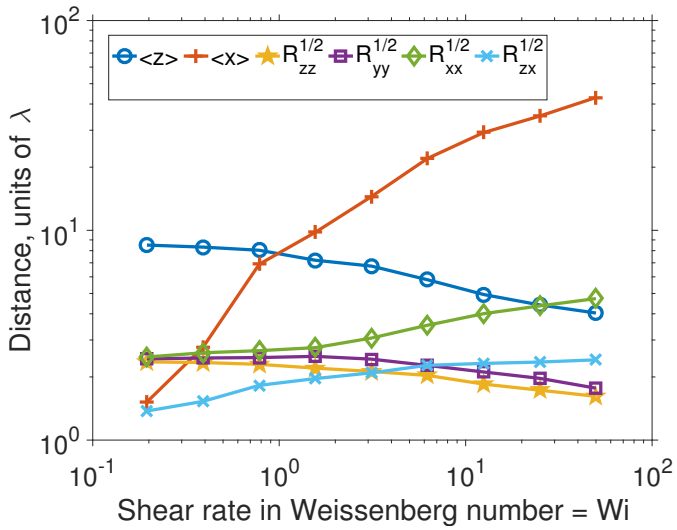

Supplementary Figure 9: Mean brush centre distance from the grafting point perpendicular to the interface, $\langle z \rangle$, and along the shear flow, $\langle x \rangle$. The components of the inertia tensor are also shown.

Bibliography

[1] Robert G Owens and Timothy N Phillips. *Computational rheology*, volume 14. World Scientific, 2002.

[2] Jean-Louis Barrat and Jean-Pierre Hansen. *Basic concepts for simple and complex liquids*. Cambridge University Press, 2003.

[3] Ronald L. Panton. *Incompressible Flow*. John Wiley and Sons, Inc., 2013.

[4] Anil K Bhowmick and Howard Stephens. *Handbook of elastomers*. CRC Press, 2000.

[5] Montgomery T Shaw. *Introduction to polymer rheology*. John Wiley & Sons, 2012.

[6] Partho Neogi. *Diffusion in polymers*, volume 32. CRC Press, 1996.

[7] Masao Doi and Sam F Edwards. *The theory of polymer dynamics*, volume 73. oxford university press, 1988.

[8] Chang Dae Han. *Rheology and Processing of Polymeric Materials: Volume 1: Polymer Rheology*, volume 1. Oxford University Press on Demand, 2007.

[9] Jacob Klein. Molecular mechanisms of synovial joint lubrication. *Proceedings of the Institution of Mechanical Engineers, Part J: Journal of Engineering Tribology*, 220(8):691–710, 2006.

[10] Yuris Dzenis. Spinning continuous fibers for nanotechnology. *Science*, 304(5679):1917–1919, 2004.

[11] Andrew M Howe, Andrew Clarke, and Daniel Giernalczyk. Flow of concentrated viscoelastic polymer solutions in porous media: effect of mw and concentration on elastic turbulence onset in various geometries. *Soft matter*, 11(32):6419–6431, 2015.

[12] Steve Edmondson, Vicky L Osborne, and Wilhelm TS Huck. Polymer brushes via surface-initiated polymerizations. *Chemical society reviews*, 33(1):14–22, 2004.

[13] Ronald G Larson. *Constitutive Equations for Polymer Melts and Solutions: Butterworths Series in Chemical Engineering*. Butterworth-Heinemann, 2013.

[14] Max Wolff, Peter Kuhns, Georg Liesche, John F Ankner, Jim F Browning, and Philipp Gutfreund. Combined neutron reflectometry and rheology. *Journal of Applied Crystallography*, 46(6):1729–1733, 2013.

[15] Airidas Korolkovas, Philipp Gutfreund, and Jean-Louis Barrat. Simulation of entangled polymer solutions. *The Journal of Chemical Physics*, 145(12):124113, 2016.

[16] Longjian Xue, Jilin Zhang, and Yanchun Han. Phase separation induced ordered patterns in thin polymer blend films. *Progress in Polymer Science*, 37(4):564–594, 2012.

[17] Yuri B Melnichenko. *Small-Angle Scattering from Confined and Interfacial Fluids: Applications to Energy Storage and Environmental Science*. Springer, 2015.

[18] Abhijit P Deshpande, J Murali Krishnan, and Sunil Kumar. *Rheology of complex fluids*. Springer Science & Business Media, 2010.

[19] RA Campbell, HP Wacklin, I Sutton, R Cubitt, and G Fragneto. Figaro: The new horizontal neutron reflectometer at the ill. *The European Physical Journal Plus*, 126(11):1–22, 2011.

[20] Henri Orland and M Schick. Simple integral equation for the polymer brush. *Macromolecules*, 29(2):713–717, 1996.

[21] Glenn Fredrickson. *The equilibrium theory of inhomogeneous polymers*, volume 134. Oxford University Press on Demand, 2006.

[22] Ludovic Berthier and Jean-Louis Barrat. Nonequilibrium dynamics and fluctuation-dissipation relation in a sheared fluid. *The Journal of Chemical Physics*, 116(14):6228–6242, 2002.

[23] Jean Louis Barrat. A possible mechanism for swelling of polymer brushes under shear. *Macromolecules*, 25(2):832–834, 1992.

[24] Kurt Kremer, Sathish K Sukumaran, Ralf Everaers, and Gary S Grest. Entangled polymer systems. *Computer physics communications*, 169(1):75–81, 2005.

[25] TCB McLeish. Tube theory of entangled polymer dynamics. *Advances in physics*, 51(6):1379–1527, 2002.

[26] Mike P Allen and Dominic J Tildesley. *Computer simulation of liquids*. Oxford university press, 1989.

[27] Kurt Binder. *Monte Carlo and molecular dynamics simulations in polymer science*. Oxford University Press, 1995.

[28] Igor V Pivkin, Bruce Caswell, GE Karniadakis, and K Lipkowitz. Dissipative particle dynamics. *Reviews in computational chemistry*, 27:85–110, 2011.

[29] Gary S Grest and Kurt Kremer. Molecular dynamics simulation for polymers in the presence of a heat bath. *Physical Review A*, 33(5):3628, 1986.

[30] Patrick S Doyle, Eric SG Shaqfeh, and Alice P Gast. Rheology of polymer brushes: A brownian dynamics study. *Macromolecules*, 31(16):5474–5486, 1998.

[31] Iwao Teraoka. *Polymer Solutions: An Introduction to Physical Properties*. John Wiley and Sons, Inc., 2002.

[32] Pierre-Gilles De Gennes. *Scaling concepts in polymer physics*. Cornell university press, 1979.

[33] Prince E Rouse Jr. A theory of the linear viscoelastic properties of dilute solutions of coiling polymers. *The Journal of Chemical Physics*, 21(7):1272–1280, 1953.

[34] Alexei E Likhtman. Viscoelasticity and molecular rheology, 2012.

[35] Rep Kubo. The fluctuation-dissipation theorem. *Reports on progress in physics*, 29(1):255, 1966.

[36] Gr K Batchelor. An introduction to fluid dynamics. *Cambridge University Press. Cambridge. UK*, 515:P13, 1967.

[37] ST Milner and TCB McLeish. Reptation and contour-length fluctuations in melts of linear polymers. *Physical Review Letters*, 81(3):725, 1998.

[38] Jean Louis Viovy, Michael Rubinstein, and Ralph H Colby. Constraint release in polymer melts: Tube reorganization versus tube dilation. *Macromolecules*, 24(12):3587–3596, 1991.

[39] Kurt Kremer and Gary S Grest. Dynamics of entangled linear polymer melts: A molecular-dynamics simulation. *The Journal of Chemical Physics*, 92(8):5057–5086, 1990.

[40] John R Dorgan, Nicholas A Rorrer, and C Mark Maupin. Parameter free prediction of rheological properties of homopolymer melts by dynamic monte carlo simulation. *Macromolecules*, 45(21):8833–8840, 2012.

[41] Hiroshi Fujita. *Polymer solutions*, volume 9. Elsevier, 2012.

[42] JT Padding and WJ Briels. Systematic coarse-graining of the dynamics of entangled polymer melts: the road from chemistry to rheology. *Journal of Physics: Condensed Matter*, 23(23):233101, 2011.

[43] Giovanni Ciccotti, Mauro Ferrario, and Christof Schuette. *Molecular Dynamics Simulation*. MDPI, 2014.

[44] Jaewoon Jung, Akira Naruse, Chigusa Kobayashi, and Yuji Sugita. Gpu acceleration and parallelization of genesis for large-scale molecular dynamics simulations. *Journal of Chemical Theory and Computation*, 2016.

[45] Pep Espanol and Patrick Warren. Statistical mechanics of dissipative particle dynamics. *EPL (Europhysics Letters)*, 30(4):191, 1995.

[46] Amir Saadat and Bamin Khomami. Matrix-free brownian dynamics simulation technique for semidilute polymeric solutions. *Physical Review E*, 92(3):033307, 2015.

[47] Petri Nikunen, Ilpo Vattulainen, and Mikko Karttunen. Reptational dynamics in dissipative particle dynamics simulations of polymer melts. *Physical Review E*, 75(3):036713, 2007.

[48] PG Bolhuis, AA Louis, JP Hansen, and EJ Meijer. Accurate effective pair potentials for polymer solutions. *The Journal of Chemical Physics*, 114(9):4296–4311, 2001.

[49] K Binder and A Milchev. Polymer brushes on flat and curved surfaces: How computer simulations can help to test theories and to interpret experiments. *Journal of Polymer Science Part B: Polymer Physics*, 50(22):1515–1555, 2012.

[50] Roland R Netz and M Schick. Polymer brushes: from self-consistent field theory to classical theory. *Macromolecules*, 31(15):5105–5122, 1998.

[51] SA Egorov. Interactions between polymer brushes in solvents of variable quality: A density functional theory study. *The Journal of chemical physics*, 129(6):064901, 2008.

[52] Giovanna Fragneto-Cusani. Neutron reflectivity at the solid/liquid interface: examples of applications in biophysics. *Journal of Physics: Condensed Matter*, 13(21):4973, 2001.

[53] Airidas Korolkovas. Simulating confined particles with a flat density profile. *Physical Review E*, 94(2):021302, 2016.

[54] C Gay. Wetting of a polymer brush by a chemically identical polymer melt. *Macromolecules*, 30(19):5939–5943, 1997.

[55] E Weinan, Bjorn Engquist, and Zhongyi Huang. Heterogeneous multiscale method: a general methodology for multiscale modeling. *Physical Review B*, 67(9):092101, 2003.

[56] ST Milner. Polymer brushes. *Articles, Feb*, 22, 1991.

[57] Günter Reiter and Rajesh Khanna. Kinetics of autophobic dewetting of polymer films. *Langmuir*, 16(15):6351–6357, 2000.

[58] Luis González MacDowell and Marcus Müller. Observation of autophobic dewetting on polymer brushes from computer simulation. *Journal of Physics: Condensed Matter*, 17(45):S3523, 2005.

[59] MW Matsen and JM Gardiner. Autophobic dewetting of homopolymer on a brush and entropic attraction between opposing brushes in a homopolymer matrix. *The Journal of Chemical Physics*, 115(6):2794–2804, 2001.

[60] Alexis Chennevière, Fabrice Cousin, François Boué, Eric Drockenmuller, Kenneth R Shull, Liliane Léger, and Frédéric Restagno. Direct molecular evidence of the origin of slip of polymer melts on grafted brushes. *Macromolecules*, 49(6):2348–2353, 2016.

[61] Bin Zhao and William J Brittain. Polymer brushes: surface-immobilized macromolecules. *Progress in Polymer Science*, 25(5):677–710, 2000.

[62] P Mansky, Y Liu, E Huang, TP Russell, and C Hawker. Controlling polymer-surface interactions with random copolymer brushes. *Science*, 275(5305):1458–1460, 1997.

[63] Jeffrey Pyun, Tomasz Kowalewski, and Krzysztof Matyjaszewski. Synthesis of polymer brushes using atom transfer radical polymerization. *Macromolecular Rapid Communications*, 24(18):1043–1059, 2003.

[64] Reihaneh Mohammadi Sejoubsari, Andre P Martinez, Yasemin Kutes, Zilu Wang, Andrey V Dobrynin, and Douglas H Adamson. Grafting-through: Growing polymer brushes by supplying monomers through the surface. *Macromolecules*, 49(7):2477–2483, 2016.

[65] Julia S Higgins and Henri Benoît. *Polymers and neutron scattering*. Clarendon press Oxford, 1994.

[66] David Griffiths. *Introduction to Quantum Mechanics (2nd ed.)*. Prentice Hall, 2004.

[67] Neutron activation and scattering calculator. https://www.ncnr.nist.gov/resources/activation/. Accessed: 2016-10-20.

[68] Jens Als-Nielsen and Des McMorrow. *Elements of modern X-ray physics*. John Wiley & Sons, 2011.

[69] SK Sinha, E Bv Sirota, S Garoff, and HB Stanley. X-ray and neutron scattering from rough surfaces. *Physical Review B*, 38(4):2297, 1988.

[70] L Nevot and P Croce. Caractérisation des surfaces par réflexion rasante de rayons x. application à l'étude du polissage de quelques verres silicates. *Revue de Physique appliquée*, 15(3):761–779, 1980.

[71] Lyman G Parratt. Surface studies of solids by total reflection of x-rays. *Physical review*, 95(2):359, 1954.

[72] Florin Abelès. La théorie générale des couches minces. *J. Phys. Radium*, 11(7):307–309, 1950.

[73] Andrew Nelson. Co-refinement of multiple-contrast neutron/x-ray reflectivity data using motofit. *Journal of Applied Crystallography*, 39(2):273–276, 2006.

[74] EB Zhulina, OV Borisov, and L Brombacher. Theory of a planar grafted chain layer immersed in a solution of mobile polymer. *Macromolecules*, 24(16):4679–4690, 1991.

[75] F Brochard and PG De Gennes. Shear-dependent slippage at a polymer/solid interface. *Langmuir*, 8(12):3033–3037, 1992.

Airidas Korolkovas

Physicist

I invent new physical models, develop algorithms to solve and explore these models, and match my results against experimental data.

Testimonials

*"Great scientific **maturity**."*
– Dr. Fabrice Cousin,
PhD thesis reviewer

*"... one of the most **creative** and interesting papers that I have read in some time."*
– Macromolecules journal reviewer (anonymous)

*"Not only did he present **significant** algorithmic advances, but he also put his code to very good use as a perfect complement to experiment."*
– Prof. Ralf Everaers
PhD thesis reviewer

Awards

International Olympiad on Astronomy and Astrophysics
- Gold (Indonesia, 2008)
- Silver (Thailand, 2007)

Value offered

Core competences

- Large scale stochastic simulations (10^6 degrees of freedom interacting over 10^8 time steps) and the resulting big data statistical analysis.
- Algorithm design and implementation (high performance computing, expertise with GPU and parallel multi-core processing).
- Thin film metrology: multidimensional regression and optimization (genetic, gradient descent). Parameter inference using multiple complementary data sources.
- Intelectual property generation (first author of 3 peer-reviewed articles).

Social skills

- Enthusiastic public speaker, explaining my specialized and often mathematical findings to broad multidisciplinary audiences (3 talks in international conferences).
- Pro-actively seek and obtain resources that I need to drive the project forward. Demonstrated success with upper management, other departments within the company, and external collaborators.
- Leadership: ◊ PhD students' representative; ◊ Designed and supervised 3 Master student projects resulting in experimental reports and presentations.
- Teamwork: coordinated a complex study involving 10 senior researchers from various disciplines, resulting in a scientific discovery.

Business experience

- Salesman at a car battery retailer (2 years, Alekora, Lithuania)
- At the age of 16 sold my first website informatist.net for 1000 euros
- Import/export data operator (8 months, UPS Lithuania)
- Textile chemistry lab technician (3 months, Alvit Mondotessile, Italy)
- Luggage loader (2 months, Brussels airport, language: Dutch)
- Warehouse orderpicker (1 month, Caterpillar, Belgium, language: Dutch)

Training

Education

- PhD "Flow of entangled polymers at interfaces", Université Grenoble Alpes and Institut Laue-Langevin, France, 2016. Main methods: neutron scattering and coarse grained computer simulations.
- MSc in Nanoscience and Nanotechnology, KU Leuven and UJF Grenoble, 2013. Focus: semi-conductor devices, integrated systems, soft lithography, cleanroom training.
- BSc in Textile Engineering, Politecnico di Torino, Italy, and Indian Institute of Technology, New Delhi, 2011. Focus: linear algebra, calculus, probability theory, computer science.

Technical skills

- Software: Matlab, CUDA, C, Python, FreeFEM++, Paraview, IgorPro, MS Office, Inkscape, ImageJ. Typesetting (Latex) and web design (HTML/CSS, also PHP+MySQL). OS: Windows and Ubuntu.
- Hardware: Neutron and x-ray reflectometry and small angle scattering, neutron spin-echo, ellipsometry, rheology, microscopy, optics, surface chemistry, polymer chemistry.
- Languages: English (fluent), French (professional), Italian (conversational), Dutch (basic), Lithuanian (native).

Volunteering, extracurricular

- Member of the Heavy Athletics Club (Haltérophilie Club Grenoblois), encouraging and promoting athletic activities and healthy lifestyle in the local community.

Born 16/10/1989 ● Lithuanian citizenship ● Driving licence B ● Tel. +33684155337 ● airidas.korolkovas89@gmail.com
Home address: 6 rue Bressieux, Grenoble, France